Combined in-situ spectroscopic and electrochemical studies of interfacial and interphasial reactions during adsorption and de-adhesion of polymer films on metals

PhD Thesis
Dr. rer. nat.

Faculty of Science
at the
University of Paderborn

Submitted by
Monika Santa
from Düsseldorf

Paderborn, July 2010

Submitted: 14 May 2010

Defence: 22 June 2010

First referee:	Prof. Dr.-Ing. Guido Grundmeier
Second referee:	Prof. Dr. Wolfgang Bremser

Acknowledgement

The present work was performed at the Max-Planck-Institut für Eisenforschung in the working group of Prof. Dr.-Ing. Guido Grundmeier. I would like to thank him for the opportunity to work under his supervision in Düsseldorf and Paderborn. With his support and productive discussions he helped me to improve my scientific work and conclude my PhD.

Prof. Dr. Wolfgang Bremser gets my acknowledgment for refereeing my thesis and his comments.

I would like to thank Dr. Ralf Posner for many fruitful discussions and an efficient cooperation. Further, I would like to thank Dr.-Ing. Haybat Itani. In our collaboration I had the opportunity to learn a lot about polyelectrolyte systems.

I am grateful to my dear collegues Dr. Nicole Fink, Dipl.-Chem. Katharina Pohl, M.Sc. Julia Lengsfeld, Olesja Stöhr, Dr. Patrick Keil, Dr.-Ing. Juan Zuo, Dr. Markus Valtiner and Dipl.-Phys. Romina Krieg, who supported me with their comments and helped me anytime. I would also like to thank my former colleagues Dipl.-Phys. René Vlasak, who helped me with IR spectroscopy, Dr. Ingo Klüppel for advice in electrochemical questions, and Dr. Tobias Titz for his help with the plasma deposition of TMDS and SKP measurements. I would like to thank my new colleague Dr. Cindy Münzenberg for helping me with corrections of the present work.

Further, I would like to thank Monika Nellessen for the FIB preparation of my polymer samples and SEM analysis. Ralf Selbach and the workshop made it possible to build my in-situ SERS cell.

I thank Philipp for his unlimited patience and grate support particularly during the last year of my PhD time.

The present work was carried out with the financial support of Cognis GmbH, Düsseldorf.

Ich versichere, dass ich diese Arbeit eigenständig verfasst und keine anderen als die angegebenen Quellen und Hilfsmittel benutzt, sowie Zitate kenntlich gemacht habe.

Content

1 Motivation

Water borne epoxy-amine polymers have been developed in order to replace solvent borne epoxy-amine polymers in the future. High performance in corrosion protection is achieved by a large variety of solvent based epoxy-amine polymers. However, water based polymers are preferred in corrosion protection due to reduced application of harmful educts during production and low emission of volatile organic compounds during application [1].

However, the main properties of the polymer arise from the solvent used. Therefore, water based coatings in general tend to higher water uptake. Atmospheric corrosion is promoted in presence of water or humidity and by corrosive gases and ions which can penetrate the polymer coatings. Atmospheric water reaching the metal surface through defects and microcracks of the polymer causes corrosive reactions at the polymer/steel interface. The main features required are therefore low uptake of water and aqueous electrolytes and adhesion in presence of high humidity. Low water uptake and low diffusion rates impede corrosive ractions, as long as the polymer is intact. When corrosion started, the adhesion strength is an important factor. Adhesion under wet conditions is usually lower than in dry atmosphere. Of course duration of wetting plays a role. Adhesion promoters enable to modify and tune properties concerning water uptake and wet adhesion [2,3,4].

The aim of this study is to understand the reasons for the different behaviour of the water and the solvent borne epoxy-amine polymers in detail e.g. the effect of the bulk structure and the interface structure on the behaviour in humid environment or the differences in adhesion. These properties determine the properties of corrosion protection of both polymers in general. Furthermore, the mechanism of corrosion is analysed for both polymers. During corrosion polymers degrade at the polymer/substrate interface due to oxidative side-reactions which result in loss of polymer/substrate adhesion. The analysis of these buried polymer/substrate interfaces is important for the detailed understanding which is needed to improved corrosion protection.

Firstly, water uptake and interface stability of the water and the solvent borne epoxy-amine polymers are analysed without any additives, then organosilanes were added to improve the interface stability in humid environment. Diffusion and water uptake were studied by electrochemical impedance spectroscopy (EIS) and attenuated total reflection infrared (ATR-IR) spectroscopy. The polymer/steel interface was analysed by a 90°-peel test after wet de-adhesion. The peeled substrate surface was further characterised by means of X-ray photoelectron spectroscopy (XPS) and scanning electron microscopy (SEM).

After understanding the bulk and interface properties in humid atmosphere the behaviour in corrosive environment was studied; this means that ions penetrate the interface, starting from a prepared defect. Anticorrosion properties and the mechanism of corrosion on steel were analysed by scanning Kelvin probe (SKP) and influence of water uptake and wet deadhesion were shown.

In order to gain a deeper insight into ion diffusion in polymers and oxidative reactions during corrosion at the polymer/metal interface, a mechanistic approach was chosen. In-situ backside surface enhanced Raman spectroscopy (SERS) was introduced as a method for studying buried interfaces. Model systems were prepared consisting of thin noble metal layers and thiol monolayers or polyelectrolytes of 100 nm thickness. Thereby, the mechanism of oxidative polymer degradation at the interface was studied. The developed setup was further applied to diffusion of the corrosion inhibitor 2-mercaptobenzimidazole through a polyelectrolyte coating. A strong influence of post-treatments like addition of Ag nanoparticles or curing at elevated temperatures on the diffusion rate is shown.

2 Introduction

2.1 Transport of small molecules and ions in polymers

Under ambient conditions polymers are penetrated by gases and liquids. According to the application transport processes are favoured or reduced. If a polymer coating is used in corrosion protection, diffusion of water, oxygen and corrosive gases have to be minimised. In other cases selective transport properties of polymers like polyelectrolytes are used for separation of gases or liquids from mixtures [5].

The basic mathematical model describing permeation in polymers is Fick's diffusion law. It describes ideal diffusion and can be applied when the diffusing molecule is much smaller than the monomer unit of the polymer. Chemical reactions between the different species and the polymer matrix are neglected. Interactions between penetrant and polymer are therefore small and diffusion takes place by random jumps of the penetrant molecules in the polymer. This applies for example to oxygen and water in hydrophobic polymers. If the penetrant molecules are the same size of the monomer unit, several units have to move for creating a hole. This applies to organic solvents and swelling agents. Diffusion is strongly concentration dependent in this case and is found, for example, in glassy polymers. Above their glass transition temperature (T_g) it is Fickian diffusion.

Alfrey et al. discerne between Case I and Case II diffusion in glassy polymers based on the relative mobilities of penetrant and polymer segment [6]. Case I refers to Fickian diffusion with $\alpha = ½$ in:

$$\frac{M_t}{M_s} = kt^{\alpha} \tag{2.1}$$

(with M_t mass of water sorbed at time t and M_s mass sorbed by the polymer at equilibrium, k and α are system parameters). Penetrant mobility has to be much lower than polymer segment mobility and can be described by a constant diffusion coefficient. Case II means non-Fickian diffusion (with $\alpha \geq 1$) when the penetrant mobility is greater than the segment mobility. This process results in an outer swollen layer separated from an inner glassy core. The boundary advances with constant velocity. Case II diffusion includes chemical interaction of the polymer with the penetrant molecule [21]. Anomalous diffusion proceeds at much smaller or larger rates.

Apicella et al. proposed three different modes of water sorption: bulk dissolution in the polymer network, moisture sorption onto the surface of holes that define the free volume of the glassy structure and H-bonding with hydrophilic groups of the polymer [7,8]. Other publications interpret two distinct forms of water in epoxy compounds, which certainly occur at the same time: filling of voids and defects in the bulk and specific interactions of water molecules with polar functional groups [9,10]. Transport through pores was described by

Soles et al. [11,12]. It depends on the polymer structure, morphology and crosslink density. The second interaction is related to the presence of H-bonding sites along the polymer chains. Polarity of functional groups in the polymer and of transported molecules plays an important role [9] and are also influenced by the presence of solved ions [13,14]. Diffusion of water is therefore enhanced in water based polymers.

On the one hand the polymer structure has an effect on water diffusion properties but on the other hand the absorbed water modifies the mechanical properties of the polymer. A general effect of water uptake in epoxy polymers is depression of glass transition temperature T_g and plasticisation [15-17]. H-bonds between water and hydroxyl groups of the network will disrupt the interchain H-bonding and decrease mechanical strength. The molecular structure is altered and T_g is reduced [15]. Hygrothermal degradation means that microcracks develop, chain scission and swelling stresses occur through hydrolysis during water uptake.

Water uptake and diffusion can be monitored by gravimetric measurements, electrochemical impedance spectroscopy, IR spectroscopy or neutron reflectivity [18]. To date, gravimetry is often used in combination with EIS [19]. Crank and Park [20] described weight gain as a function of time with Fickian diffusion. Determination of diffusion coefficient from impedance measurements is performed by different methods [21] and used by several groups [10,14,21-23]. Cotugno et al. conclude from EIS measurements that diffusion in polymers may be a two stage process consisting of fast diffusion, followed by slow rearrangement of the polymer chains [16]. Similar conclusions are drawn by Hinderliter at al. [24] based on impedance measurements showing increasing coating capacitance during swelling, which is opposite to the expected effect. They conclude that polymer chain relaxation allows a higher water volume fraction before the polymer starts swelling. At the same time distribution of water within a coating changes, becoming more connected: droplets merge into cylinders and aspect ratio increases [28]. Kittel et al. were able to perform impedance measurements for inner and outer layers of the coating [29,30]. Free-standing and applied coatings were compared, they often show different properties, because of the substrates influence. In ATR-IR spectroscopy Fick’s model was adopted by Fieldson and Barbari [22,23]. Furthermore, detection of different types of interaction or “states” of water molecules is possible by IR spectroscopy. Bulk dissolution, H-bonding interaction between polymer and water, clustering of water molecules, adsorption onto the surface of free microvoids can be differentiated with this method.

Non-uniform distribution of water in the polymer often result from the film formation process, e.g. hydrophilic interstices in latex polymers. These structures have an effect on the electrochemical response of a polymer. Concentration gradients which exist due to size exclusion of a charged species lead to space charge layers e.g. at the polymer surface. The Donnan potential is the potential step related to the space charge layers. If two diffusing species seeking for electroneutrality have different mobilities a diffusion potential is generated [27]. With polyelectrolytes such electrochemical potentials were evaluated by Tagliazucchi et al. and Calvo et al. [26,25]. They show that a varying polyelectrolyte structure results in changing potential responses if used as electrode coating.

2.2 Vibrational spectroscopy at polymer/metal interfaces

Varying penetration depth from a monolayer to several hundred micrometers can be achieved by means of vibrational spectroscopy. Using IR spectroscopy the penetration depth can be varied by changing the angle of the incident IR radiation: the polymer bulk is observed at low incidence angles around 90° and the substrate surface composition is measured at high incidence angles of about 80° [38,39]. Thereby, interface/interphase properties or changes can be evaluated. The "interface" describes in this context a monomolecular layer on the substrate or at the border between the substrate and the adjacent polymer layer. The term "interphase" includes a higher number of molecular layers. Possart et al. precisely define the "interphases" in a polymer layer coated on a substrate [40]. They differentiate between a some 100 nm thick "chemical interphase" which is characterised by different cross-linking compared to the bulk phase due to bonds to the substrate surface. They also mention "morphological interphases" which result upon segregation processes and different curing process in the bulk and at the coating surfaces.

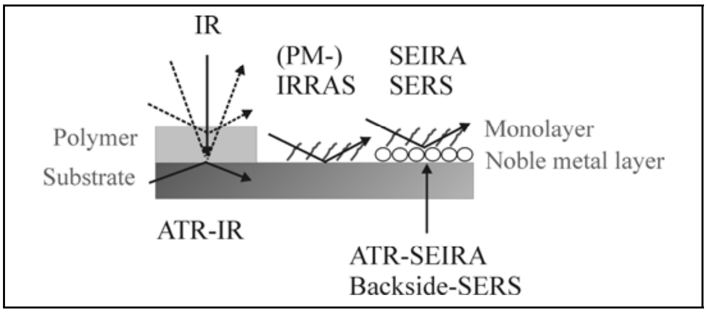

Fig. 2-1: Overview of vibrational spectroscopy techniques applied to polymer/metal interfaces

The substrate/air interface can be studied by infrared reflection absorption spectroscopy (IRRAS) [41]. PM (polarisation modulated)-IRRAS is used for high interface sensitivity and determination of adsorption geometries of ordered structures on metal surfaces [42]. Using this geometry the contribution of the surrounding atmosphere are eliminated due to the following surface selection rules (Fig. 2-2): the incident IR radiation with a parallel polarisation (to the plane of incidence) is absorbed by dipoles perpendicular to the surface. The absorption is enhanced by the conductive substrate. IR radiation with a perpendicular polarisation is not enhanced and generally provides the information about the atmosphere. Using polarisation modulation, the sample and the background spectra are acquired simultaneously. Also substrate/liquid interfaces can be probed e.g. in correlation with electrochemical studies of the interface [43,44].

In situ studies of polymer film formation on metal substrates were limited to deposition of ultrathin films from the gas phase. Grundmeier et al. applied a combined QCM-IRRAS (Quarz microbalance-IR reflection absorption spectroscopy) approach to observe the film formation of alkoxyorganosilanes from the gaseous phase [45]. Alkoxyorganosilanes need a minimum water adsorption layer on the metal surface before hydrolysis of silane starts and film formation begins. But no spectral features could be assigned to interfacial bonds between organosiloxane and iron oxide. However, with water free deposition these bonds were observed.

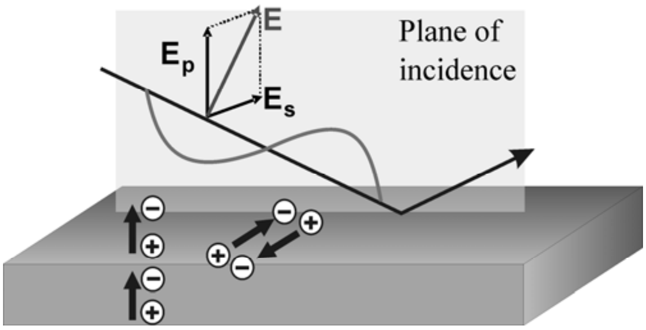

Fig. 2-2: Schematic of PM-IRRAS measurement.The electromagentic vector E of the incident IR beam consists of two components which are parallel and perpendicular to the plane of incidence. E_p – parallel component, E_s – perpendicular (senkrecht) component

Surface enhanced IR (SEIRA) and surface enhanced Raman spectroscopy (SERS) are generally applied for high interface sensitivity. The enhancement of the signal of one monolayer is reached on noble metal surfaces as gold, silver or copper and described in chapter 3.1.1.2. Also the penetration depth of ATR can be improved by surface enhancement (SEIRA-ATR) depending on the angle of the incident IR radiation and on the thickness of the enhancing metal layer.

To date, microspectroscopy is used in combination with Raman and IR spectroscopy [56]. Imaging and mapping software tools allow the extraction of measured data in form of images, which show the chemical composition of surfaces or layered structures.

2.2.1 Vibrational spectroscopy in corrosion science

In corrosion protection good adhesion is required for an effective barrier function of a corrosion inhibitor. Diffusion of water and ions can lower adhesion and lead to de-adhesion or loss of adhesion. The interaction between adherence and corrosion propagation is still not clear, because contrasting studies have been published [30]. In this case, water uptake can be detected by IR spectroscopy in transmission or ATR geometry as described by Wapner et al. [35].

Vibrational spectroscopy can be used to detect reaction products like corrosion products [34,36] or addition of components in a polymer/substrate system ex-situ or in-situ [37]. Studies of diffusion or transport (presented in chapter 7.3) are performed, chemical changes are detected while film formation of a polymer (chapter 4.1.1) or partial oxidation of organic components and changes of adsorption geometry (chapter 7.2) are observed.

2.2.2 Buried polymer/metal interfaces

Polymer/metal interfaces are mostly buried interfaces. They can be observed applying substrates which are transparent to the excitation wavelength, like ATR crystals for attenuated total reflection (ATR) IR spectroscopy or glass substrates for SER spectroscopy. Sum-frequency generation (SFG) is also used to probe buried polymer interfaces [46]. Other new methods to study buried interfaces are described in [47] and [48].

Adsorption of water at buried metal surfaces is detected as replacement of adsorbed organic molecules with water in IR spectra: the intensity of vibrational bands related to water increase while polymer bands decrease in intensity as displayed in Fig. 4-9. With ATR-IR spectroscopy or by SFG the state of sorbed water in the polymer/substrate interphase can be interpreted by fitting the OH stretching peak as reported in [16,17,49-53] and applied in chapter 4.2.2 and chapter 5.1. SEIRA in ATR geometry and SERS show the conformation of water molecules in electrolytes in the Helmholtz layer and in the electric double layer.

In chapter 7.3 SERS is used for detection of the buried interface and study of adsorption and adhesion of organic molecules on metal from aqueous solution. Desorption and chemical reaction of thiols on Au and Ag surfaces can be studied. Furthermore, SERS is applied for investigation of the orientation of organic molecules adsorbed on metal surfaces [chapter 7.2, 54,55].

2.3 Fundamentals of adhesion and de-adhesion of polymers on oxides

Adhesion is the interatomic and intermolecular interaction at the interface of two surfaces. The fundamental theories of adhesion are described by Awaja et al. and Packham [57,58]. They report that the pioneering work of McBain and Hopkins [59] led to the development of the modern adsorption and mechanical theories of adhesion. In Russia the electrostatic theory was developed by Deryagin [60] and the diffusion theory of adhesion by Voyztskii [61]. Recently, contact mechanics, molecular dynamics and surface analysis have provided considerable insight into the nature of the interface and interfacial region in adhesive joints.

Hopkins specific adhesion involved interaction between surface and adhesive, which could be chemical adsorption, adsorption or mere wetting. In this theory adhesion of the polymer and structure of the paint substrate layer is controlled by the chemical groups at or near the interface which to date is called “molecular bonding”, implying van der Waals interactions, covalent and coordinative bonds between polymer and substrate. According to Hopkins theory the chemical composition of the polymer surface correlates with the wetting behaviour of the polymer and the contact angle (“thermodynamic adhesion”). Surface energies are associated with failure because failure involves forming new surfaces. However, the measured adhesion values strongly differ from theoretically determined thermodynamic work terms. The third adhesion mechanism which is discussed is the “mechanical coupling”. It refers to the mechanical interlocking of the polymer and a rough surface. The higher adhesion strength is in this case due to the increased surface area and more molecular bonding interactions.

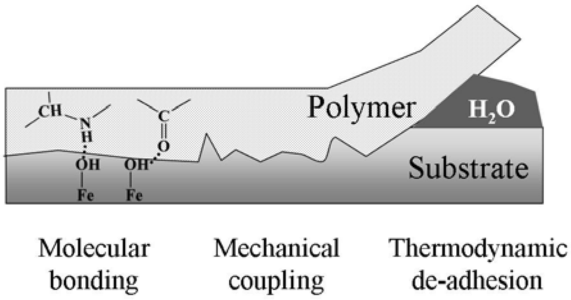

Fig. 2-3: Adhesion mechanisms described by McBain and Hopkins [59] and by Awaja et al. [57].

Water interferes with the molecular bonding of the polymer to the substrate: the water molecules interact with the substrate surface and modify the oxide structure. Further, water molecules interact with the functional groups of the polymer. Thereby the polymer structure is modified by swelling processes which are enhanced in the presence of ions. The concept of wet de-adhesion was introduced by Funke et al. [31-33].

Adsorption energy is determined in-situ by chemical force microscopy. These experiments show that adhesion over a sample surface is often very heterogeneous. Reorganisation of the surfaces occurs after they are brought together and interdiffusion or interpenetration lead to roughening of the surface. The composition of the interphase is determined ex-situ by surface analysis tools like XPS and static secondary ion mass spectrometry (SIMS) [62]. Nazarov et al. performed SKP measurements in order to determine the polymer adhesion to the metal substrate [170,171].

2.4 Adhesion mechanisms of organosilanes on oxides

Organosilanes have been studied as additives and primers for epoxy adhesives [63-66]. They are used as primers instead of chromates also with water based coatings [67-,69]. Further, they are applied to stabilise dispersions or modify surfaces embedded fibers [70-72]. Seth et al. introduced water based “self-priming” coatings which they called “superprimers” [73].

Organosilanes are adsorbed on oxidic surfaces as iron oxide, alumina or silicon oxide from aqueous solution. Self-assembly is only observed when a long alkylchain-substituents are present in the organosilane [74-76]. In the other cases an unordered multilayer consisting of oligomers coveres the substrate. The bond to the substrate can be established by the silanol groups or the functional group of the organic rest. Gettings and Kinloch [77] studied polysiloxane surfaces on iron by XPS and static SIMS. Different silicon containing fragments SiO^{2-}, $SiOH^{+}$ and $FeSiO^{+}$ were interpreted as indicators for Si-O-substrate surface chemical bonding. This is confirmed by van Ooij and Sabata [78]. Abel et al. found evidence of Si-O-Al bonding in a different study [79].

If alkoxyorganosilanes are used as additives they still need a minimum water adsorption layer on the metal surface before hydrolysis of silane starts and leads to film formation [80]. Amine components in the organosilane solution enhance organosilane adsorption on the substrate [77,81].

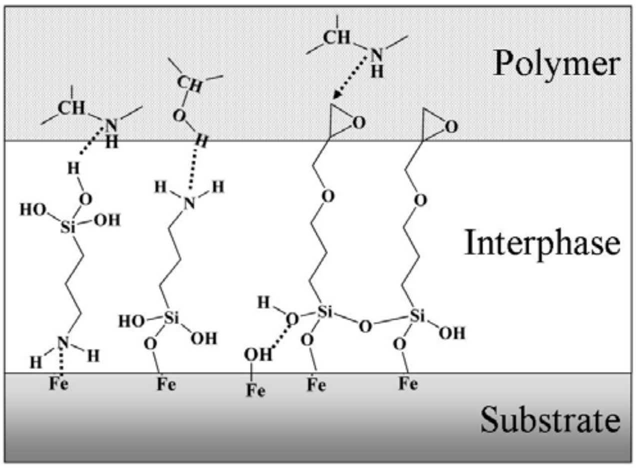

Fig. 2-4: Adhesion promotion by addition of the organosilanes APS (3-aminopropyl(trimethoxy)silane and GPS (3-glycidoxypropyl(trimethoxy)silane).

Reaction between functional groups of the organosilane and the adhesive system has been demonstrated by Watts et al. [82]. Characteristic reaction products between amine curing agent and the oxirane ring of 3-glycidoxypropyl(trimethoxy)silane (GPS) were detected in SIMS. Senett et al. [83] performed molecular dynamics simulations on the adsorption of trimethoxy-GPS on aluminum oxide and iron oxide. Their results show that GPS is likely to bind to the iron oxide surface via the silanol group, but on aluminium oxide the epoxy group approaches the surface. As a result adhesion promotion by GPS of a polymer to iron oxide is better than to aluminum oxide. Formation of organosilane layers on metals is complex and strongly depends on the surface [84]. Possible reactions between the organosilanes, the polymer and the substrate are displayed in Fig. 2-4.

Until now, the adhesion promoting mechanism of organosilanes is explained by segregation or diffusion to the interfaces [18,85-87]. Wang and Schaefer [18] used neutron reflectivity to understand the adhesion promoting mechanism of organosilanes as epoxy additives and found that the silane is consumed at the interface. This is the driving force for silane diffusion to the interface. Not only the interface exhibits high silicon amounts but also the density of the polymer bulk changed, indicating higher cross linking. It is often reported that water uptake is reduced by addition of organosilanes [72,88-90].

2.5 Corrosive de-adhesion of polymers on zinc and iron substrates

Bare iron and steel surfaces easily corrode in presence of water and oxygen. Polymeric coatings are commonly applied for reducing the corrosion reaction at the steel surface. They inhibit the contact of the steel surface with water and electrolyte and reduce the oxygen diffusion to the steel surface. However, a defect in the corrosion protection coating leads to an electrochemical cell in presence of an aerated electrolyte. As a result, the electrolyte enters the polymer/steel interface and macroscopic de-adhesion of the polymer takes place. This process dominates in high humidity and occurs on metals like iron or zinc which are covered by conductive oxide structures. The process of cathodic delamination is describe due to results achieved by SKP, adhesion tests, XPS and ToF-SIMS surface analysis [96,98,99,105,106, 108,132,145,162-165,168,173].

The electrochemical reaction which is typical for the cathodic delamination process starts with iron oxidation in the defect center. Fig. 2-5 shows that oxygen is reduced at the same time at the egde of the defect. The defect potential determined by SKP is measured at steady state conditions (i = 0). Initial oxygen reduction can also occur at the intact polymer/metal interface, but it is kinetically strongly inhibited due to a diffuse double layer. The lower the interfacial ion concentration, the less compact the electric double layer at the oxide surface will be. In addition, the Fe^{2+}/Fe^{3+} oxidation is limited by the Fe^{2+} diffusion through the oxide layer.

When iron dissolution occurs in the defect, the electrochemical reaction is induced due to the different potentials of steady states at the defect and intact polymer/steel interface displayed in Fig. 2-5. The electrolyte enters the polymer/steel interface and oxygen reduction increases at the reaction front at the polymer/steel interface. During reduction highly reactive oxygen species lead to degradation and de-adhesion of the polymer. Detection of the polymer degradation at the buried polymer/steel interface is difficult. A new approach applying SER spectroscopy in backside geometry is therefore explained in chapter 7.2.

The hydroxide concentration at the polymer/metal interface increases as oxygen is reduced. Due to the increasing anion concentration cations enter the polymer/metal interface and are therefore typically found in the transport area. Together with the cations also water migrates into the interface. The cation containing electrolyte leads to conductive coupling of the degraded polymer/steel interface to the defect. Therefore the potential of the degraded interface is similar to the defect potential in SKP measurements.

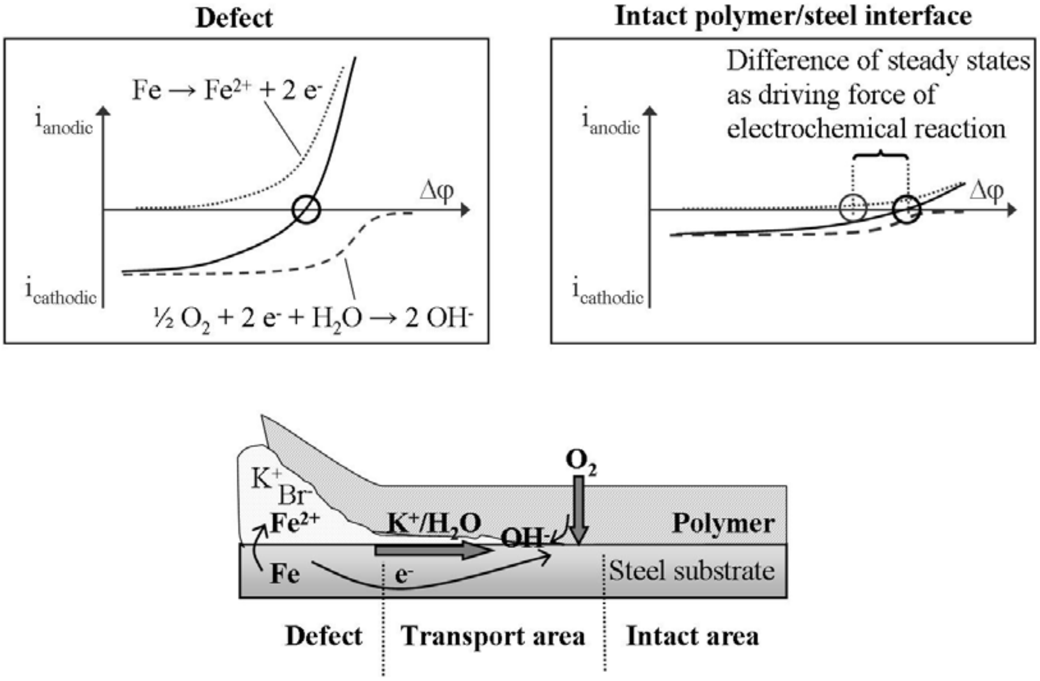

Fig. 2-5: Schematic of the electrochemical reaction during the cathodic delamination process.

Grundmeier et al. [132] and Posner et al. [173] observed cathodic delamination of zinc surfaces in detail. They are of technological interest as galvanised steel surfaces. As zinc is also covered by conducting oxides the same processes observed on iron and steel can occur. However, zinc oxides are not stable in the alkaline environment of oxygen reduction and the oxide scale grow in alkaline environment. If oxygen-free atmosphere the potential of the transport area cathodically shifts to a potential of 400 mV more negative than the defect potential. The defect potential is due to Zn/Zn^{2+} and the potential in the transport are is due to $Zn/Zn(OH_4)^{2-}$. The combined oxygen reduction and zinc dissolution in the transport area buffer the pH and limit the degradation of the polymer/Zn interface. In case of a scratch in the zinc layer of a galvanised steel surface the zinc layer acts as a sacrificial anode.

In some cases wet de-adhesion mentioned in chapter 2.3 occurs at the same time as cathodic delamination. Nazarov et al. described SKP studies of wet de-adhesion and explain that the potential determined by SKP is sensitive to the adhesion state of polymer and metallic surface. However, an combined SKP approach of wet de-adhesion and cathodic delamination was not described and is presented in chapter 6 [159,169].

3 Experimental

3.1 Applied techniques

3.1.1 Spectroscopic techniques

3.1.1.1 IR spectroscopy

IR spectroscopy was used for determination of the chemical composition of polymeric films, i.e. epoxy-amine polymers or polyelectrolyte films. Single reflection experiments at 30° and 80° from the surface normal enable the measurement of varying film thicknesses. In case of a 100 nm thick polyelectrolyte film the absorbance of IR light is enhanced by a large incident angle. IR spectra of polyelectrolyte films were acquired in 80° reflection mode using a Nicolet 5700 FTIR spectrometer (Thermo Electron Corporation, Germany). In case of a 10 µm thick epoxy-amine film the small incident angle assures a lower absorbance. If the absorbance is too high, IR bands broaden and overlap in the spectrum and the spectral information is smaller. IR spectra in 30° reflection geometry were measured with the Bio-Rad Uniflex unit.

In-situ measurement of water uptake in epoxy-amine polymers were performed using the ATR geometry. Thereby, the IR aborbance is enhanced by multiple reflections at the crystal/polymer interface. The incident light is introduced into the ATR crystal and then totally reflected at the edges of the crystal (Fig. 3-1). At each point of total reflection an evanescent wave is formed which penetrates the polymer. The penetration depth *d* of the evanescent wave depends on the wavelength of incident light and constitutes the depth of measurement at the polymer/ATR crystal interface:

$$d = \frac{\lambda}{2\pi\sqrt{n_1^{\,2}\sin^2\Theta - n_2^{\,2}}} \tag{3.1}$$

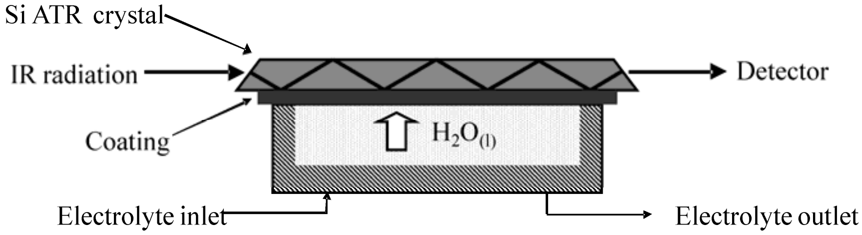

Fig. 3-1: IR spectroscopy in ATR geometry. The silicon ATR crystal is coated with the polymer under study and introduced into a specially designed cell for the determination of water uptake [51].

ATR-IR experiments were performed with a BioRad FTIR 3000 Spectrometer (Digilab, Germany), equipped with a MIR globar source, a DTGS detector and an internal reflection unit of Specac Ltd. (Great Britain). 148 interferograms were taken at room temperature with a spectral resolution of 4 cm^{-1}. Reference spectra of the uncoated silicon ATR crystal were recorded with the same parameters. Reference spectra of dry epoxy-amine films were recorded before filling the applied ATR-cell volume with aqueous borate buffer solution. The change of the ν(OH) peak area was evaluated as a function of time [99].

3.1.1.2 Surface enhanced Raman spectroscopy (SERS)

IR spectroscopy is more popular than Raman spectroscopy because Raman scattering cross sections are very low compared to absorbtion in the IR wavelength region. Therefore, Raman signals are excited by a laser. The challenge is to use enough power to generate a decent spectrum but not to damage the substrate. Surface enhancement caused by rough surfaces of coinage metals is large enough to enable the measurement of monolayers. The enhancement factor can be in the order of 10^6. Surface plasmons are induced on metal structures on the sample surface which are in the range of the exciting wavelength. The interaction of surface plasmons with molecules next to the surface enhances the Raman signal. Different theories try to explain the mechanism of enhancement: the chemical and electromagnetic enhancement, the first layer theory and the theory of hotspots [100-103].

Raman spectra were obtained using a LabRam confocal Raman microprobe system (Dilor LabRAM, ISA Instruments. SA, France) equipped with an Olympus BX40 confocal microscope and an air cooled HeNe laser (λ = 632.8 nm). Measurements were performed applying a 100x objective with a numerical aperture of 0.9 and a 1800 grooves/mm diffraction grating. In-situ backside SERS studies were carried out at > 90 % atmospheric humidity within a custom made cell (see Fig. 7-7).

A similar setup was used for diffusion experiments of 2-mercaptobenzimidazole (MBI) in aqueous solution ($0.13 \cdot 10^{-3}$ mol/L). A Renishaw inVia Raman microscope equipped with a LEICA DM2500M microscope and an air cooled HeNe laser (λ = 632.8 nm) was used for acquisition of SER spectra in this case. Measurements were performed applying a 100x objective with a numerical aperture of 0.85 and a 1800 grooves/mm diffraction grating.

3.1.1.3 X-ray photoelectron spectroscopy (XPS)

XPS is a surface sensitive method with a depth of information of around 5 nm. It gives qualitative and quantitative information about the sample surface. X-rays are focused at the sample surface, absorbed and lead to emission of electrons. The kinetic energy E_{kin} of the emitted electrons is typical for elements on the surface and their chemical bonds:

$$E_{Kin} = h\upsilon - E_{Binding} - \Phi_{Sample} \tag{3.2}$$

with $E_{Binding}$ as binding energy of the electron and Φ_{Sample} as electron work function of the sample. The binding energy is determined using the kinetic energy measured by the detector which is conductively coupled to the sample. Thereby, the Fermi levels of the sample and the detector equalise. The binding energy is determined by the following equation:

$$E_{Binding} = h\upsilon - E_{Kin(Detector)} - \Phi_{Detector} \tag{3.3}$$

(with kinetic energy $E_{Kin\ (Detector)}$ measured by the detector, with the electron work function of the detector $\Phi_{Detector}$). Detected intensities can be quantitatively compared after correction with sensitivity factors which are typical for each element.

XPS experiments were performed with a Quantum 2000 (Physical Instruments, USA). Spectra on iron substrates were measured with 100 x 100 μm^2 spot size at 45° take-off angle using monochromated Al Kα radiation at 25 W and 15 kV. For high resolution spectra pass energy was set to 29.35 eV and step size to 0.125 eV. The Fe_2O_3 peak at 530 eV in the O 1s high resolution spectra was used as internal reference.

Spectra on Au or Ag samples were recorded at 50 W and 17 kV with 1 x 1 mm^2 spot size at 45° take-off angle. For high resolution spectra the pass energy was set to 23.5 eV and the step size to 0.1 eV. Ag 3d and Au 4f peaks were used as internal reference [104].

3.1.1.4 Time-of-flight secondary ion mass spectrometry (ToF-SIMS)

A focused Ga^+ ion beam desorbs and partially ionises molecules from the substrate surface [92]. Time of flight separation of secondary ions is determined by their mass/charge ratio. Acceleration of the secondary ions by an electrostatic field leads to varying time of flight according to their mass/charge ratio. Thereby, information depth of SIMS reaches the sensitivity of one monolayer. Typical patterns of organic mass fragments are detected and allow conclusions concerning the chemical constitution of the substrate surface. However, high surface sensitivity leads to detection of minor components and contaminations on the substrate. Furthermore, the detected ion signal intensities strongly depend on the chemical surroundings and can only be evaluated quantitatively using adequate references.

The ToF-SIMS analysis was carried out with a TRIFT II (Physical Instruments, USA) applying a gallium ion gun at an acceleration voltage of 15 kV on a spot size of 100 x 100 μm^2.

3.1.2 Electrochemical techniques

3.1.2.1 Scanning Kelvin Probe (SKP)

The Kelvin probe is a non-contact and non-destructive method which measures the work function difference $\Delta\Phi_S^{Ref}$ of a needle (reference) and the substrate surface [91,105,106]. The Kelvin probe represents a capacitor with a changing capacitance due to the vibration of the needle (Fig. 3-2). This setup allows the sensitive in-situ detection of a change of surface chemistry due to electrochemical reactions.

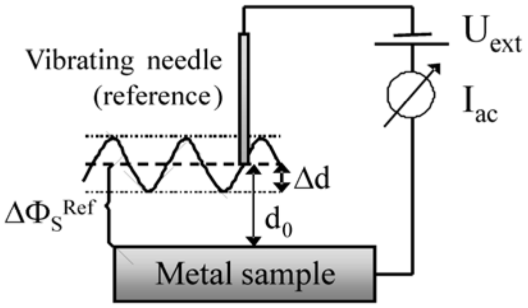

Fig. 3-2: Schematic of the Kelvin probe setup [175].

The Kelvin probe tip and the sample surface form a capacitor. The resulting capacitance can be calculated by the following equation:

$$C = \frac{Q}{V} = \varepsilon\varepsilon_0 \frac{A}{d + \Delta d \cdot \sin \omega t} \tag{3.4}$$

(with the dielectric constant and the permittivity of free space ε and ε_0, the frontal tip area A, the distance d between sample surface and tip and the tip vibration frequency ω). With the external contact of the needle and the substrate the Fermi levels equalise and the contact potential V_{CP} is measured currentless:

$$V_{CP} = \frac{\left(\Phi_{\mathrm{Re}f} - \Phi_S\right)}{e} = \frac{\Delta\Phi_S^{\mathrm{Re}f}}{e} \tag{3.5}$$

(with the work function of the reference Φ_{Ref} and the work function of the substrate Φ_S). During vibration of the needle a current flow is induced in the external contact (I_{ac}). The measured potential difference is obtained when $I_{ac} = 0$.

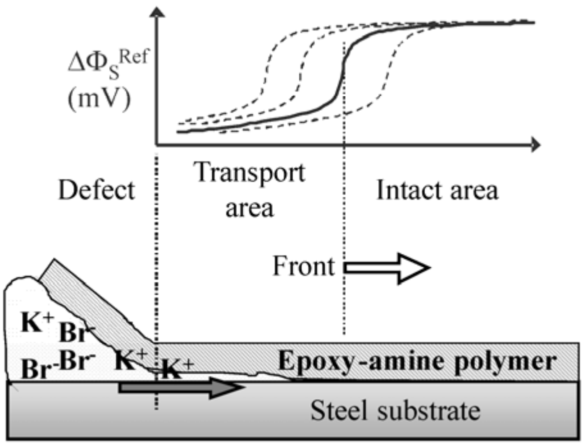

Fig. 3-3: Schematic of the sample during cathodic delamination and resulting sigmoid potential profiles detected by SKP.

The SKP was applied for the detection of electrochemical reactions on uncovered and MBT monolayer covered Au and Ag surfaces and cathodic delamination processes at epoxy-amine/steel interfaces. A defect was prepared and filled with aqueous 0.5 molar KBr solution. The potential at the defect area where iron is oxidised is typically more cathodic than at the intact polymer/iron oxide/iron interface. In case of Au and Ag as surface zinc powder was used as oxidising agent in the defect. The resulting potential difference between the local electrodes (the defect and the intact interface) is discussed as driving force for the electrochemical reaction velocity and, therefore, also determines the delamination kinetics. When ions from the defect enter the polymer/steel interface for reasons of charge compensation, the local interface potential is cathodically shifted to the defect potential. This process can be detected by means of Scanning Kelvin Probe as progressive front moving along the so far intact interface (Fig. 3-3). The delamination velocity strongly depends on the adhesion force between polymer and substrate as well as on the water amount at the interface.

SKP measurements were carried out with a height regulated, custom made Scanning Kelvin Probe [93]. Measurements were performed in humid air of > 95 % r.h. at room temperature, unless otherwise noted. As defect electrolyte 0.5 molar KBr solution was applied. Detected interface potentials could be correlated with respect to the standard hydrogen electrode (SHE) after calibration against Cu/$CuSO_4$ [94]. A part of the coating is lifted from the sample as displayed in Fig. 3-3, in order to avoid spreading of the electrolyte over the polymer surface.

3.1.2.2 Electrochemical impedance spectroscopy (EIS)

EIS measurements were performed using a FAS2 Femtostat (Gamry Instruments, Warminster/USA) in a chloride free borate buffer solution (with pH 8.4). A potential amplitude of 15 mV was applied relative to the open circuit potential of the investigated sample system. A frequency range of 0.1 Hz to 10^5 Hz was implemented on epoxy-amine coated steel substrates or polyelectrolyte covered ITO substrates.

In case of capacitive film behaviour the capacitance of the polymer C_P was calculated according to

$$C_P = \frac{1}{2\pi \cdot f \cdot Z_{\text{mod}}} \tag{3.1}$$

(with Z_{mod} as modulus of the impedance at the excitation frequency f, usually 40 kHz).

Touhsaent and Leidheiser [136] correlated the dielectric properties to the lifetime of coatings. Since then, many studies have reported determination of water uptake from impedance data [130,137,138,21]. The Brasher-Kingsbury approach leads to water uptake values higher than determined by gravimetry. However, it still shows the lowest aberration compared to gravimetric results [21,95,130]. Therefore, it was used to evaluate the water uptake ϕ of the epoxy-amine polymers and polyelectrolyte films [95,130,96]:

$$\phi = K \frac{\log\left(C_{Psat} / C_{P0}\right)}{\log \varepsilon_W} \tag{3.2}$$

(with ϕ the water content expressed as volume fraction, C_{P0} as coating capacitance linearly extrapolated to $t = 0$, C_{Psat} as coating capacitance at saturation prior to any polymer swelling and $\varepsilon_W = 78.3$ as the dielectric constant of water). The assumptions of Brasher and Kingsbury include i) the presence of a conductive electrolyte during the impedance measurement, ii) no chemical changes of the polymer during water uptake, iii) no interaction of water with the polymer (constant $\varepsilon_W = 78.3$), iv) no swelling of the polymer (the factor K is generally taken as 1, but should not exceed 1.25 [130]) and v) a random and uniform distribution of water in the polymer film. Therefore, the Brasher-Kingsbury approach is only applied for water uptake values lower than 8 %.

The diffusion coefficient can be determined because of linear correlation of the capacity change during water uptake [139,140,141]. The model is based on Fickian diffusion and valid, if i) water is evenly distributed along the diffusion path, ii) diffusion is one-dimensional, iii) the diffusion coefficient is constant and not a function of the amount of absorbed water, vi) the coating does not swell during the experiment and coating thickness is constant [142]. The water diffusion coefficient D was evaluated applying equation 3.3 and by linear fitting of the $\log C_{Pt}$ vs. $\sqrt{t}$ graph during the initial immersion time [21,97,98]:

$$\frac{\log C_{Pt} - \log C_{P0}}{\log C_{Psat} - \log C_{P0}} = \frac{2\sqrt{t}}{L\sqrt{\pi}}\sqrt{D} \tag{3.3}$$

(with C_{Pt} as coating capacitance at time t and L as thickness of the coating).

3.1.3 Microscopic techniques

3.1.3.1 Scanning electron microscopy (SEM)

The SEM allows a detailed surface analysis of condensed materials. Electrons are generated by a hot cathode or by Schottky field emission. They are accelerated up to 50 keV and then focused on the surface by electromagnetic lenses. Secondary (below 50 eV) and backscattered electrons (50 eV to acceleration voltage) result upon contact with the specimen. They are detected and used for imaging. Interaction area and depth depend on the acceleration voltage and the elemental composition of the sample material.

Secondary electrons are formed by inelastic interaction of primary electrons with surface atoms. Either a chamber detector or an in-lens detector can be used for their detection. Chamber detectors are mainly Everhart-Thornley detectors that use a grid with an applied voltage between -200 to +200 V. The electrons hit a scintillation counter and the generated photons are amplified by a photomultiplier. High electron yields lead to lighter and lower electron yields to darker pixels in the image. In-lens detectors also collect the electrons by an applied voltage but the detection of the electrons happens by a semiconductor. When an electron hits the detector, it generates electron-hole pairs that lead to an electric signal. In-lens detectors allow much smaller working distances than chamber detectors and collect the electrons at the point of impact. This leads to higher resolution in contrast to the chamber detectors.

SEM does not give any chemical information about the substrate, but Auger electrons and X-rays are formed by the interaction of electrons with the sample. By means of electron dispersive X-ray analysis elemental composition of the substrate is evaluated in a depth of few micrometers [92].

SEM was performed with a LEO 1550 VP (Zeiss, Germany) equipped with an EDX analyser. SEM pictures were acquired with magnification of 10, 15 and 40 kX at voltage of 5 keV in InLens or MPSE mode.

3.1.3.2 Focused ion beam (FIB)

FIB can be used either to image the sample surface or to machine the surface by sputtering with ions. Secondary ions are generated by the interaction of the accelerated Gallium ions with the sample and can be detected in a similar way as in SEM. The ion beam is accelerated with 5 to 30 keV. It can be used to sputter the surface and create structures in the micro and nanometer range, e.g. in preparation of lamellae for transmission electron microscopy. In the present work FIB was used for preparation of cross sections of steel substrates covered with epoxy amine films. The experiment was performed using a Cross Beam XB1540 (Zeiss, Germany). Thereby, a part of the polymer was cut applying an acceleration voltage of the ion beam of 30 kV and a current of 5 nA. Subsequently, the current was decreased to 2 nA in order to acquire SEM images of a flat, representative bulk cross section.

3.1.4 Adhesion tests

Peel tests were performed at a fixed angle perpendicular to the sample surface and with a constant velocity of 3.4 mm/min. Custom made equipment was applied [105,106]. Stripes of 5 mm width were peeled off at different relative atmospheric humidity and at room temperature.

3.1.5 Contact angle measurement

The contact angle θ of a liquid droplet on the sample surface depends on the surface tension of the solid/liquid interface and the surface tension of the solid surface. It is important for the behaviour of paints, adhesives and detergents. In this study it is used to determine the hydrophobicity of the epoxy-amine polymer surface.

The surface tension given in *mN/m* is equivalent to the surface energy (unit *Nm*) that has to be invested when a new surface is generated. Young's equation allows a correlation between the contact angle θ and the solid/gas interface tension γ_{sg}:

$$\gamma_{sg} = \gamma_{sl} - \gamma_{\lg} \cdot \cos\theta \tag{3.4}$$

(with the solid/liquid interface tension γ_{sl} and the liquid/gas interface tension γ_{lg}).

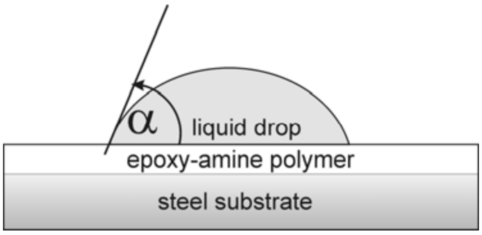

Fig. 3-4: Contact angle between liquid drop and solid surface

Different approaches exist which allow the calculation of surface energies from contact angle measurements. Fowkes introduced an additive approach, describing the bulk phase as a sum of independent contributions from different types of intermolecular interactions. Owens and Wendt extended this approach to the interaction of polar liquids and surfaces [123]. In this case the surface energy consists of two components, the polar γ^p and the dispersive part γ^d:

$$\gamma = \gamma^p + \gamma^d \tag{3.5}$$

The solid/liquid interface tension can be described by:

$$\gamma_{SL} = \gamma_S + \gamma_L - 2\sqrt{\gamma^d{}_S \cdot \gamma^d{}_L} - 2\sqrt{\gamma^p{}_S \cdot \gamma^p{}_L} \tag{3.6}$$

Contact angles of three different solvents – deionised water with pH = 6.8, ethylene glycol and diiodomethane - were measured. The polar ($\gamma^p{}_L$) and dispersive ($\gamma^d{}_L$) components of the surface tension of these solvents are known. Combining equation 3.6 with Young's equation 3.4, the surface energies of the observed system ($\gamma^p{}_S$, $\gamma^d{}_S$) can be determined:

$$\gamma_L(\cos\theta + 1) = 2\sqrt{\gamma^d{}_S \cdot \gamma^d{}_L} + 2\sqrt{\gamma^p{}_S \cdot \gamma^p{}_L} \tag{3.7}$$

Static contact angles were investigated with 10 µl droplets, measured 5 s after deposition on the surfaces and applying a Dataphysics Contact Angle System OCA 20. At least six values were averaged for every angle.

3.2 Sample preparation

Low carbon steel substrates (ST1405) were provided by Cognis GmbH (Düsseldorf/ Germany). They were ultrasonically degreased with organic solvents, then alkaline cleaned with a 3 % Ridoline 1570 TM and 0.3 % Ridosol 1237 TM solution (provided by Henkel AG & Co.KGaA, Düsseldorf/Germany) [107]. Substrates used for peel tests and Scanning Kelvin probe measurements were first ground and polished with 3 µm diamond paste and then alkaline cleaned as described above.

N-type silicon ATR crystals with base trapezoidal angles of 45° were cleaned in an aqueous solution of 30 % NH_3/H_2O_2 at 80°C, rinsed with ultrapure water and dried. Iron covered silicon wafers or ATR crystals were prepared by physical vapour deposition of 6 nm high purity iron using electron beam evaporation [108]. They are covered by approximately 2 nm native iron oxide due to exposure to air.

Samples were coated with a water or a solvent borne two-component model epoxy-amine polymer provided by Cognis GmbH (Düsseldorf/Germany). The organic matrix did not include pigments, fillers or other functional ingredients. The water based epoxy component was dispersed in water and the dispersion was stabilised with a standard surfactant. Epoxy and amine components were mixed with a stoichiometric ratio of 1:1. Epoxy and amine components of the solvent borne polymer were also mixed with a stoichiometric ratio of 1:1 under addition of o-xylene/1-butanol with 3:2 volume ratio. Modified polymers were prepared by addition of 0.5 wt%, 2.5 wt%, 5 wt% 3-aminopropyl(trimethoxy)silane (APS) or γ-glycidoxypropyl(trimethoxy)silane (GPS) to the mixture of epoxy and amine components.

The water borne polymer layers were applied on steel substrates or on silicon ATR crystals, dried in ambient atmosphere for one week and then annealed at 60°C for one hour. The solvent borne polymer was dried in ambient atmosphere for four days and subsequently annealed at 60°C for one hour. Keeping these preparation conditions a Surfix layer thickness analyser (Phynix Company, Cologne / Germany) confirmed film thicknesses of 30 ± 4 µm.

For preparation of SERS substrates silicon wafers were cleaned as described above. Glass substrates with a thickness of 0.25 mm were treated with a 1:2 volume mixture of 98 % H_2SO_4 and 30 % H_2O_2 at 80°C. Then a calcinated cauliflower like hexamethyldisilane plasma polymer film with approximately 120 nm in thickness was deposited on both types of substrates to increase the surface roughness according to Sun et al. [109]. Subsequently, either 50 nm gold of 99.99 % purity were thermally evaporated at a rate of 0.5 Å/s or 70 nm silver of 99.99 % purity were deposited by electron beam evaporation at the same rate. A modification of the preparation was applied for polyelectrolyte substrates. A monolayer of 3-mercaptopropyl(trimethoxy)silane (MPS, Sigma Aldrich) was deposited on the hexamethyldisilane (HMDS) plasma polymer by chemical vapour deposition at room temperature to increase adhesion of the subsequently deposited Ag layer.

2-mercaptobenzothiazole (MBT) monolayers were adsorbed from a 10^{-3} molar MBT solution based on ethanol of analytical grade during three hours, subsequently thoroughly rinsed with fresh ethanol and dried in a nitrogen stream [110].

The polyelectrolyte was deposited from 10^{-3} molar solutions of polyallylamine hydrochloride (PAH, M_w = 56,000 g/mol, Sigma Aldrich) and polyacrylic acid (PAA, M_w = 100,000 g/mol, Sigma Aldrich). The polyelectrolyte solution was adjusted to pH 3.5 by addition of 1 molar NaOH or HCl. Polyelectrolyte layer-by-layer films were deposited by means of the automatic dipcoater DC-Multi-8 (Nima Tchnology Ltd., U.K.). Bilayer films were formed by first dipping the substrate for five minutes in PAA followed by three times two minutes-washing steps in deionized water. The same procedure was used for the PAH layer. Films of 10 bilayers were formed and finally dried in air. For EIS measurements ITO glass substrates (Praezisions Glas & Optik GmbH, Germany) were functionalized before deposition of the polyelectrolyte film. They were immersed in an aqueous solution of 2 g/L polyethylenimine (PEI, 50 wt%, Sigma Aldrich) for 1 hour, then washed with deionized water for 2 minutes and subsequently dried with nitrogen.

Ag nanoparticles containing polyelectrolyte films were prepared by immersing the 10 bilayers films in a $AgNO_3$ solution (Merck) for 1 hour. Ag cations diffuse into the PE network. Metallic nanoparticles form by reduction with 10^{-3} molar $NaBH_4$ (96 % in aqueous solution, Merck) with a reduction time of 30 sec.

All used chemicals and solvents were of p.a. quality.

4 Comparison of water uptake in solvent and water borne epoxy-amine polymers

Solvent and water borne epoxy-amine polymers have been applied in corrosion protection for several decades [1,111,112]. Improving properties of water borne epoxy-amine polymers is motivated by environmental protection and personal safety during application of paints and resins.

Corrosion protection demands for low penetration of water and ions and high interface stability even in presence of water or electrolytes [1]. Usually suitable systems are tested using model systems which allow the application of theoretical considerations, e.g. correlation of adhesion stability with substrate and polymer acid-base properties [114]. In industrial frameworks methods like salt spray test [113] are used.

In this work polymer properties were investigated by EIS, ATR-IR spectroscopy, peel tests, XPS and SEM measurements. The water borne polymer exhibits a higher water uptake than the solvent borne polymer, which leads to different interface stability at high relative humidity or immersion into electrolyte.

4.1 Film formation

Film formation of water and solvent borne polymer was determined in order to establish preparation parameters. Polymerisation of the epoxy and amine components in solution and evaporation of the solvent at the same time are leading to the solvent borne polymer film. The epoxy component of a water borne polymer is an aqueous dispersion. The reaction between the amine component and the epoxy groups begins at the outside of epoxy groups containing micelles. Later interdiffusion of amine containing molecules in the epoxy containing micelles leads to full consumption of epoxy groups [115,116]. Film formation of both systems is observed and surface energies are determined in order to understand inherent properties of both systems which strongly differ from each other.

Electrochemical impedance spectroscopy (EIS) is a well known tool for determination of film structure and defect concentration [4,117]. The substrate/polymer interface is probed by ATR-IR spectroscopy. Penetration depth of ATR-IR spectroscopy depends on the wavelength. It is in the range of 250 to 850 nm [51,118]. In this depth range solidification is delayed compared to the bulk as shown by Possart et al. [40].

4.1.1 Bulk and interface reaction during film formation

Hardening of the polymer layer occurs in parallel to the evaporation of the water or organic solvent [116,115,119]. Impedance measurements were performed after immersing the polymer covered steel substrate for 10 min in borate buffer. Daily EIS measurements were performed from one to seven days after application of the water borne polymer (Fig. 4-1a and Fig. 4-1b) and up to nine days for the solvent borne polymer (Fig. 4-1c and Fig. 4-1d). The measurements were performed on different positions on the sample surface. Fig. 4-1a to

Fig. 4-1d display the Bode plots of the water and solvent borne coatings. The increasing coating impedance is related to the film formation process: the formation of the three-dimensional polymer network leads to a decreasing concentration of defects. At the same time the phase shift decreases towards 90° in the frequency region above 1 kHz.

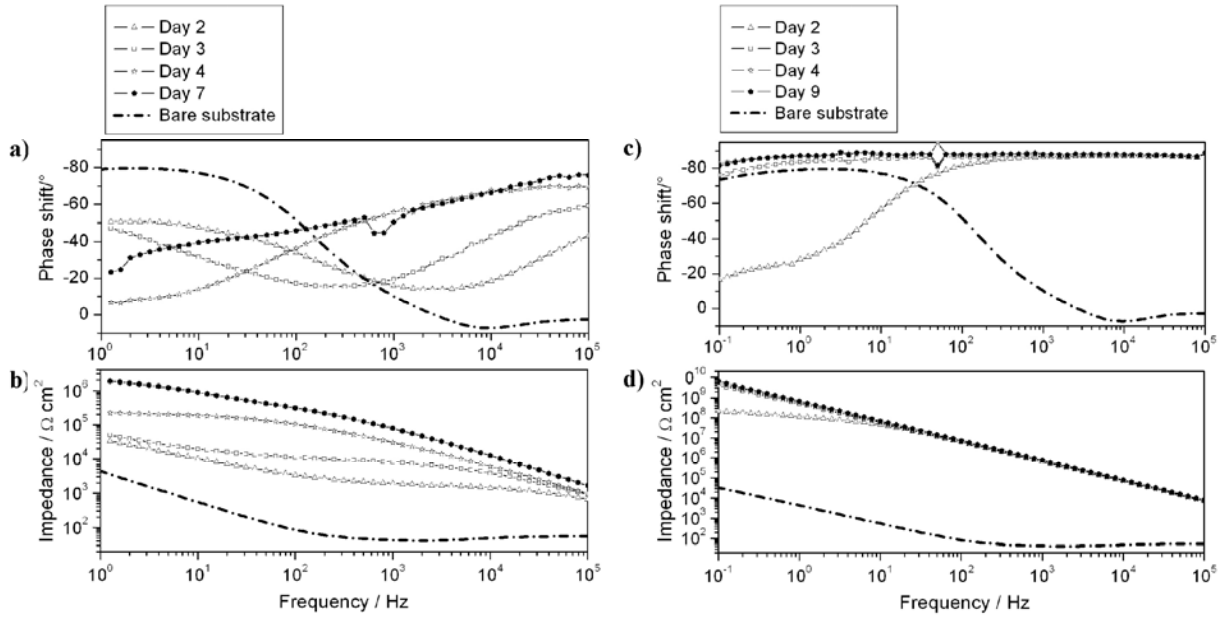

Fig. 4-1: Bode plots of water and solvent borne polymer during film formation and hardening. a) Phase shift and b) impedance of water borne polymer. c) Phase shift and d) impedance of solvent borne polymer.

The Bode plot was determined theoretically for an intact and a defective coating by Mansfeld [117]. The model circuit called Randles cell is displayed in Fig. 4-2a. The model circuit of the intact coating consists of the electrolyte resistance R_{el}, the pore resistance R_{Po} and coating capacitance C_C. The phase shift of 0° indicates purely resistive behaviour of the electric circuit at the frequency 10 kHz in the Bode plot of Fig. 4-1a. Therefore, the electrolyte resistance of $80\ \Omega cm^2$ is given at 10 kHz for the bare substrate. The coating capacitance is given where the phase shift is between -80° and -90°. In Fig. 4-1c the solvent borne coating shows capacitive behaviour over the whole range of measurement. The capacitance influences the tilt of the increasing impedance. The pore resistance influences the Bode plot at low frequencies around 1 Hz. Fig. 4-2b shows the extension of the Randles cell to defective coatings. Defects are characterised by a free sample surface area with a corresponding polarisation resistance R_P and the double layer capacitance C_{dl}.

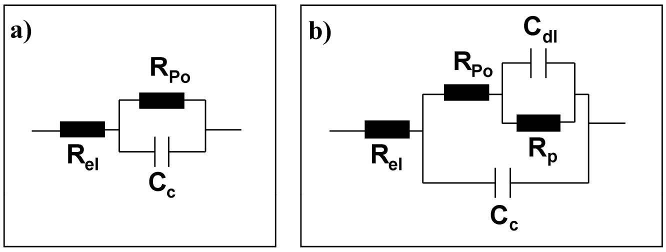

Fig. 4-2: a) Randles cell and b) modified Randles cell as model for impedance response of intact and defective coating.

Fig. 4-1a and Fig. 4-1b illustrate the Bode plot of the water borne polymer after two, three, four and seven days. The phase graphs of the water borne polymer show a characteristic change with increasing hardening time in Fig. 4-1a. The phase shift of -10° shifts from 30 kHz at day 2 towards 3 Hz on day 4. The place of the phase shift near 0° indicates the value of pore resistance according to the Randles cell. Therefore, the pore resistance increases from 2 kHz on day 2 to 200 kHz on day 4. After seven days of curing the phase shift of -10° is below 1 Hz and out of the measured range. Consequently, the influence of defects diminishes towards seven days of hardening. The coating behaviour does not further change at longer curing periods.

After seven days the polymer was annealed for 1 h at 60 °C. Fig. 4-7a displays the Bode plot of the initial measurement at t = 6 min which underlines that the impedance was distinctly increased by up to three orders of magnitude for low frequencies during annealing.

Fig. 4-1c and Fig. 4-1d show the change of Bode plot with film formation for the solvent borne polymer. In this case measurements are compared for two, three, four and nine days of hardening at 50% relative humidity. After two days low pore resistance is the reason for smaller impedance compared to later measurements. During hardening the pore resistance increases and after three days the coating behaviour is completely capacitive, indicated by a phase angle of -90° and the linear slope of the impedance. A further decrease of the phase shift is observed after four days which remains constant at longer periods of film formation. the pore resistance of the solvent borne polymer exceeds 10^9 Ω cm^2 compared to 10^6 Ω cm^2 for the water borne polymer.

Chemical reactions during film formation were analysed by ATR-IR spectroscopy [40,51,120]. Hardening at the polymer/substrate interface is influenced by the presence and surface properties of the substrate. The substrate influences the network formation in the first few hundred nanometers [40,121]. Penetration depth of ATR geometry reports therefore reactions in the interphase (see also schematic in Fig. 4-6). The bulk reaction of epoxy and amine component of the water borne polymer results in formation of hydroxide and secondary amide (Fig. 4-3). In the solvent borne polymer an amide group is formed. In ATR-IR spectra the chemical reaction is superimposed by water or solvent evaporation. Simultaneous approximation of the polymer to the ATR crystal surface leads to an increase of almost all peaks.

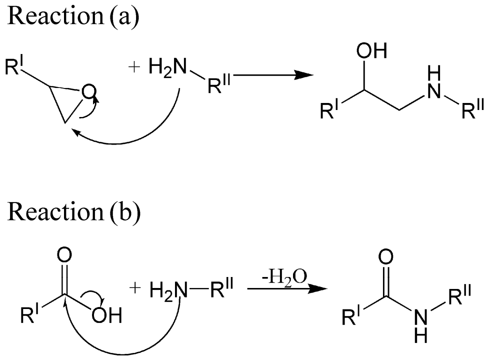

Fig. 4-3: Chemical reaction of amine and epoxy component of water borne polymer (a) and solvent borne polymer (b).

Fig. 4-4a shows spectra of water borne polymer before and after hardening and difference spectra of different periods of hardening in the inlets. Difference spectra are measured using the dry polymer film as a reference. Decrease of the ν(OH) peak between 3600 cm^{-1} and 3100 cm^{-1} with time is displayed in Fig. 4-4c. Concentration of water in the substrate/polymer interphase reaches a minimum after one day. In the inlet of Fig. 4-4a an enlarged picture of the ν(OH) peak is given. Before film formation and at long drying periods a shoulder is visible at 3300 cm^{-1} which can be assigned to NH stretching. NH groups are consumed during the reaction. Before film formation, NH_2 and OH stretch of water cause a broad peak between 3700 cm^{-1} and 3100 cm^{-1}. After film formation new OH groups show hydrogen bonding in a similar range. Intensity increase of $\nu_{as}(CH_3)$ at 2966 cm^{-1}, $\nu_{as}(CH_2)$ at 2930 cm^{-1} during film formation is detected on top of a tilted baseline [122]. The large amount of evaporating water influences the baseline even in the area of CH stretching between 3090 cm^{-1} and 2870 cm^{-1}. Difference spectra show also an increase of $\nu_s(CH_2)$ at 2820 cm^{-1}.The $\nu_s(CH_3)$ peak area at 2870 cm^{-1} remains constant [122]. The growing peak at 3040 cm^{-1} gives indication on the existence of an aromatic OH group.

Peaks at 1608 cm^{-1}, 1580 cm^{-1} and 1509 cm^{-1} belong to ν(CC) in aryl groups. At 1458 cm^{-1} scissoring and asymmetric deformation of CH_2 and CH_3 is detected. Difference spectra in the inlet show that the peak at 1246 cm^{-1} consists of vibrations at 1248 cm^{-1}, 1233 cm^{-1} and 1217 cm^{-1}. Stretching vibration of aryl ether (=COC) is detected in this region.

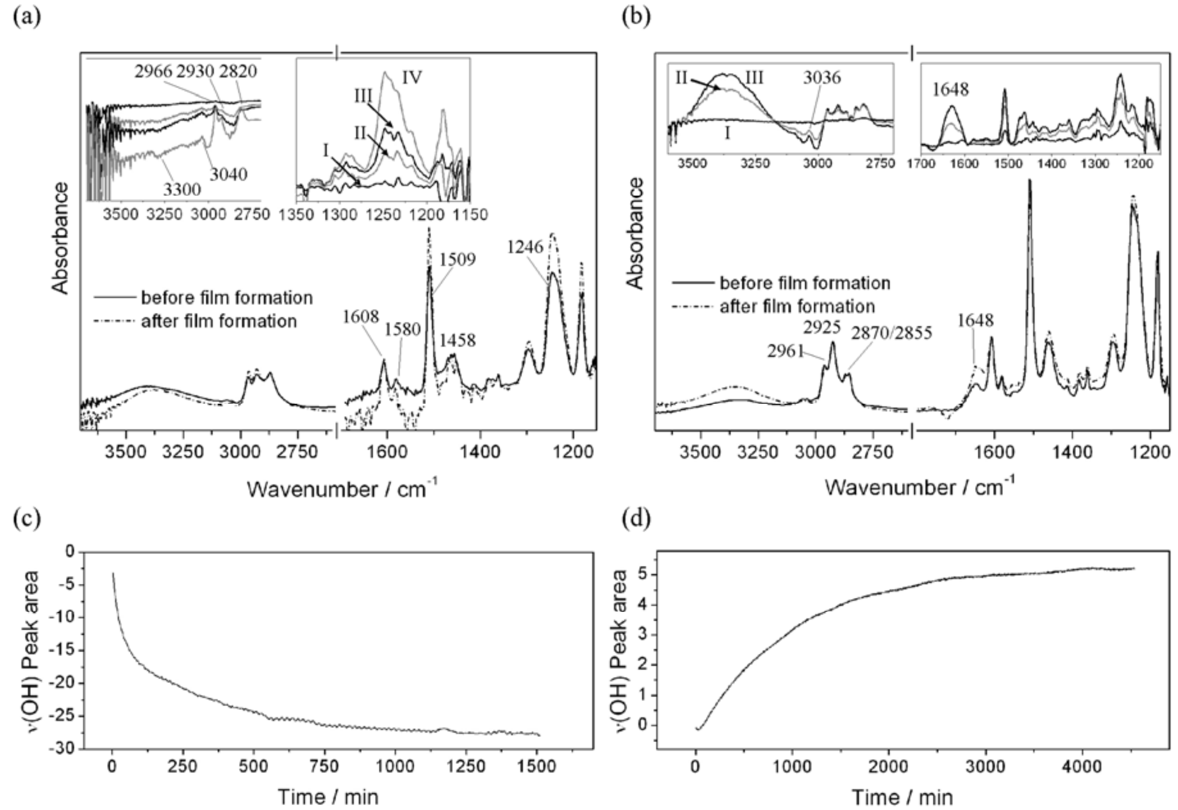

Fig. 4-4: (a) ATR-IR spectra before and after film formation of water borne polymer. Spectra I,II,III and IV in the inlets are difference spectra at 1 min, 40 min, 100 min and 1500 min, related to the polymer before drying. Time zero is 30 min after polymer application. (b) ATR-IR spectra of solvent borne polymer before and after film formation. Inlets show difference spectra I, II and III at 40 min, 1000 min and 4000 min of hardening. (c) Progression of the ν(OH) peak area during hardening of water borne polymer and (d) solvent borne polymer.

Table 4-1:Assignment of IR peaks in Fig. 4-4 (ν - stretching vibration, δ – deformation vibration, sciss - scissoring vibration; indices: s - symmetric, as - asymmetric, ip - in plane vibration, op - out of plane vibration)

Wavenumber [cm^{-1}]	Assignment
3600 - 3100	ν(OH)
3040 - 3036	ν(CH) aromatic group
2966 - 2960	$\nu_{as}(CH_3)$
2944 - 2925	$\nu_{as}(CH_2)$
2866 - 2820	$\nu_s(CH_3)$
1648 - 1629	δ(OH)
1608	ν(CC) aryl group
1580	ν(CC) aryl group
1509	ν(CC) aryl group
1458	sciss(CH_2) + $\delta_{as}(CH_2)$; sciss(CH_3) + $\delta_{as}(CH_3)$
1246-1242	ν(COC) aryl ether

Fig. 4-4b shows ATR-IR spectra of solvent borne polymer before and after film formation. In general, IR spectra of the applied water and solvent polymers strongly resemble each other. In case of solvent borne polymer the broad peak between 3600 cm^{-1} and 3100 cm^{-1} increases in the higher wavelength region due to formation of water in the amide reaction. Nevertheless difference spectra exhibit a decreasing peak area in the lower wavelength region because of consumption of amines (see inlet of Fig. 4-4b). In this region increasing peaks around 3036 cm^{-1} display the approach of aromatic groups (ν(CH)) to the ATR crystal surface. The CH stretching region shows further $\nu_{as}(CH_3)$ at 2961 cm^{-1}, $\nu_{as}(CH_2)$ at 2925 cm^{-1}, $\nu_s(CH_3)$ at 2870 cm^{-1} and $\nu_s(CH_2)$ at 2855 cm^{-1}. The difference spectra show a slight increase but constant intensity ratios. Peaks between 1700 cm^{-1} and 1100 cm^{-1} can be assigned similarly to the water borne polymer. The main difference is the peak at 1648 cm^{-1} which results from the C=O stretch of the newly formed amide group. The amide band II at 1540 cm^{-1} which stands for deformation and stretching vibrations involving NH group of the amide group is not detected. This accounts for the detection of a disubstituted amide. Termination of curing reaction can be linked to the progression of ν(OH) peak area (Fig. 4-4d). After three days a stationary concentration is reached.

EIS and ATR-IR measurements show differences in film formation periods for the water borne polymer. After one day chemical reaction at the interface seems to be concluded but impedance measurements show different bulk behaviour. Interphase processes reported by Possart [40] can be the reason for earlier termination of the reaction. A new type of OH groups is generated from epoxies during the reaction and comparison of ν(OH) peak and progression of ether band at 1246 cm^{-1} shows, that ν(OH) peak is still decreasing when ether band already reached a constant level. The solvent borne polymer exhibits comparable bulk and interphase curing periods of three to four days.

4.1.2 Surface energy during film formation

The surface energy of polymers is a criterion for their wettability. When wetting of the polymer surface occurs, it is succeded by water uptake. Therefore, low wettability is desired in corrosion protection in order to delay water uptake in the corrosion protection polymer. Surface chemistry of water and solvent borne polymers is expected to change during drying. In neutral environments such as air, the thermodynamics of the polymer system will attempt to minimize the surface free energy by orienting the surface into the non-polar region of the polymer. Low dispersive parts of the total surface energy and low total surface energy account for low wetting. Dispersive and polar interactions can be separated using the Owens-Wendt approach which is based on Fowkes surface tension theory [57]. Static contact angles of deionised water, ethylene glycol and diiodomethane were used to calculate surface energies according to Correia et al. [123] (see chapter 3.1.5).

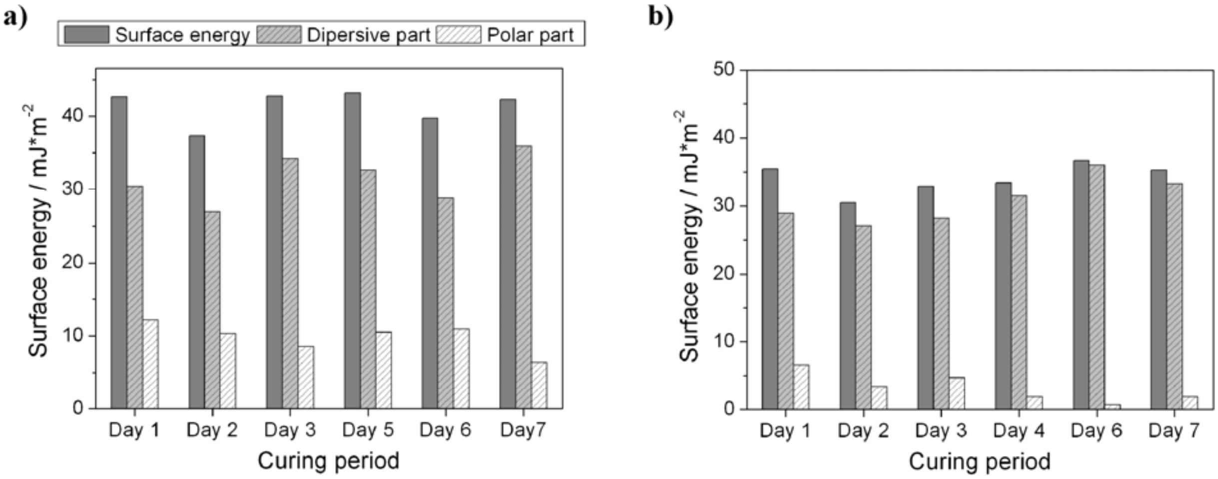

Fig. 4-5: Surface energies during seven days of film formation and hardening of the water borne (a) and solvent borne (b) polymers. The maximum standard deviation is 2.8 mJ/m^2.

Total surface energies of polymers are typically between 20 and 40 mJ/m^2 [124]. The water borne polymer exhibits surface energies in the range of 42 mJ/m^2. The polar part is 9 mJ/m^2 and the dispersive part is equal to 33 mJ/m^2. No clear trend depending on the curing period is illustrated in Fig. 4-5a. In contrast, decreasing polar contributions are detected for the solvent borne polymer while the total surface energy does not show a trend. The polar part is 3 mJ/m^2 and the dispersive part 30 mJ/m^2 (Fig. 4-5b). The considerably larger polar part of the water borne polymer can be the reason for the 10 mJ/m^2 higher surface energy compared to the solvent borne polymer. At the beginning of film formation water is present in the film, lateron water molecules remain in the polar parts of the polymer microstructures. The surface structure that is formed after one day does not change at longer curing periods.

4.2 Water uptake and diffusion

De-adhesion processes at polymer/oxide/metal interfaces are commonly connected to the interfacial incorporation of water and hydrated ions. Water diffusion via free volumes or directly through the polymer matrix itself takes place even for defect free films. Such a water uptake results in a change of the viscoelastic properties of the polymer and in its plastification. Adsorption of water molecules is energetically favoured in comparison to secondary forces between coating and substrate surface and is therefore connected to a loss of polymer adhesion to the substrate [12,125-127]. This effect will depend on the prevalent polymer/oxide bonding energy. Often water diffusion coefficients and the water uptake of the polymer films are used to characterise their barrier properties. In particular electrochemical impedance spectroscopy [51,120,128-132] and ATR-IR spectroscopy [51,120,133-135] were applied for the analysis of these values. Fieldson and Barbari [133] applied one-dimensional Fickian diffusion to ATR geometry and gave a means to determine diffusion coefficient.

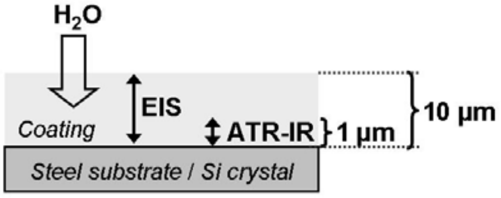

Fig. 4-6: Determination of bulk and interphasial water uptake by electrochemical impedance spectroscopy (EIS) and FTIR-ATR spectroscopy (ATR-IR).

ATR-IR and impedance measurements display different parts of the polymer: interphase or the bulk. Therefore, water uptake determined by EIS will be called bulk water uptake (Fig. 4-6).

4.2.1 EIS study

After seven days of hardening the water borne polymer was annealed for 1 h at 60°C and then exposed to a borate buffer solution to investigate its barrier properties towards water ingress. Fig. 4-7a and Fig. 4-7b display the change of the Bode plots with time. They resemble a non-water based epoxy-amine coating with barrier properties similar to the solvent borne polymer displayed in Fig. 4-8 [51]. However, the phase does not drop abruptly at low frequencies [51], but decreases uniformly between 3000 Hz and 0.1 Hz. These characteristics more and more dominate the Bode plots during the subsequent stages of water uptake. A decrease of the impedance can be observed in the whole frequency range (Fig. 4-7). This indicates a decreasing barrier function of the film at exposure times in the range of one day [117]. Obviously some coating pores and micro cracks develop in the polymer layer [98,143]. The common fit model used for the corrosion protection coatings displayed in Fig. 4-2 does not perfectly reproduce the behaviour of the water borne polymer. Bierwagen et al. [144] show the behaviour of polymers at rising temperature. No pores are formed, but the decrease of phase shift occurs at higher frequencies. In case of Fig. 4-8 the capacitive behaviour shifts towards 10 and 100 kHz out of the measured range. Bierwagen suggests that "…water dissolves partially in the film, plasticizes the film, lowers its T_g…" [129]. Consequently, it can be carefully interpreted from the impedance measurement that the coating structure shows a plasticised polymer structure.

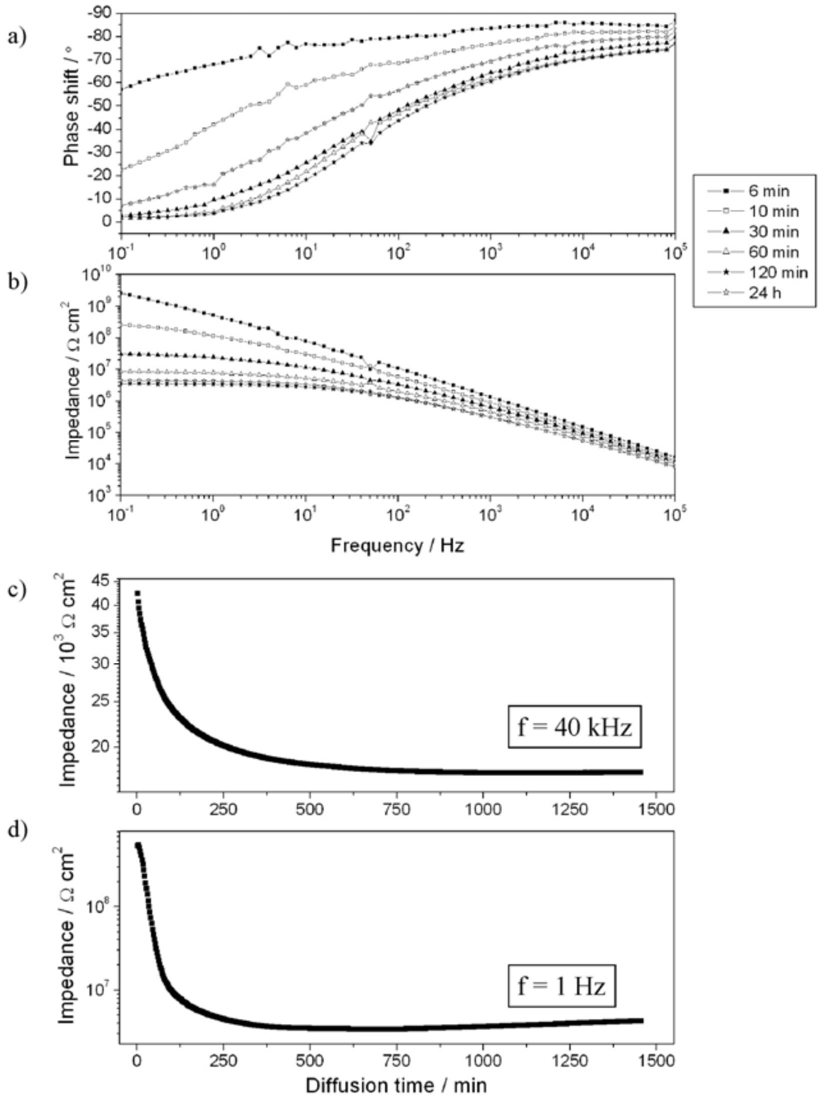

Fig. 4-7: Water uptake of epoxy-amine layers on steel substrates after drying and annealing. Typical development of the Bode plots with time: a) phase shift and b) impedance. c) Development of the coating impedance with time, displayed for 40 kHz and d) for 1 Hz.

The frequency region higher than 10 kHz is used for determination of water uptake. Usually low phase angles around -80° to -90° in this region result from purely capacitive behaviour of the polymer. However, impedance measurements of the water borne polymer show phase shifts around -70° at 40 kHz in the Bode plot (Fig. 4-7) after 60 min of immersion in electrolyte. These phase angles result from a capacitive behaviour which is overlayed by resistive parts. Fig. 4-7c illustrates the progression of impedance at 40 kHz. A constant impedance level is reached when the sample is exposed to the borate buffer solution for 700 min. The Brasher-Kingsbury approach would give a value of water uptake which largely exceeds 8 % [95]. It is very high compared to e.g. 2.5 % to 4 % reported for solvent based epoxy-amine coatings [51,145]. Therefore, also the determination of the diffusion coefficient is difficult. Deviations do not only occur due to the resistive contribution to the capacitance value, but also because of swelling and changes in the polymer due to high water uptake and because of the method of fitting the short-term linear region of capacity with time.

The solvent borne polymer shows an ideal coating behaviour even after one day of immersion into borate buffer (Fig. 4-8a). Impedance at 0.1 Hz is about 10^9 Ωcm^2 compared to 10^7 Ωcm^2 for the water borne polymer at similar coating thicknesses. The diffusion coefficient is at $1.5*10^{-10}$ cm^2/s. Fig. 4-8b shows progression of capacitance during water uptake, calculated at 40 kHz. Hinderliter reports a similar shape of capacitance curves and correlates the decrease after reaching a maximum with polymer reorganisation and redistribution of water within the coating and homogenisation [24]. He reports this asymmetry for wetting and drying cycles. For the simulation of atmospheric weathering performance, several wet-dry cycles should be compared. Hinderliter et al. [24] indicate that coatings are altered by the first wetting cycles. The water uptake of the solvent borne polymer reaches 3 ± 1 % which is obviously lower than for the water borne polymer.

Van Westing et al. explain the capacitance behaviour observed for the solvent borne polymer in Fig. 4-8b with Case II diffusion which was described in chapter 2.1 [21]. At the first stages of diffusion ideal behaviour is observed, but when a critical concentration of water is reached, the starts swelling. The penetrating water molecule cannot be modelled by an inert molecule which was described as prerequisite for ideal diffusion. Water interacts with the polymer and causes a front of swelling which moves at constant rate. Thereby, a linear increase of the capacitance with immersion time is observed.

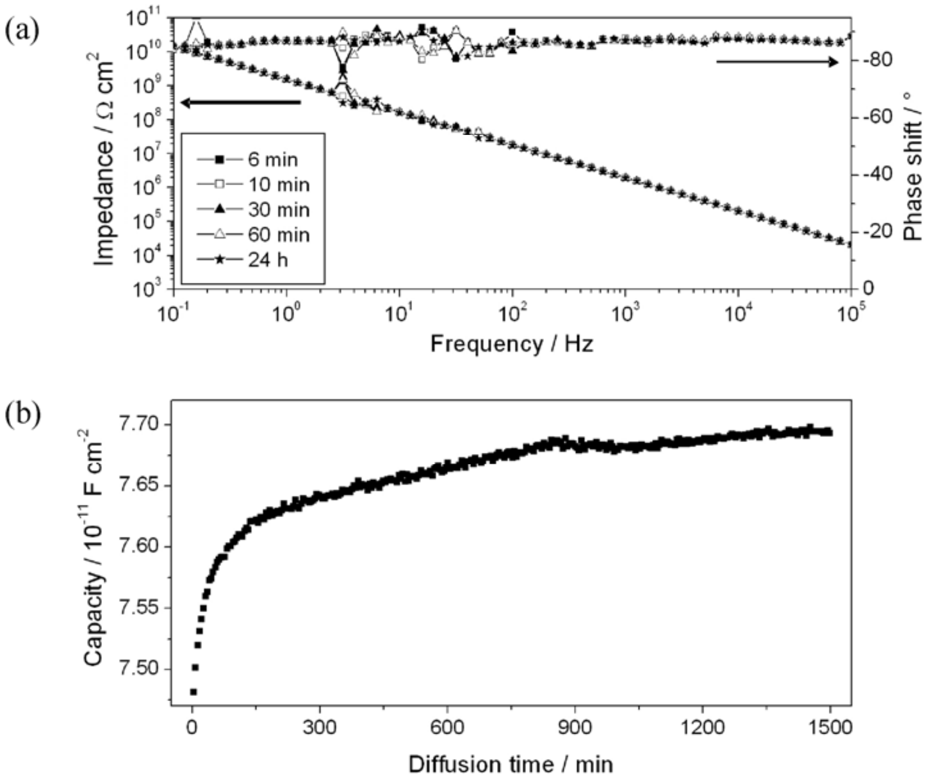

Fig. 4-8: (a) Bode plot of solvent borne polymer during immersion in borate buffer. (b) Capacity of solvent borne polymer during immersion in borate buffer.

4.2.2 ATR-IR study

ATR-IR experiments were performed to complement the EIS results. Silicon ATR crystals have been coated with the epoxy-amine polymers. The samples were exposed to borate buffer solution again and the increase of the interfacial water activity was detected by tracking the resulting changes of the ν(O-H) peak intensity. Often D_2O has been used instead of water, because D-O stretching at 2500 cm^{-1} does not interfere with other peaks [51]. On the other hand D-H isotope exchange influences kinetics observed for D_2O uptake [149,150]. At room conditions a small amount of water is solved in the coating. A decrease of the ν(OH) peak is therefore detected together with the increase of ν(OD). Thus, H_2O was used in the following IR study.

Fig. 4-9a shows the changes in the water borne polymer during water uptake. The dry polymer was used as reference for the time dependent spectra. Fig. 4-9b displays the time dependent progression of ν(OH), ν(CH), ν(CC) and ν(COC) peak areas. The interphasial H_2O activity steeply increases during the first minutes of the experiment (peak area between 3650 cm^{-1} and 3160 cm^{-1}). It is similar to the change of the capacity during the initial stage of the EIS measurement (see Fig. 4-7c). However, for the subsequent stages of the ATR-IR experiment a linear and continuous increase and no saturation level of the water uptake is detectable. This points at an expansion of free volumes at the polymer/silicon interface which should be filled up with water in this case [99]. Simultaneously, swelling of the polymer can occur. During water uptake the polymer concentration at the ATR crystal surface decreases. Negative peaks in Fig. 4-9a can be assigned to the polymer as described in chapter 4.1.1. ν(OH) and ν(NH) at 3400 cm^{-1} and 3020 cm^{-1}, respectively increase during water uptake. Further, δ(OH) bending is detected at 1645 cm^{-1}. Although the spectrometer was purged with dry nitrogen during the measurement, the rotation pattern overlaps the δ(OH) peak. At the same time the aromatic ν(CC) peak at 1508 cm^{-1} decreases to a minimum. In contrast, the ν(COC) peak at 1242 cm^{-1} shows a steady decrease due to partial hydrolysis of ether. Also the ν(CH) peak decreases steadily and seems to reflect the effect of the increasing water concentration at the interface. Consequently, wet de-adhesion effects have to be taken into account when further investigating the water borne epoxy-amine coating in a humid environment.

Water uptake of the water borne polymer shows also Fickian behaviour, but after one hour a second process overlaps the saturation value reached by Fickian diffusion. Strong interactions of water molecules with the polymer network cause further water uptake and lead to degradation of the polymer/substrate interphase. Generally, the amount of water uptake is proportional to the peak height or the peak area, which is eight times larger in the water borne polymer.

Diffusion in the solvent borne polymer shows Fickian behaviour (Fig. 4-9d). Water uptake was fitted by applying the approach of Fieldson and Barbari [133]. The diffusion coefficient correlates with the value determined by impedance spectroscopy as also shown by Vlasak et al. with the use of a combined EIS-ATR-IR cell [51]. A decreasing area of the polymer peaks is detected during water uptake (Fig. 4-9c) in the solvent borne polymer. Negative peaks are detected in the CH stretching region at 2925 cm^{-1} ($\nu_{as}(CH_2)$), 2867 cm^{-1} ($\nu_s(CH_3)$) and 2810 cm^{-1} (ν(CH) in CHO, aliphatic aldehydes). Peaks between 1550 cm^{-1} and 1200 cm^{-1} can be assigned according to Fig. 4-4b. The positive peak at 1246 cm^{-1} and the negative peak 1234 cm^{-1} can be explained by a shift of the ν(COC) peak position: the interaction of ether groups with ingressing water molecules causes a blue shift of the peak.

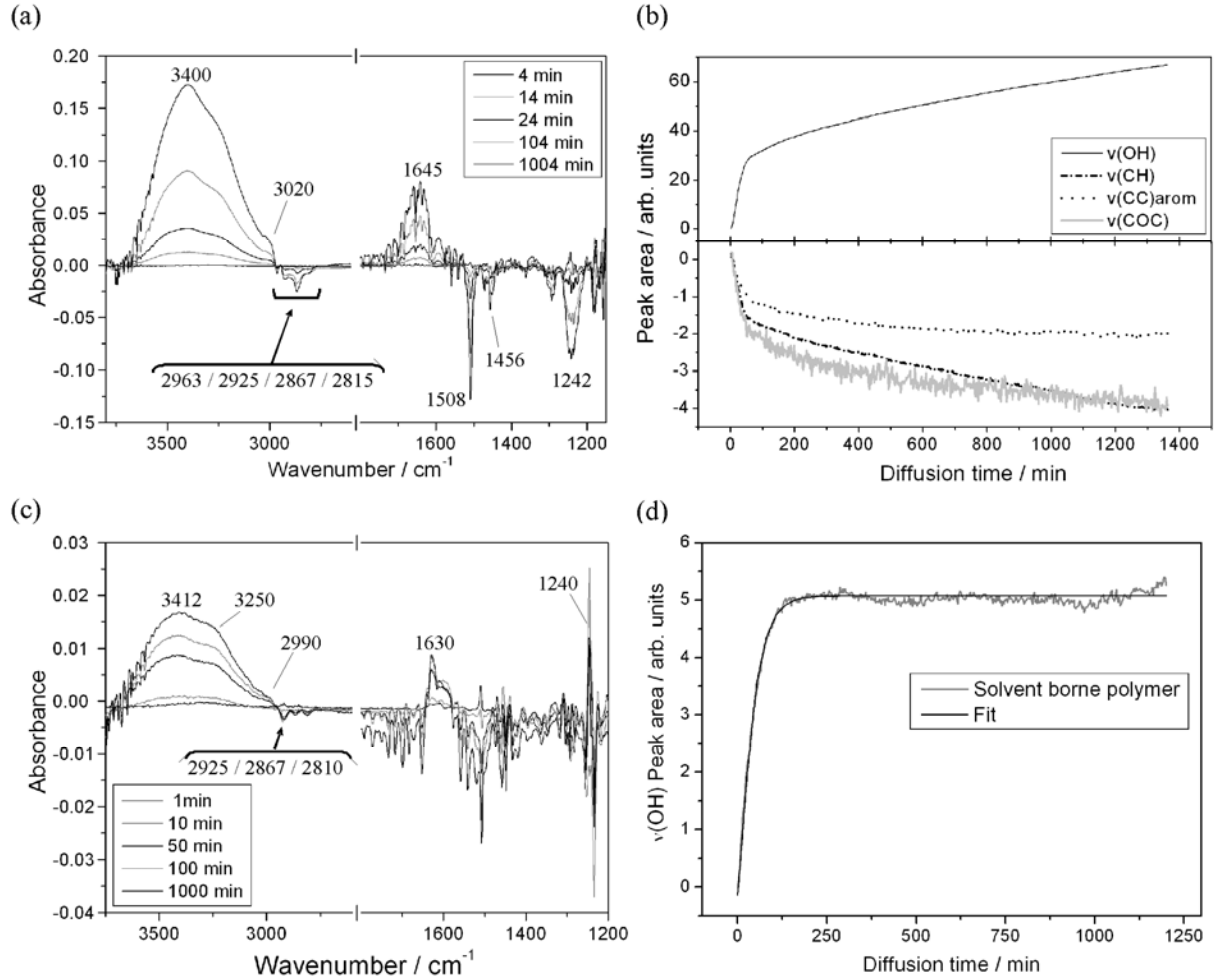

Fig. 4-9: (a) In-situ ATR-IR measurement of water uptake in water borne polymer: difference spectra and (b) progression of peak area of OH stretching between 3650 and 3160 cm^{-1}(ν(OH)), CH stretching between 2815 cm^{-1} and 3000 cm^{-1} (ν(CH)), CC stretching of aromatic groups at 1508 cm^{-1} (ν(CC)arom) and stretch of ether group at 1242 cm^{-1} (ν(COC)). (c) Water uptake in solvent borne polymer determined by ATR-IR spectroscopy: difference spectra related to the dry polymer and (d) progression of ν(OH) peak area between 3660 cm^{-1} and 3450 cm^{-1} and fit according to Fieldson and Barbari [133].

When water reaches the polymer/crystal interface, the ν(OH) band with the maximum at 3412 cm^{-1} and the δ(OH) band at 1630 cm^{-1} increase. The broad OH stretching in Fig. 4-9c displays shoulders at 3250 cm^{-1} and 2990 cm^{-1}. Interactions of OH groups with unreacted primary or secondary amine groups influence the band as well as different association states of water molecules [16,17,52,53]. The detected ν(OH) peaks can be quantitatively explained by the superposition of four Gaussian peaks according to Sutandar et al. [53]. The fit for the ν(OH) peak of the solvent borne polymer after saturation is shown in Fig. 4-10c. Fit values are given in the table of Fig. 4-10, the fit of liquid water as performed by Sutandar et al. is thereby used as a reference. The peaks in Fig. 4-10 are assigned according to Sutandar et al. and Cotugno et al., who explained the fit with the interaction of water molecules with themselves or with the polymer [16,53]. They assigned i) H_2O monomers without H-bonding (unassociated water molecules), ii) H-bonded dimers or clusters and H-bonded wate molecules which specifically interact with the polymer network and iii) stronger H-bonded molecules with several types of interactions and therefore highly reduced mobility. Low mobility is additionally correlated to a higher plasticising effect. An additional peak was fitted around 3000 cm^{-1} in the difference spectra, in order to account for the influence of CH stretching vibrations.

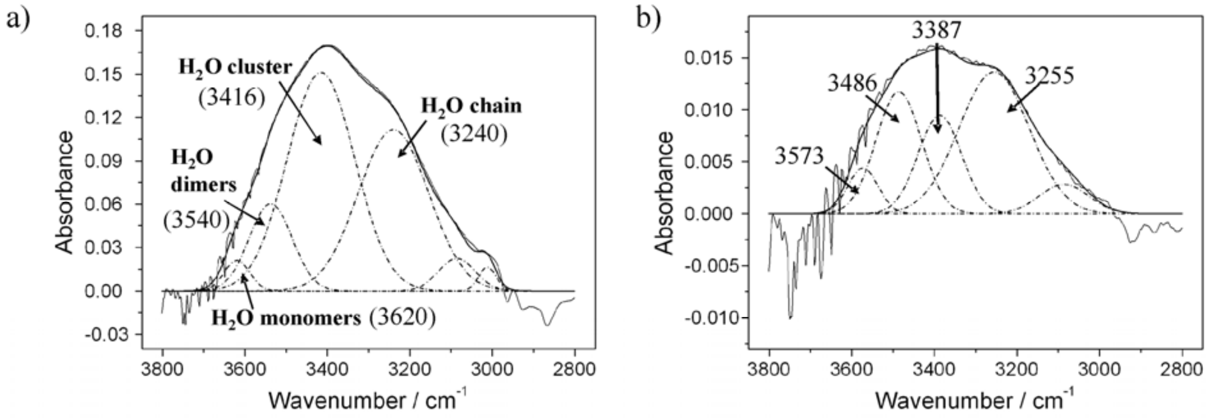

Liquid water		
Wavenumber [cm^{-1}]	FWHM [cm^{-1}]	Peak areas related to peak at 3246 cm^{-1}
3616	83	3
3536	138	13
3424	171	17
3246	386	100

Water borne polymer (a)			Solvent borne polymer (b)		
Wavenumber [cm^{-1}]	FWHM [cm^{-1}]	Peak areas related to peak at 3240 cm^{-1}	Wavenumber [cm^{-1}]	FWHM [cm^{-1}]	Peak areas related to peak at 3255 cm^{-1}
3620	73	7	3573	86	14
3540	123	33	3486	130	56
3416	193	130	3387	124	43
3240	201	100	3255	200	100

Fig. 4-10: Fit of ν(OH) peak after 1000 min immersion in borate buffer according to Sutandar et al. [53]: (a) water borne polymer and (b) solvent borne polymer. The table below gives FWHM values and peak areas of the OH peak fits in (a) and (b). The fit of liquid water is taken from [53] as a reference.

In general, the interaction of water with the polymer network differs for the water and the solvent borne polymer. The peak at 3416 cm^{-1} in Fig. 4-10a indicates large contributions of H_2O clusters in the water borne polymer. The contributions of H_2O dimers and clusters are clearly different in the ν(OH) peak of water borne and solvent borne polymers. In the solvent borne polymer the contribution of hydrogen-bonded dimers or clusters at 3486 cm^{-1} is larger than in liquid water (Fig. 4-10b). Around 3250 cm^{-1} also hydrogen bonded amine groups contribute to the absorbance of H-bonded molecules. Although the water uptake is much larger in the water borne polymer, a continuous water film is not observed even after longer immersion: similar to the observations of Vlasak et al. [51] also in this case the contribution of the peak fitted at 3240 cm^{-1} for associated water chains (Fig. 4-10a) is much smaller than in liquid water.

Drying after water uptake was analysed on polymers on steel substrates by means of IR spectroscopy in 30° reflection geometry. The wet water borne polymer spectrum is displayed in Fig. 4-11a, difference spectra during drying are displayed in Fig. 4-11b. Measured peaks are broadened due to the few micrometer thick film. Peaks of difference spectra with the wet film as reference can be compared to the fitted components of water uptake. They show how water molecules are aggregated at high water concentrations in the polymer bulk.

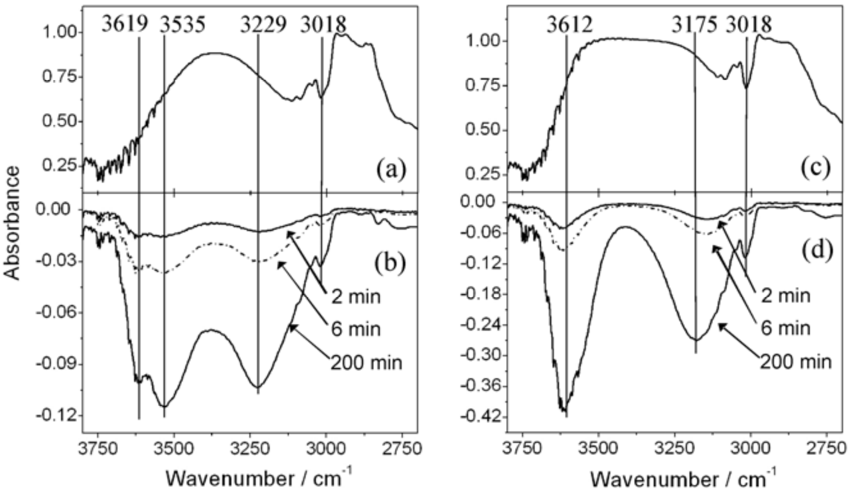

Fig. 4-11: Drying of solvent and water borne polymer on steel substrates, IR spectroscopy in 30° reflection mode. a) IR spectrum of solvent borne polymer after exposure to >90% rel. hum. b) Difference spectra of solvent borne polymer between 2 and 200 min of drying at room conditions. c) IR spectrum of water borne polymer after exposure to >90% rel. hum. d) Difference spectra of water borne polymer between 4 and 200 min of drying at room conditions.

OH stretch and OH bend show decreasing intensities at 3612 cm^{-1}, 3175 cm^{-1}, 1645 cm^{-1} in the water borne polymer (Fig. 4-11). This means that water accumulated as monomers and strongly H-bonded water diffuses out of the polymer. Water which interacts specifically with the polymer network does not decrease strongly. Again the peak at 3175 cm^{-1} is contributed by H-bonded NH stretch.

Also, the solvent borne polymer shows decreasing amount of monomeric and weakly interacting water molecules at 3613 cm^{-1} and 3532 cm^{-1} and δ(OH) at 1629 cm^{-1} (Fig. 4-11a and Fig. 4-11b). Again, highly H-bonded water decreases (3225 cm^{-1}).

4.3 Polymer/substrate interface and adhesion

Failure of polymer/metal bonding in presence of water is reported by Gledhill et al. [151]. The thermodynamical work of adhesion W_A is required to separate two phases forming an interface. In absence of chemisorption and interdiffusion it can be related to the surface free energies by the Young-Dupré equation:

$$W_A = \gamma_{sl} (\cos \alpha - 1) \tag{4.1}$$

(with γ_{sl} solid-liquid interfacial tension and α contact angle). In inert atmosphere W_A has a large positive value indicating thermodynamic stability, but with liquid water it may be negative and lead to dissociation. This is a simplified model because chemisorption cannot be neglected in coating adhesion.

At high relative humidity wet delamination was observed for the water and the solvent borne polymers. Peel forces were determined by a 90°-peel test after exposure to humid air. After partial drying bonds re-establishing of strong interface interactions are crucial for corrosion resistance, which is modelled by dry-wet cycles [153]. After peel tests it was possible to analyse substrate surface and the buried polymer surface at different drying stages by XPS and SEM/EDX (Fig. 4-12).

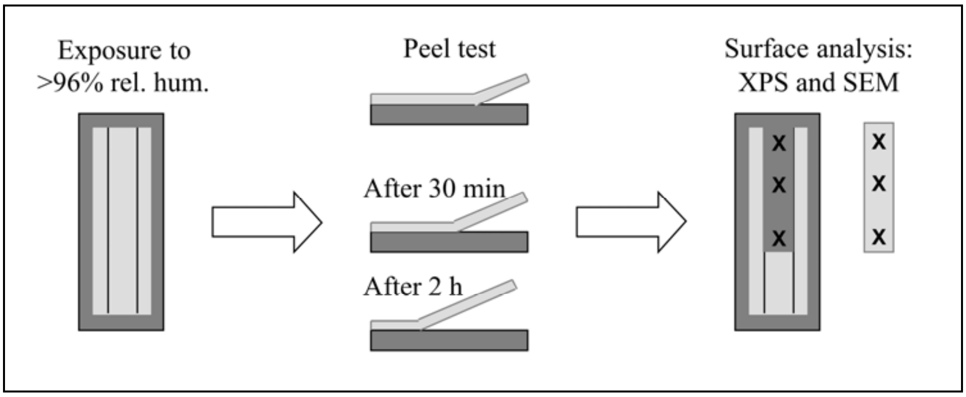

Fig. 4-12: Determination of peel force and interface composition.

Loss of adhesion after five days of exposure to high relative humidity (> 95%) resulted in low peeling forces of the water borne polymer around 0.01 $\mathrm{Nmm^{-1}}$. Hinderliter et al. [24] show that water ingress and egress happen in the same time regime. During drying at room conditions an increase of peel forces was not always detected in the range of four hours although the water uptake is accomplished after one hour. The solvent borne polymer always shows the start of re-bonding after one hour of drying due to increasing peel force. Peel forces are 0.02 $\mathrm{Nmm^{-1}}$ in the wet state of the solvent borne polymer and increase towards 0.07 $\mathrm{Nmm\text{-}^{1}}$ after drying (Fig. 4-13).

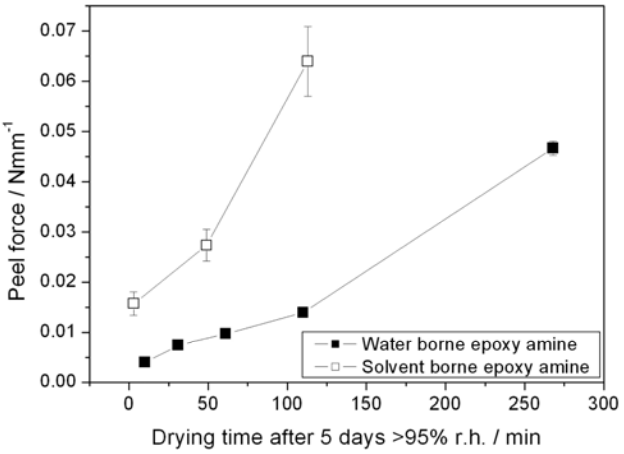

Fig. 4-13: Peel test of solvent and water borne polymer after exposure to high humidity for 5 days and drying for the displayed periods.

Polymeric residues of the water and solvent borne polymer on the steel substrate were analysed by XPS and SEM after the peel test, as displayed in Fig. 4-12. Thereby, the steel surfaces do not vary with drying time although re-bonding to the substrate occurred in case of the solvent borne polymer, as described before. Also at the water borne polymer/steel interface adhesive failure exceeds the cohesive failure of the polymer.

The XPS analysis of the steel surface after peeling the water borne polymer shows a lower surface concentration of iron than the alkaline cleaned, uncoated steel surface (Fig. 4-14a). In Fig. 4-14b the iron surface fraction is similar to the uncoated steel surface. The peak centre of the Fe $2p_{3/2}$ high resolution spectra is detected at 710.8 eV in Fig. 4-14b, Fig. 4-14c and Fig. 4-14d indicating Fe^{2+} and Fe^{3+} species on the steel surface. The ratio of peak areas of the Fe^0 peak at 707 eV and the oxidised iron peak at 710.8 eV in the high resolution Fe $2p_{3/2}$ spectra (Fig. 4-14b, Fig. 4-14c and Fig. 4-14d) displays varying oxidation of the substrate as well as different coverage with polymeric residues. A higher Fe^0 fraction indicates lower surface oxidation and coverage of the uncoated steel surface in Fig. 4-14b compared to the peeled surfaces (Fig. 4-14c and Fig. 4-14d).

Less oxygen is present at the polymer/substrate interface of the solvent borne polymer than at the interface with the water borne polymer (Fig. 4-14a). The higher O 1s amount present on the substrate surface after peeling of the water borne polymer can result from interaction of iron oxide with water. As a result, beneath the solvent borne polymer a thinner iron oxide layer is present. The oxygen signal at the interface of steel and solvent borne polymer mostly originates from adsorbates and carbonates. This is also supported by the C 1s spectrum showing carbon at high oxidation states (carbonates).

The amount of C 1s is higher on the peeled surfaces (Fig. 4-14, Fig. 4-14c and Fig. 4-14d) than on the bare substrate (Fig. 4-14b). Aromatic components of the polymer at 284.3 eV (Fig. 4-14e and Fig. 4-14f) are not detected on the substrate surface after peeling of water and solvent borne polymer. This indicates that the plain of failure is next to the substrate surface as also no iron is detected on the polymer surface. O 1s spectra of the iron surface clearly differ from the oxygen composition on the polymer surface: OH and C=O are detected at 531 eV and 532.4 eV (Fig. 4-14e and Fig. 4-14f), but an inverse intensity ratio is detected on steel and on the polymer surface. A small part of nitrogen present in the polymer is detected on the substrate surface after the peel test.

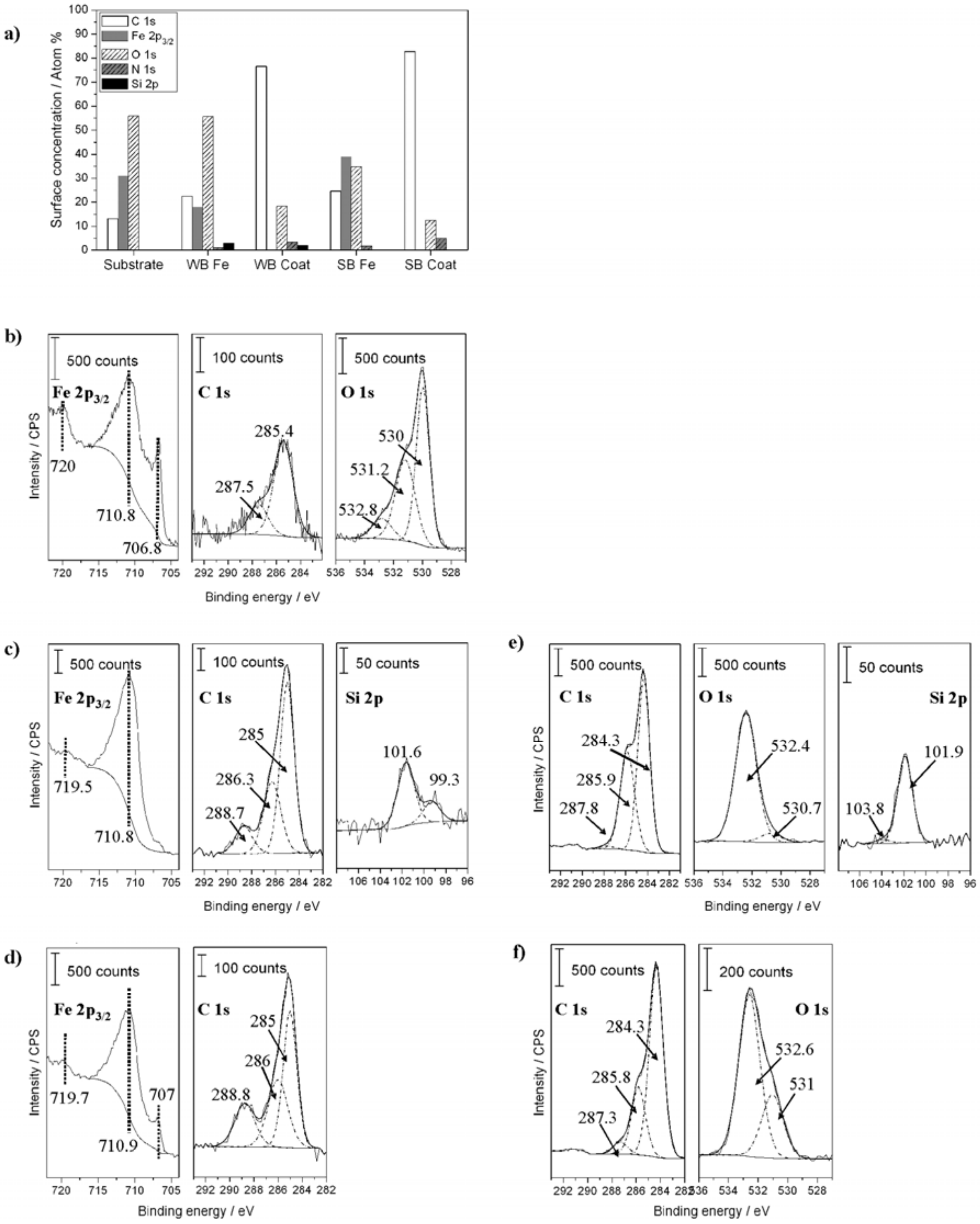

Fig. 4-14: XPS surface analysis after peel test of water and solvent borne polymer. a) Surface concentration of elements. b) Fe $2p_{3/2}$, C 1s and O 1s high resolution spectra of alkaline cleaned steel surface. c) Fe $2p_{3/2}$, C 1s and Si 2p high resolution spectra of steel surface after peeling water borne polymer. d) Fe $2p_{3/2}$ and C 1s high resolution spectra of steel surface after peeling solvent borne polymer. e) Water borne polymer surface after peel test. f) Solvent borne polymer surface after peel test.

Table 4-2: Assignment of XPS peaks in Fig. 4-14

Signal	Binding energy [eV]	Assignment
Si 2p	99.3	Si^0
	101.6 - 102	Si^{+II}
	102.8	Si^{+IIi}/ Si^{+Iv}
C 1s	284.3	Aromatic compound
	284.9 – 285.1	C-C, C-H
	286.1 – 286.7	C-O
	289	C=O
	291.7 - 292	π–π shake up satellite of aromatic compound
O 1s	530	Fe_2O_3
	531 – 531.4	OH
	531.9	C-O
	532.4 – 533.2	C=O, CO_3^{2-}, H_2O
	533.8	C=O, CO_3^{2-}
Fe 2p	706.8 - 707	Fe^0
	710.8	Fe^{2+}/Fe^{3+}

Silicon is detected at similar intensities on the substrate and on the polymer surface of water borne polymer. On the polymer the oxidation state is +II (101.9 eV) and on the substrate 0 at 99.3 eV and +II at 101.6 eV.

Organic residues on the surface are islands containing varying concentrations of carbon, oxygen and silicon (EDX). This means, that the organic residues are not necessarily a covering layer. A 100 x 100 μm^2 spot in XPS can include such an island or not. Therefore, SEM supplements the XPS analysis in this case.

4.4 Conclusions

Differences in the behaviour of the water and the solvent borne polymers both during film formation and water uptake were highlighted in this chapter. Film formation in the bulk and in the polymer/steel interphase occur on different time scales for the water borne polymer. The Detection of the chemical reaction is difficult due to simultaneous evaporation of water. Thereby, all polymer components approach the substrate surface and peak intensities grow. For the solvent borne polymer the chemical reaction is visible in the growth of the carbonyl peak of the amide group. The chemical reaction of the water borne polymer proceeds for one week, while hardening of the solvent borne polymer is concluded after four days. During hardening total surface energies do not change, but the polar part of the surface energy decreases.

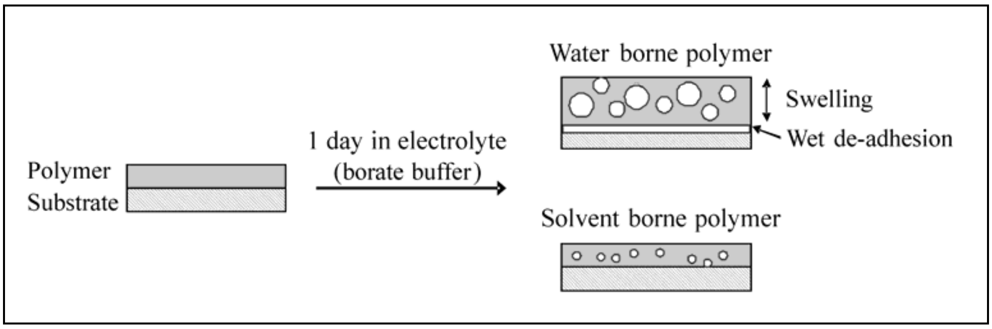

Fig. 4-15: Schematic - behaviour of water and solvent borne polymer during water uptake

Although the chemical composition of the water and the solvent borne polymers detected by ATR-IR spectroscopy is very similar, water uptake elucidates intrinsic differences. The amount of uptaken water on the one hand and the distribution of water species in the polymer on the other hand differ clearly. The Bode plots indicate good barrier properties towards water penetration due to high impedances of both polymers. However, the pore resistance of the solvent borne polymer is stable at 10^{10} Ωcm^2 during 24 hours of immersion into borate buffer, whereas the pore resistance of the water borne polymer is 10^9 Ωcm^2 and is decreasing to 10^6 Ωcm^2 after two hours of immersion. Furthermore, the Randles cell as model of the electric circuit applied for corrosion protection coatings does not explain the impedance behaviour of the water borne polymer because the water uptake determined by impedance spectroscopy exceeds 8 %. Furthermore, ATR-IR measurements display high water uptake in the interphase of the water borne polymer and the ATR crystal which indicates deviations in the determination of capacitance and water uptake from impedance data. Furthermore, low interface stability can influence the water uptake value, because a thin layer of water with high capacitance results in a two-layered system with increased capacitance.The impedance reaches a constant value after two hours of sample immersion into borate buffer, but Bode plots indicate plasticisation of the polymer. These processes must result in swelling of the water borne polymer.

The polymer structure and behaviour strongly depend on its hydrophilic or hydrophobic nature. Peel tests show that the polymer matrix alone cannot provide rebonding after interface destabilisation by water uptake. The IR data indicates that after Fickian water uptake the interphasial water concentration steadily increases in the water borne coating. The solvent borne polymer/steel interphase is more stable. Nevertheless, after several days water ingress lowers the peel forces. Chemical bonding of the solvent borne polymer is thereby not necessarily stronger, only the interphasial water concentration is much lower than in the water borne polymer.

5 Organosilane adhesion promoters in water and solvent borne epoxy-amine polymers

Coating additives are used in order to improve the interface stability of the polymer matrix. Adhesion promoters can be applied as primers or mixed to the polymer (chapter 2.3). The influence of APS and GPS on water uptake and interface stability of the solvent and the water borne polymers will be discussed in this chapter. The adhesion promoting function of organosilanes has been known for some decades [63]. If they are used as additives, Fickian diffusion of the organosilane molecules towards the interfaces is observed [86]. Abel and Watts performed studies of with GPS on Aluminium, where they observe segregation of the organosilane at the interfaces [155,156]. Also durability and performance of organosilane additives in degrading environment was studied [157,158].

Interfaces modified with adhesion promoting organosilanes are expected to be more stable in an environment of high water activity. Covalent bonds between polymer chains, GPS and the oxide layer are less sensitive to hydrolysis and provide a major contribution to the overall adhesion forces [63,86,155]. EIS and ATR-IR spectroscopy are used to investigate the barrier properties of the organosilane containing coatings. Ex-situ XPS, SEM and EDX measurements will be applied to analyse the interfacial composition after polymer de-adhesion in humid atmosphere. The received results are compared to the characteristics of the unmodified water and solvent borne epoxy-amine coatings that were described in chapter 4.

5.1 Water uptake of modified water and solvent borne coating

The water uptake was determined for APS and GPS as adhesion promoters. They were applied as primers from aqueous solution and as additives mixed to the polymer in different concentrations (0.5 wt%, 2.5 wt%, 5 wt%). The chemical structures of APS and GPS are displayed in Fig. 5-1. Wang et al. [18] report that modified systems exhibit different water uptake and can be more hydrophobic due to i) the hydrophobic interface with SiO_2 groups, ii) a hydrophobic surface and bulk because of consumption of hydroxyl groups during the reaction with the silane and the introduced hydrophobic rest of the organosilane, and iii) higher crosslinking in the bulk and thereby reduced free space. In contrast, primers are not expected to influence water uptake.

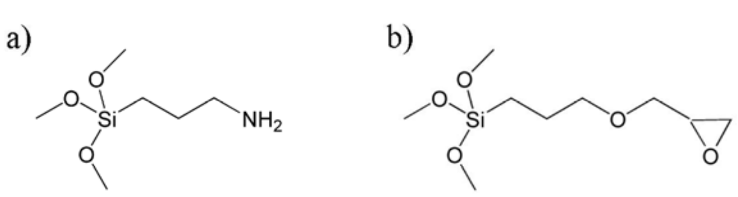

Fig. 5-1: a) 3-aminopropyl(trimethoxy)silane (APS). b) 3-glycidoxypropyl(trimethoxy)silane (GPS)

Water uptake and diffusion are again determined by ATR-IR spectroscopy and impedance measurements for the modified water and solvent borne polymers [159] and compared to the unmodified polymers. The peak area of OH stretching (ν(OH)) determined from ATR-IR data is proportional to the amount of water in the interphase according to the law of Beer and Lambert:

$$A = -\log_{10}\left(\frac{I}{I_0}\right) = -\varepsilon \cdot c \cdot d \tag{5.1}$$

(with A the absorbance, I the measured intensity, I_0 the reference intensity given by the sample background or by a reference state (dry state) of polymer, ε the dielectric constant of the sample, c the concentration and d the sample thickness). This expression was applied to the ATR geometry by Possart [40]. Lower water uptake in the interphase can be therefore directly deduced from ATR-IR data, as also penetration depths are similar in the observed polymer systems.

Influence of GPS and APS are discussed separately in the following chapters. As already discussed in chapter 4, water uptake is much higher in water borne polymer than in the solvent borne epoxy-amine polymers [51]. Therefore, diffusion coefficients of the water borne polymer cannot be calculated from the water uptake determined by ATR-IR spectroscopy in an eligible way using the approach of Fieldson and Barbari. However, the impedance data can be fitted according to [21] and thereby the diffusion coefficients can be determined.

5.1.1 Application of GPS as adhesion promoter

Water uptake of the water borne polymer determined from EIS data depends on GPS addition. Lower water uptake is measured with higher GPS content; with 5 wt% GPS the magnitude of solvent borne polymer is reached. This means that voids and micropores are reduced and the polymer network is densified by addition of the epoxy containing adhesion promoter. The water uptake of solvent borne polymer is in the expected range of 1% to 3% for all systems containing GPS. The interface stability is clearly enhanced by GPS in water borne polymer. APS addition leads to higher water uptake in the polymer/substrate interphase in water and solvent borne polymer.

Fig. 5-2a illustrates the development of the recorded Bode plots with time after addition of 2.5 wt% GPS. It was experienced that the general characteristics of the impedance and phase graphs are similar for the unmodified and GPS modified water borne polymer. The graph of Fig. 5-2b represents the time dependent development of the coating impedance at 31.6 kHz. Fig. 4-7c shows the same plot for the unmodified polymer. The two curves exhibit a strong but different initial impedance decrease and converge towards a constant value when the samples were exposed to the borate buffer solution for longer times. Both graphs do not point at a significant swelling of the polymers [96]. In case of the system modified with 2.5 wt% GPS the Brasher-Kingsbury equation for water uptake can be applied [95]. Approximately 8 % water uptake was determined at 31.6 kHz, where the phase remained nearly constant. The calculated diffusion coefficient is $4.5*10^{-9}$ cm^2/s for the 2.5 wt%-GPS modified water borne polymer.

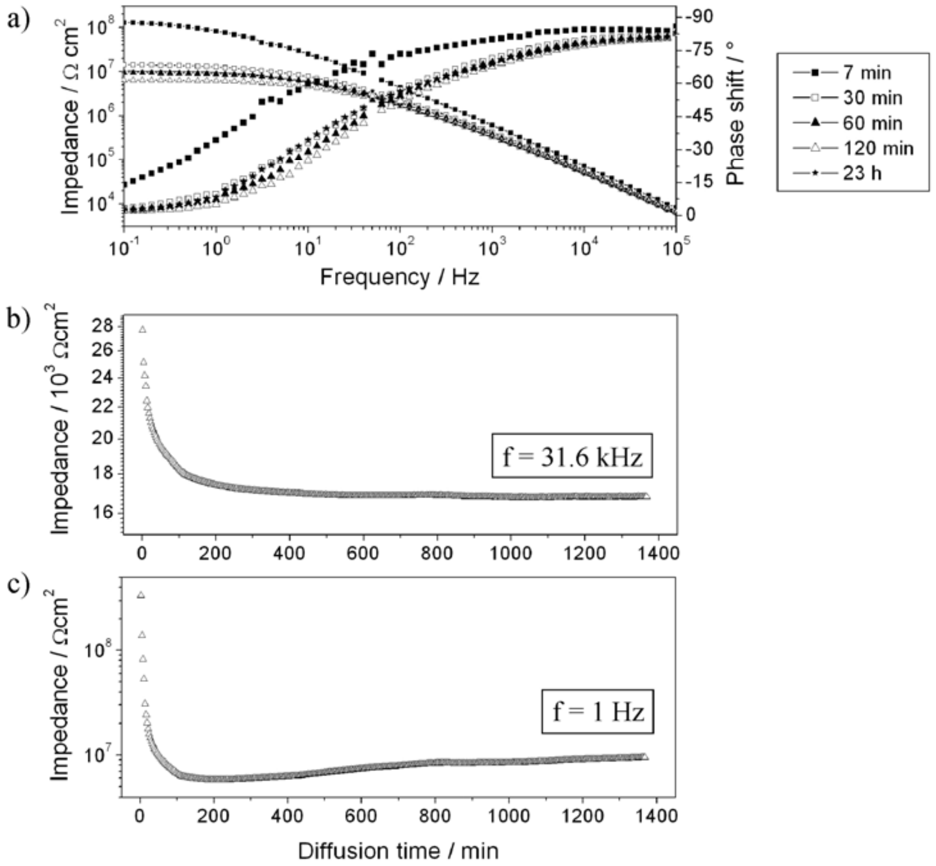

Fig. 5-2: Impedance measurement of water borne polymer containing 2.5 wt% GPS. a) Bode plot with increasing diffusion time in borate buffer. b) Impedance variation at 31.6 kHz and at c) at 1 Hz with increasing diffusion time.

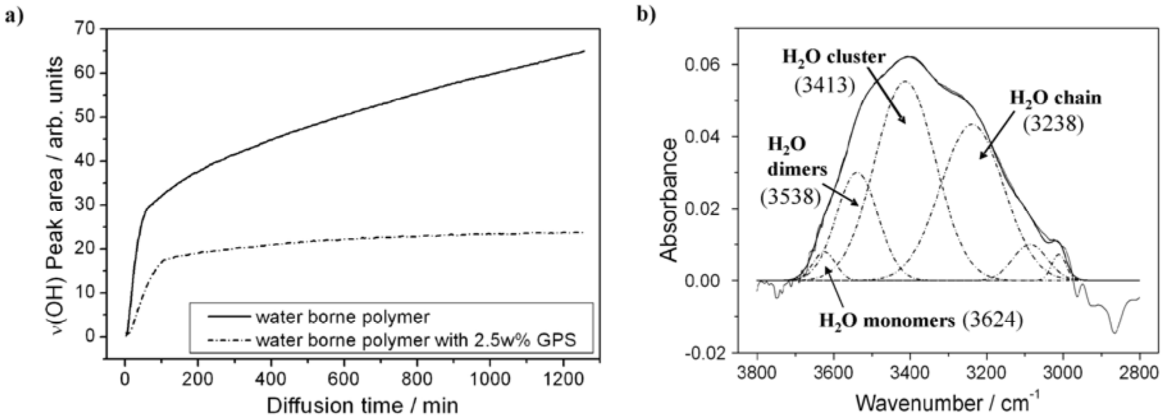

Water borne pol. with 2.5 wt% GPS			Water borne pol. with 5 wt% APS		
Wavenumber [cm^{-1}]	FWHM [cm^{-1}]	Peak areas related to peak at 3238 cm^{-1} [%]	Wavenumber [cm^{-1}]	FWHM [cm^{-1}]	Peak areas related to peak at 3211 cm^{-1} [%]
3624	69	6	3599	128	14
3538	128	46	3470	239	161
3413	186	122	3344	202	136
3238	194	100	3211	165	100

Fig. 5-3: a) Comparison of water uptake with addition of 2.5 wt% GPS. b) Fit of OH stretching peak of water borne polymer with 2.5 wt% GPS after 1000 min of immersion in borate buffer. The table gives FWHM values and peak areas of the OH peak fi presented in Fig. 5-3b and Fig. 5-6b.

The phase decreases uniformly in Fig. 5-2a between 10^4 Hz and 0.1 Hz [159,98,143]. The mentioned decrease stops after 110 min of immersion into electrolyte (Fig. 5-2c). Phase and impedance begin to re-increase slowly after 300 min. This effect was also observed with 0.5 wt% GPS, but it was not detected when the unmodified coating (Fig. 4-7) or the 5 wt% GPS-modified coating were investigated. At frequencies lower than 1 Hz the pore resistance R_{Po} of coating defects is detected. During water uptake the number of defects increases and the pore diameters grow. Therefore, a steady decrease of the pore resistance is expected as more water penetrates the polymer. The increasing pore resistance after 300 min could be interpreted as a partial stabilisation of the polymer/substrate interface which is caused by the presence of the adhesion promoter GPS. The coating structure strongly changes with increasing water amount, but the impedance data alone cannot clearly address the reason of the partial stabilisation [143].

The polymer/substrate interface is enforced due to addition of GPS. Coated Silicon ATR-crystals were exposed to borate buffer solution again and the increase of the interfacial water activity was observed by characteristic changes of the ν(OH) peak intensity. Fig. 5-3a shows the water uptake of a 2.5 wt% GPS containing water borne polymer. The increasing ν(OH) peak of unmodified water borne polymer is given as reference. Obviously, less water reaches the GPS modified polymer/silicon interface compared to the crystal coated with the unmodified water borne polymer. The slope of the initial steep increase of water activity during the first minutes of the experiment is lower for the GPS modified coating. It reaches a saturation level after about 100 minutes. Swelling in the substrate/polymer interphase is strongly diminished compared to the unmodified polymer [99].

For a more detailed interpretation of the H_2O peak shape the signal was fitted in the same way as explained for the unmodified water borne polymer in chapter 4.3.2 (Fig. 4-10) [16,17,52,53]. The result is displayed in Fig. 5-3b. It is comparable to the unmodified water borne polymer with the non H-bonded H_2O monomers at 3624 cm^{-1}, H-bonded dimers/clusters at 3538 cm^{-1} and 3413 cm^{-1}. Water molecules that specifically interact with the polymer network via H-bondeds are fitted at 3238 cm^{-1}. Signals at lower wavenumbers point at immobilised and strongly H-bonded H_2O molecules [16,53]. It can be concluded that the distribution of water species and agglomerates in the polymer matrix near the adhesive/substrate interface is hardly influenced by the presence of GPS. Similar as in the bare water borne polymer, the formation of a macroscopic interfacial water film is not observed [51,53]. The water amount in the polymer is reduced when GPS is added to the epoxy-amine mixture prior to the hardening process. The velocity of water diffusion through the bulk adhesive on the other hand is less affected.

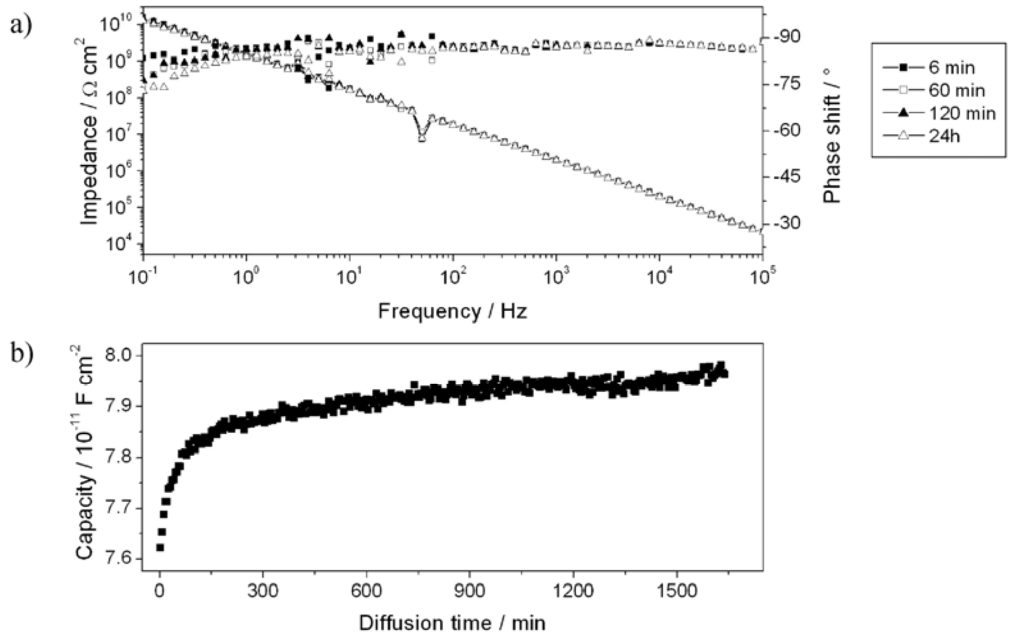

Fig. 5-4: Bode plot (a) and progression of capacity at 10 kHz (b) during water uptake in solvent borne polymer containing 2.5 wt% GPS

Water uptake was calculated from impedance data according to Brasher and Kingsbury and a value of 3 ± 1 % was determined. Such values were reported for solvent borne epoxy-amine polymers applied as adhesives or coatings [51,145]. The addition of GPS does not strongly change the diffusion properties of the solvent borne polymer compared to the water borne polymer. The introduction of hydrophobic silane groups reduced the water uptake of the water borne polymer to 8 %. The Bode plot of a 2.5 wt% containing solvent borne polymer is displayed as example in Fig. 5-4a. The change of capacity during immersion in borate buffer is displayed in Fig. 5-4b. Increase of capacity slows down after 150 min but a saturation level is not reached in the observed time range of 1700 min. Slow swelling can explain the small slope after fast water uptake. Furthermore, the velocity of the water diffusion into the polymer was also determined from the impedance data. The diffusion coefficient is determined as $1.5*10^{-9}$ cm^2/s.

Also the interface stability is not strongly modified by GPS addition. However, a small delay of the water uptake is detected in the polymer/silicon ATR crystal interphase when 2.5 wt% GPS are added to the solvent borne polymer (Fig. 5-5a). The same saturation value of the ν(OH) peak is reached after 200 min of immersion in borate buffer. Further, no swelling is observed in the GPS-modified solvent borne polymer due to low water uptake compared to the water borne polymer. But it also indicates high interface stability and good adhesion to the substrate. The peak shape of the ν(OH) peak in Fig. 5-5b was fitted with the same parameters as in Fig. 5-3 and Fig. 4-10. Peak positions of not-associated water molecules and H_2O dimers are shifted to higher wavenumbers in the 2.5 wt% GPS-containing solvent borne polymer. The contribution of low H-bonded water molecules or water dimers is slightly higher than in the unmodified polymer.

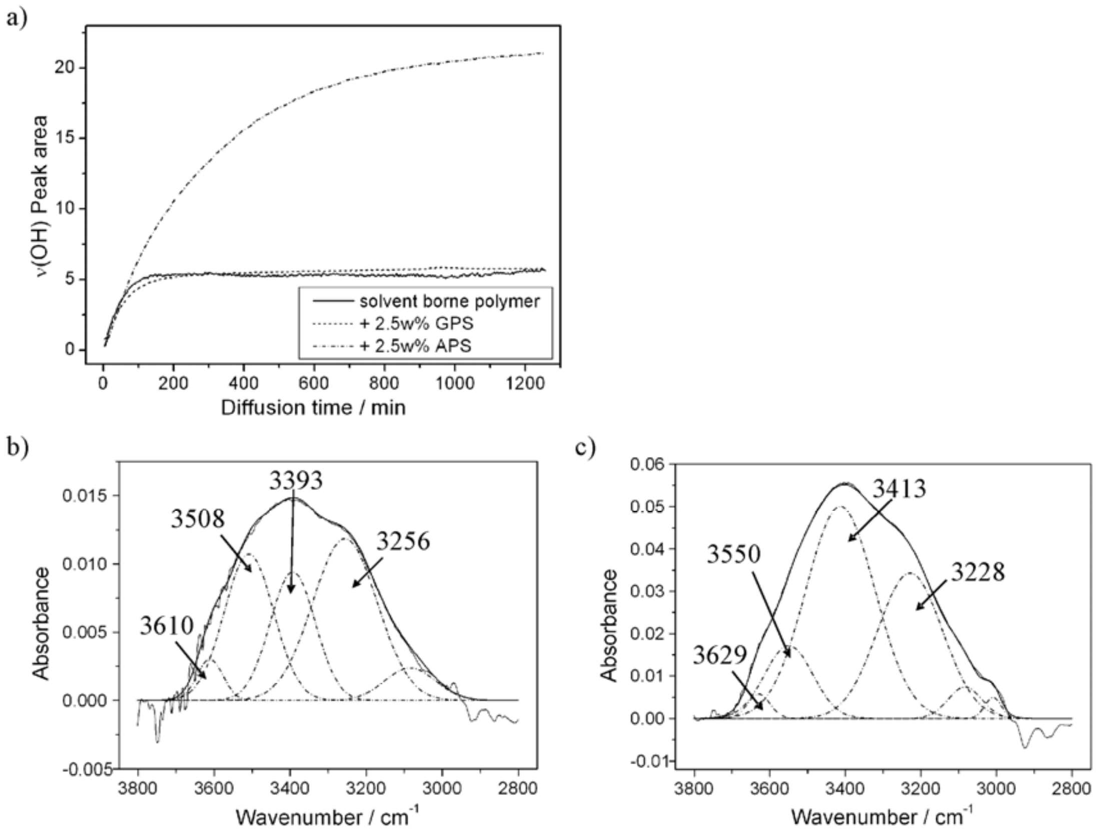

Solvent borne pol. with 2.5 wt% GPS (b)			Solvent borne pol. with 2.5 wt% APS (c)		
Wavenumber [cm^{-1}]	FWHM [cm^{-1}]	Peak areas related to peak at 3256 cm^{-1} [%]	Wavenumber [cm^{-1}]	FWHM [cm^{-1}]	Peak areas related to peak at 3228 cm^{-1} [%]
3610	81	10	3629	70	6
3508	153	69	3550	149	37
3393	140	56	3413	216	156
3256	200	100	3228	202	100

Fig. 5-5: a) Water uptake from borate buffer in modified solvent borne polymer measured by ATR-IR spectroscopy. b) ν(OH) peak of solvent borne polymer with 2.5 wt% GPS after 1000 min of immersion in borate buffer. c)) ν(OH) peak of solvent borne polymer with 2.5 wt% APS after 1000 min of immersion in borate buffer.The table gives FWHM values and peak areas of the OH peak fit.

In general, GPS seems to stabilise the polymer/substrate interface due to the reduced water uptake of the water borne polymer. Fitting the ν(OH) peak after 1000 min gives the association of water in the polymer/silicon ATR crystal interphase. It is independent on the addition of GPS and depends only on the applied polymer.

5.1.2 Application of APS as adhesion promoter

Wapner and Grundmeier found that mixing APS to the coating improves polymer adhesion if the sample is stored for several days after coating application [160]. They assumed that during storage the organosilane diffuses to the substrate surface, where it is consumed by chemical reaction with the iron oxide. Abel and Watts [86] also show diffusion of APS from the polymer bulk to the aluminum surface after half a day of curing at room conditions. XPS and

ToF-SIMS experiments of APS accumulation at the steel surface from a polyamide coating had shown similar results [161]. Abel and Watts further show that the plane of failure changes due to APS addition. They conclude that the interaction of APS and iron is high, but not the interaction between the APS layer and the polymer. The polymer/APS/iron interphase will be further analysed in the following chapter.

Adhesion promotion was not clearly observed when 0.5 wt%, 2.5 wt% or 5 wt% APS were added to the water borne polymer. EIS and ATR-IR measurements show that more water accumulates in the interphase of the water borne polymer and the silicon ATR crystal. As an example progression of water accumulation at the ATR crystal/polymer interphase is given in Fig. 5-6a, which was detected by ATR-IR spectroscopy. The initial behaviour resembles that of the unmodified water borne polymer. However, lateron swelling of the modified water borne polymer is much stronger. The effect on adhesion is discussed in detail in chapter 5.2. Impedance data does not indicate higher water uptake in the polymer bulk. APS as an additive was not observed to clearly enhance adhesion of the water borne polymer at similar exposition times. The shape of ν(OH) peak is displayed in Fig. 5-6b. Fitting was performed with the same parameters used for GPS-modified polymer in Fig. 5-3b and unmodified polymer in Fig. 4-10a. The peak shape of APS containing water borne polymer is very different from the unmodified and the GPS-modified polymer after water uptake. H-bonded amine groups (NH stretch) contribute to the OH stretching between 3300 cm^{-1} and 3400 cm^{-1} on the one hand and thereby specific binding of OH changes on the other hand. The largest peak shifts from 3416 cm^{-1} in unmodified water borne polymer to 3470 cm^{-1} in 5 wt% APS containing polymer.

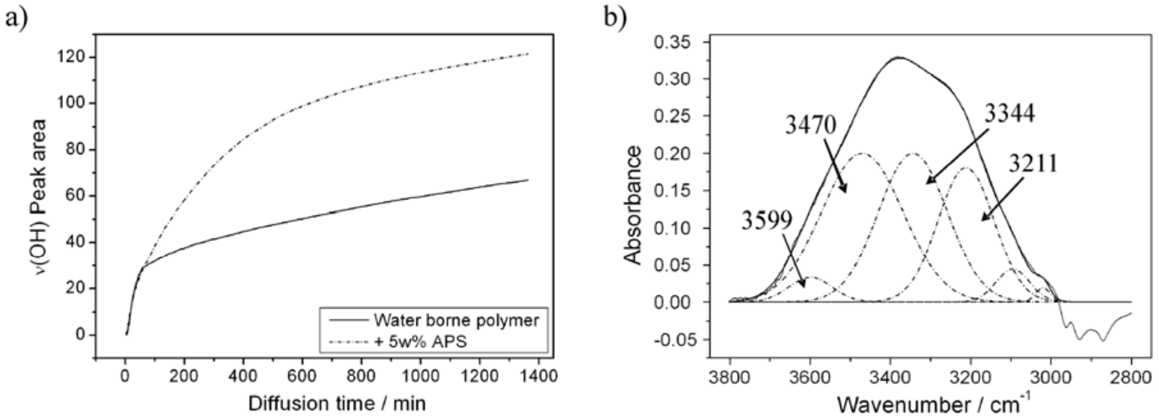

Fig. 5-6: Water uptake from borate buffer in water borne polymer with 5 wt% APS (a). b) ν(OH) peak after 1000 min of immersion in borate buffer. The fit parameters are given in the table in Fig. 5-3.

Similar results are gained for addition of 0.5 wt%, 2.5 wt% and 5 wt% APS in the solvent borne polymer. The bulk water uptake does not change but the interphase shows a higher water activity after saturation. Fig. 5-5a shows the increasing ν(OH) peak area of the 2.5 wt% APS containing solvent borne polymer after immersion in borate buffer. It resembles the water uptake of the water borne polymer. Therefore, swelling of the polymer in the interphase can be interpreted. Similar to the effect of APS in the water borne polymer also in the solvent borne polymer the composition of water species absolutely changes as displayed in Fig. 5-5c. H_2O monomers are measured at higher wavenumbers (3629 cm^{-1}) than before and the FWHM values increase. The ν(OH) band resembles water borne polymer in this case which means that more voids exist and specific interactions increased due to the area of 156% at 3413 cm^{-1}.

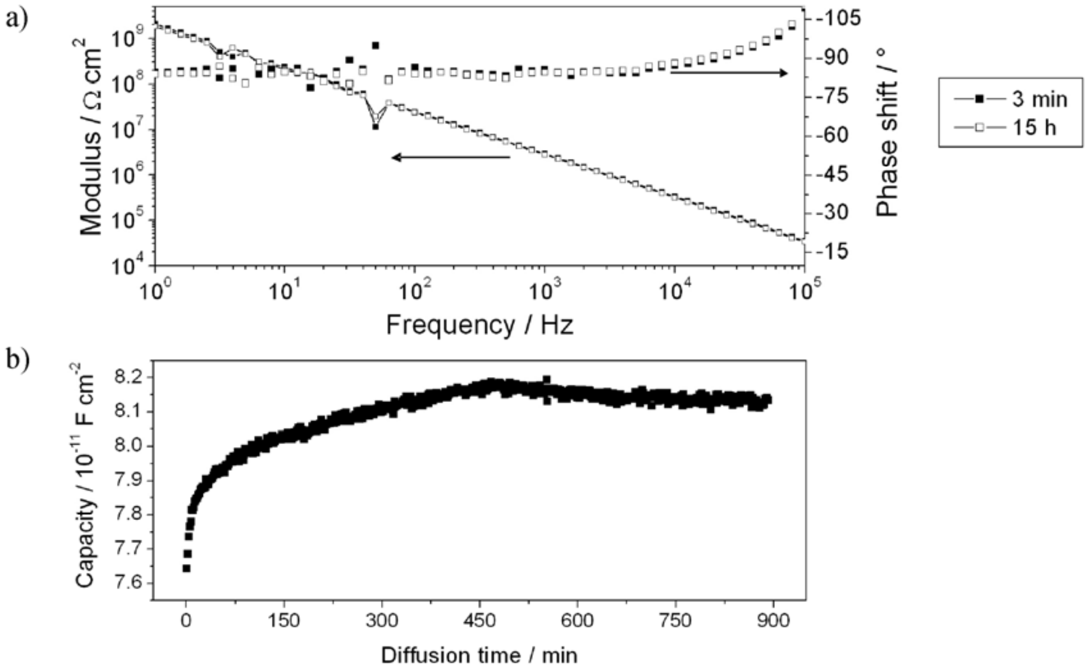

Fig. 5-7: Impedance measurement of solvent borne polymer with 2.5 wt% APS during immersion in borate buffer. a) Bode plot. b) Capacity determined at 10 kHz.

Impedance measurements of APS modified solvent borne polymer do not show degradation of the polymer after immersion in borate buffer (Fig. 5-7a). Even water uptake is not significantly enhanced and is still at approximately 1 %. Only the diffusion coefficient seems to be slightly higher, $3.5*10^{-9}$ instead of $1.5*10^{-9}$ cm^2/s. The capacitance curve during water uptake of solvent borne polymer with 2.5 wt% APS in Fig. 5-7b shows again reorganisation [24]. Hinderliter reports this asymmetry for wetting and drying cycles and assigned them to redistribution of water within the coating and homogenisation.

5.2 Polymer/substrate interface and adhesion

Peel tests are again applied to characterise the interface structure and behaviour after exposition to high humidity and during drying. The experiment was performed as displayed in Fig. 4-12: SEM/EDX analysis and XPS surface analysis were performed after the peel test. Results of GPS and APS containing water and solvent borne polymer systems are displayed in Fig. 5-8. The displayed peel tests were performed after exposition of the samples to high humidity for 5 days or for 20 days. The exposure time indicates that interface stabilities of the systems under study strongly differ. Systems with higher GPS or APS content are not displayed, because their polymer/steel interfaces were very stable and a peel test could not be performed. In some cases only small steel surface areas were layed open in order to perform XPS and SEM analysis. The peel test was performed while drying of the polymer at room conditions. The last measurement indicates the point of cohesive failure of the polymer layer.

It is interesting that the cohesive properties of the different systems vary during esposure [105]. In case of strong adhesion of the water borne polymer only small polymer pieces were peeled from a brittle polymer layer. Interface destabilisation of the solvent borne polymer was observed after 20 days. After this exposure period the solvent borne polymer was still flexible and the peel tests could be performed. The maximum measured peel force indicates the cohesive strength of the polymer layer which are clearly lower for the APS containing water borne polymer.

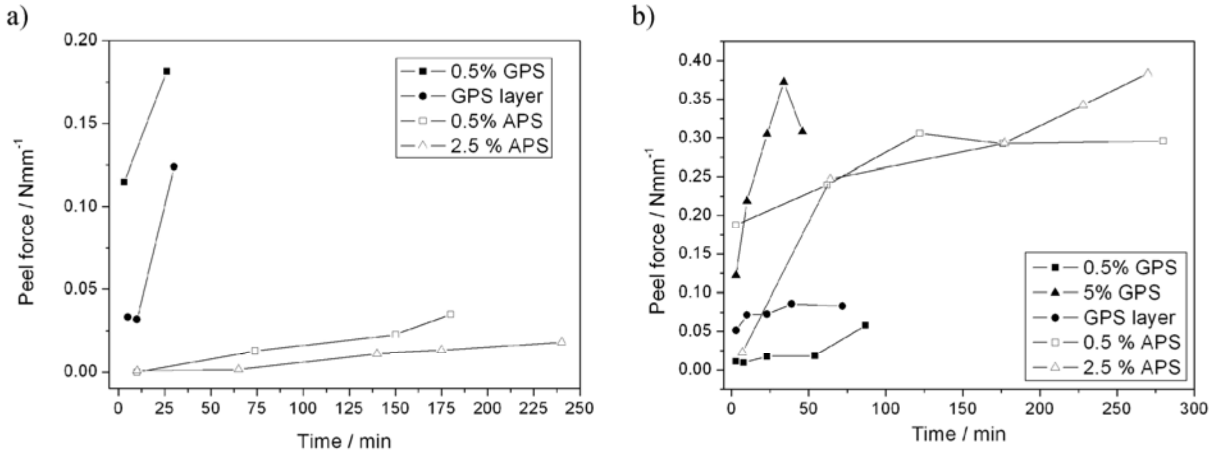

Fig. 5-8: Peel test of water borne polymer on steel substrate with GPS and APS after 4 days of exposure to high humidity (>96% r.h.) (a). Peel test of solvent borne polymer on steel substrate with GPS after 20 days of exposure and with APS after 5 days of exposure (b).

Furthermore, the presented peel tests display re-bonding as a function of the added organosilane and the organosilane content. This can be compared to the bare polymers in Fig. 4-13. Re-bonding is important for a good corrosion protection, which is tested or compared with wet-dry cycles [153]. The water uptake reaches a maximum after two hours for the water and the solvent borne polymer (Fig. 5-5 and Fig. 5-6). The peel tests were performed after several days of exposure to humidity to assure a weakened interphase structure by complete water uptake. Re-bonding as well as adhesion strength of the water borne polymer are improved by addition of GPS. APS does not have a positive effect on adhesion performance. The solvent borne polymer shows that in case of loss of adhesion, the peel force is similar for APS and GPS. With GPS a loss of adhesion happens after a longer exposure period and re-bonding is much faster.

5.2.1 Application of GPS as adhesion promoter

Bonding of the water borne polymer is enhanced by addition of GPS to the coating or by application of a GPS primer on the steel substrate. Following SEM and EDX measurements are displayed in Fig. 5-9a. They show an almost bare steel surface. Some organic residues containing silicon are detected by EDX.

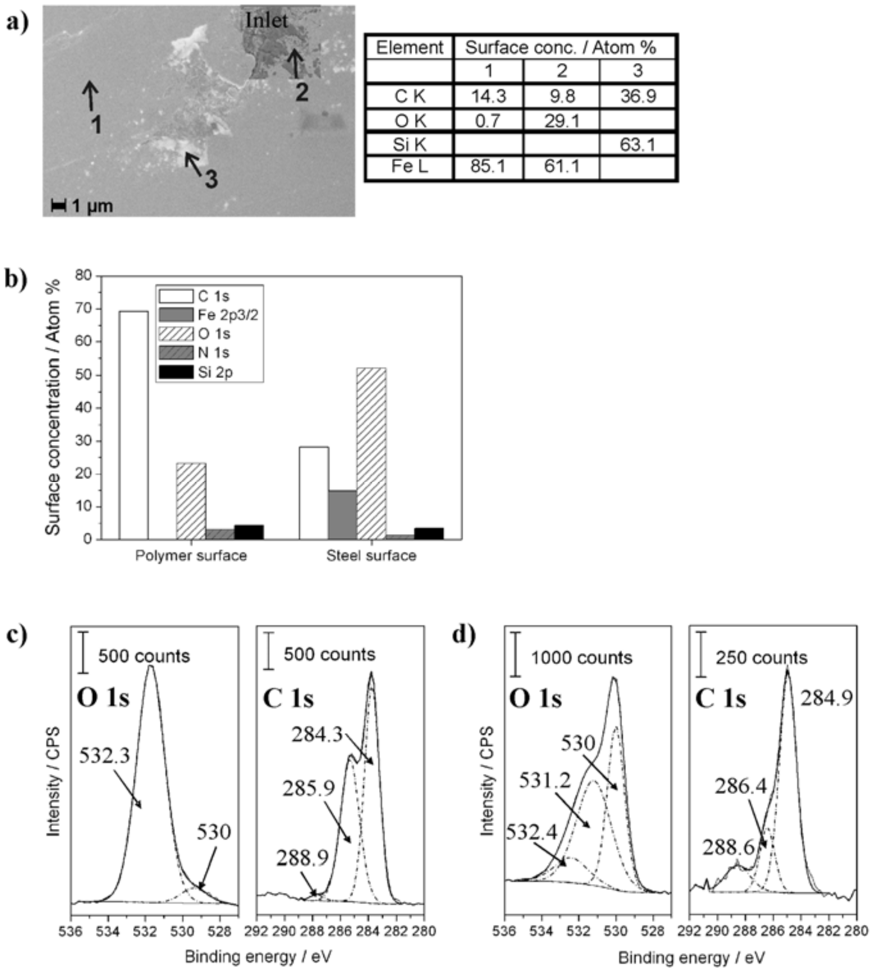

Element	Surface conc. / Atom %		
	1	2	3
C K	14.3	9.8	36.9
O K	0.7	29.1	
Si K			63.1
Fe L	85.1	61.1	

Fig. 5-9: Surface analysis of water borne polymer with 2.5 wt% GPS after peeling from steel substrate. a) SEM and EDX results. SEM parameters: Mag=15kX, WD=10 mm, EHT=5 kV, Detector: Inlens, Inlet – MPSE. b) Surface composition determined by XPS. c) O 1s and C 1s high resolution spectra of polymer surface and d) of steel surface after peeling the polymer.

Surface analysis performed by means of XPS of the water borne polymer containing 2.5 wt% GPS is displayed in Fig. 5-9b, Fig. 5-9c and Fig. 5-9d. Surface concentrations of carbon, iron, oxygen, nitrogen and silicon on the steel surface are compared to the polymer surface after the peel test. The analysis of both sides of the polymer/steel interface reveals the plain of failure. Silicon is detected on both surfaces as well as nitrogen. C 1s and O 1s high resolution spectra should indicate the amount of polymer residues on the substrate. Aromatic polymer components at 284.3 eV on the polymer surface are not detected on the steel substrate which points at a failure of the adhesive bonds of the water borne polymer to the steel surface. Furthermore, iron is not detected on the polymer surface for the same reason. A large amount of C=O is detected at 532.3 eV on the polymer. The C 1s peak of the steel surface is composed of C-C/C-H at 284.9 eV, some C-O at 286.4 eV and more CO_3^{2-} than on the polymer. The O 1s peak of the steel surface shows the composition of iron oxide at 530 eV, hydroxide at 531.2 eV and C=O or CO_3^{2-} and H_2O at 532.4 eV. These results indicate that the plain of failure is in the organosilane layer and includes some minor polymer residues.

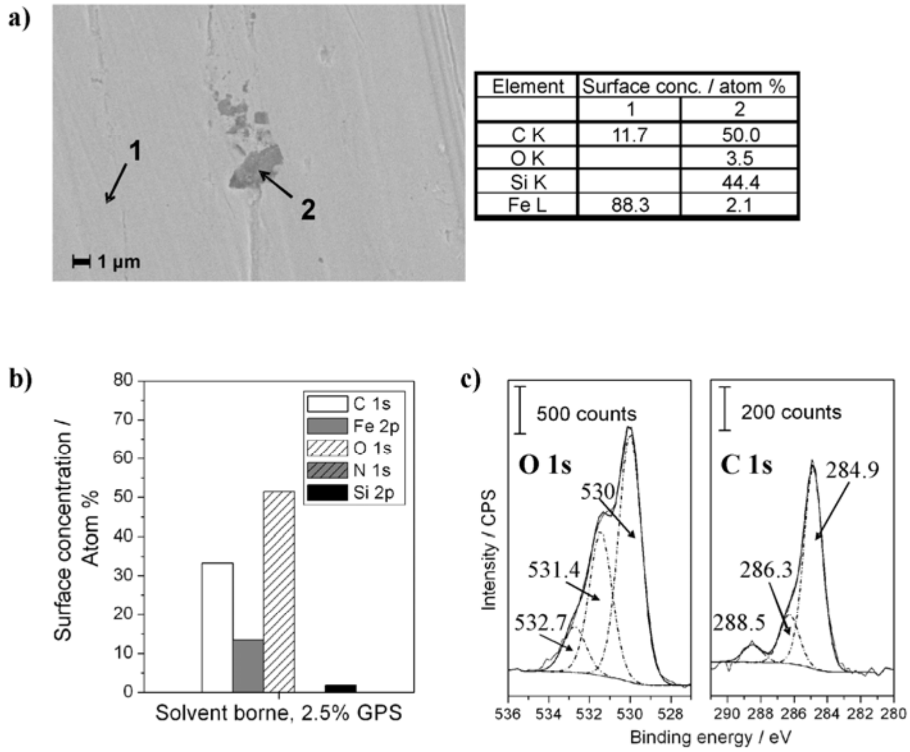

Element	Surface conc. / atom %	
	1	2
C K	11.7	50.0
O K		3.5
Si K		44.4
Fe L	88.3	2.1

Fig. 5-10: Surface analysis after peel test of solvent borne polymer with 2.5 wt% GPS. a) SEM and EDX analysis on spots 1 and 2. SEM parameters: Mag=15kX; WD=9mm; Detector=SE2; EHT=97kV. b) Surface concentration of elements detected by XPS on the steel surface and. c) O 1s and C 1s high resolution spectra.

In case of the solvent borne polymer containing 0.5 wt%, 2.5 wt% and 5 wt% GPS, only small residues are detected after the peel test. As example, the sample with 2.5 wt% GPS is displayed in Fig. 5-10. SEM pictures show small dark features up to 2 µm in diameter. These islands include high carbon and silicon amounts (Fig. 5-10a). The rest of the surface seems to be uncovered after removing the polymer. Only small amounts of carbon are detected. Also the XPS surface analysis displayed in Fig. 5-10b and Fig. 5-10c shows organic residues including silicon, but high resolution spectra do not show aromatic carbon from the solvent borne polymer (Fig. 4-14f). The plain of failure is between polymer and steel surface.

The high resolution spectra of water and solvent borne polymer are very similar, indicating that almost no organics are left on the substrate. Only small parts of the polymer were removed in this case, because a full peeling after exposure in high humidity was not successful. However, nitrogen was not detected in the solvent borne polymer sample but on the water borne polymer sample.

5.2.2 Application of APS as adhesion promoter

Fig. 5-11 shows SEM surface analysis of 0.5 wt%, 2.5 wt% and 5 wt% APS containing water borne polymer. When an APS layer is adsorbed on the substrate prior to organic film application, peel tests could not be performed because of strong bonding of the coating to the substrate surface. Already an addition of 0.5 wt% APS leads to island formation on the substrate surface. Single spots analysed by EDX consists of iron and oxygen, but the also carbon, nitrogen and silicon are detected in the islands. Therefore, adhesion is not improved. With addition of more APS, islands grow larger and the particle number on the surface increases. Generally, grey areas in the SEM pictures are polymer free areas and black areas are remains of polymer, some of them containing silicon.

SEM pictures and EDX analysis presented in Fig. 5-11 were measured after 10 min of drying and after three hours, on the time scale of the peel test in Fig. 5-8. The 0.5 wt% APS containing water borne polymer shows some residues after 10 min drying. Generally, more islands are detected on the surface after 10 min of drying. Islands with a diameter of about 0.4 µm are present at the steel substrate after peeling off the water borne polymer containing 2.5 wt% APS (Fig. 5-11d). Black, organic residues are detected at short drying and APS islands are detected after 3 hours drying. At the interface of water borne coating containing 5 wt% APS islands are larger. Between the islands silicon and carbon are not detected on the steel surface. Already in wet state large islands are detected on the substrate. It is unclear whether these islands are formed because of high APS concentration at the interface or if they are formed due to phase separation throughout the bulk polymer.

Bulk cross sections of water borne polymer are prepared by FIB. Also in the bulk APS islands form during film formation. Fig. 5-12 displays the cross sections of 2.5 wt% GPS and 5 wt% APS containing water borne polymer. GPS does not show any features and is homogenously dispersed in the polymer.

XPS surface analysis gives more information about the chemical composition of the organic residues detected by SEM/EDX. In order to understand the composition of the substrate/ coating interface not only the steel surface but also the composition of the buried coating surface is analysed. Though XPS is more surface sensitive, the average value of the measurement area of 50 x 50 µm^2 causes a different elemental surface distribution in XPS compared to EDX results. SEM images of the island-like structures with 0.4 µm to 1 µm in diameter displayed in Fig. 5-11 cannot be analysed explicitly by means of XPS.

High water activities were determined by ATR-IR spectroscopy when APS was present at the polymer/substrate interface. This may lead to destabilisation of the polymer and failure through the three-dimensional network. The plain of failure is analysed as function of the water activity with increasing drying times according to the experiment displayed in Fig. 4-12. SEM results of the water borne polymer with 2.5 wt% APS observed at increasing drying time are displayed in Fig. 5-11 and XPS results in Fig. 5-13.

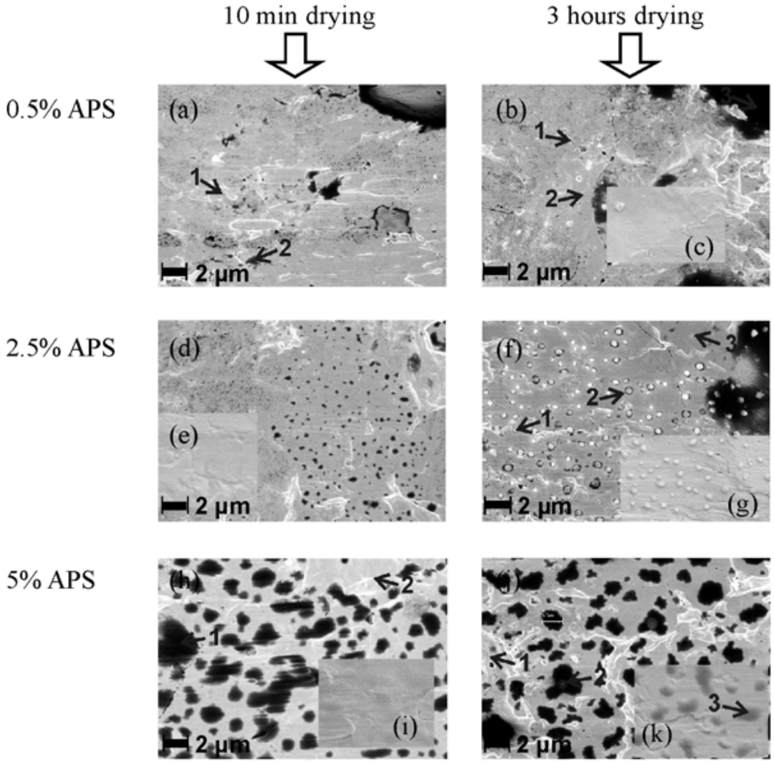

EDX results

Element	Surface concentration / Atom %												
	a) 1	a) 2	b) 1	b) 2	b) 3	f) 1	f) 2	f) 3	h) 1	h) 2	j) 1	j) 2	k) 3
C K		47		5.2	24.1	53.9	24.4		15.7			41.5	34.3
N K		9.2					4.7						7.6
O K		11.7	5.8	7.5	13.8	23.9	19.4	1.2	9.2	4.3	4.5	21.7	23.1
Si K					11.9	22.2	17.9		5.5			22.1	21.3
Fe L	100	32.1	94.2	87.3	50.2		33.5	98.8	69.6	95.8	95.5	14.7	13.8

Fig. 5-11: SEM analysis of steel surface after peeling water borne polymer with 0.5 wt%, 2.5 wt% and 5 wt% APS after 10 min and 3 hours of drying at room conditions. EDX results are displayed for pictures (a) to (k). SEM parameters: Mag=15kX, WD=9 mm, EHT=5 kV, Detector: Inlens, Inlet (c), (g), (i), (k) with SE2.

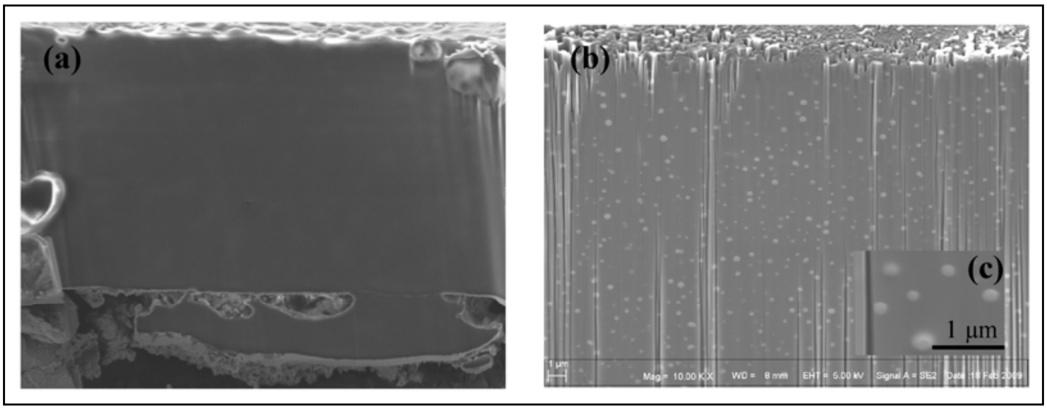

Fig. 5-12: Bulk analysis of water borne polymer with 2.5 wt% GPS (a) and 5 wt% APS (b). Surfaces were prepared by focused ion beam (FIB) and analysed by SEM. SEM parameters: a) Mag = 5 kX, WD = 8 mm, Detector= SE2, EHT = 5 kV, b) Mag = 10 kX and c) Mag = 40 kX.

The silicon content on the steel surface decreases during drying even though SEM images show uniform distribution of silicon-rich islands on the substrate. At the same time the amount of detected iron and carbon slightly increase. The surface concentrations of carbon and nitrogen describe the amount of polymeric remains on the steel surface. Iron and oxygen surface concentrations indicate coverage and film thickness on the steel substrate. As a result, the relative amount of carbon and iron indicate the plain of failure during the peel test. C 1s and O 1s high resolution spectra of the steel surface are fitted and displayed in Fig. 5-13b. They present the variation of surface composition between 10 min and 3 hours of drying before the peel test was performed. The iron oxide component at 530 eV in the O 1s spectra is used as reference. The ratio of the Fe_2O_3 peak and the C-O/OH peak at 531.4 eV obviously changes. Less OH is detected due to evaporation of water on the one hand. On the other hand this result again indicates that the plane of failure changes. Due to increasing intensity of iron oxide, the plain of failure approaches the steel surface. In the C 1s high resolution spectrum the amount of aromatic C-C at 284.3 eV which comes from the polymer, decreases after drying. At the same time the C-C component at 285.1 eV and the C-O component at 286.5 eV slightly increase. Generally, the XPS measurement shows that in the wet state of the polymer, the failure during the peel test occurs in the polymer layer next to the steel surface. With drying of the polymer the failure approaches the steel surface. On the coating surface the amount of silicon (Si 2p) as well as the detected amount of nitrogen (N 1s) decrease after drying of the interface.

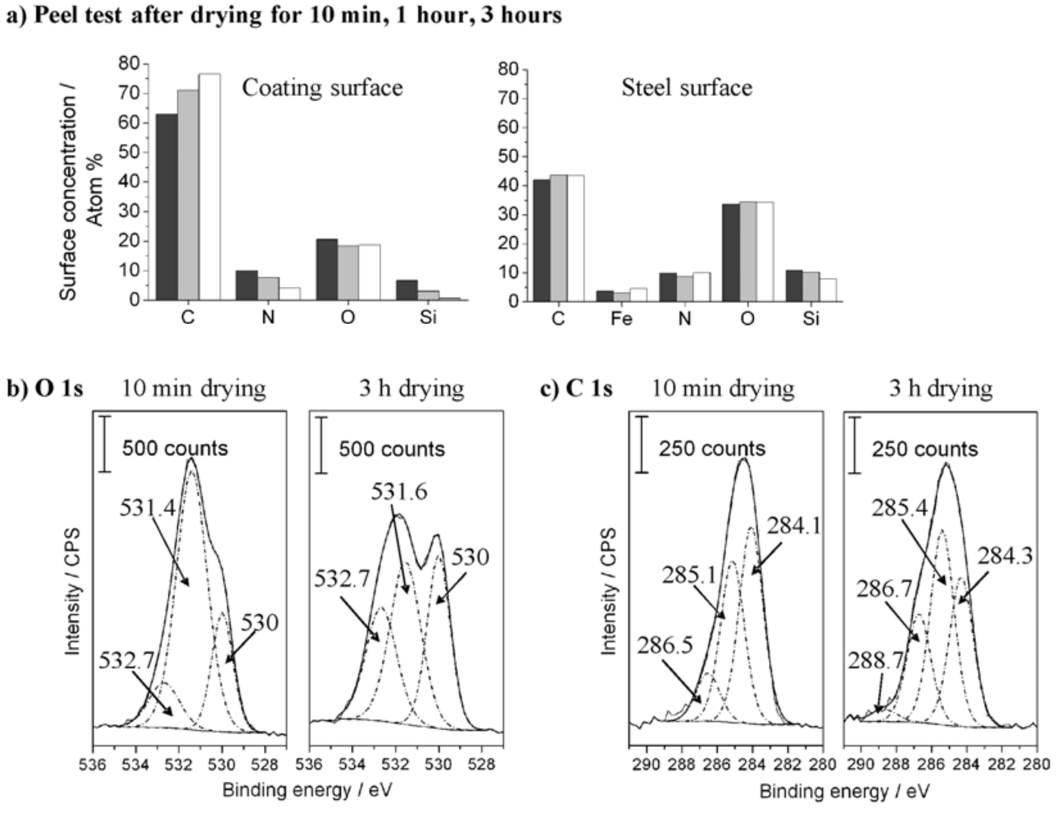

Fig. 5-13: XPS surface analysis of steel and coating surfaces after peeling water borne polymer. a) Interphase composition of 2.5 wt% APS containing water borne polymer after 10 min, 1 hour and 3 hours of drying before the peel test was performed. b) O 1s and C 1s high resolution spectra, comparison between 10 min and 3 hours of drying before peel test of 2.5 wt% APS containing water borne polymer.

A comparison of the results for 0.5 wt% and 2.5 wt% APS in water borne coating shows an increase of the detected amount of silicon with increasing APS concentration. At short drying times more organic residues are detected at higher APS concentrations (Fig. 5-14a). After drying, the APS concentration detected by XPS is similar in all interphases although SEM images show diverse steel surfaces. In SEM images the island coverage is correlated to the APS concentration in the coating. Less iron is present on the surface than with addition of 0.5 wt% APS which indicates that the organic layer remaining on the surface is thicker. At 3 hours drying, the film thickness of the polymeric residues seems to be similar on the different samples (0.5, 2.5 and 5 wt% APS in water borne polymer in Fig. 5-14b). This result indicates that the plane of failure is moving towards the steel surface during the peel test with increasing drying time. When the coating is wet, the cohesive strength of the polymer is weaker because of high water concentrations. During the drying process, stability of the polymer increases and the cohesive strength is larger than bonding to the steel surface. Another interpretation of the growing silicon concentration in XPS results can be the increasing bonding of APS to the steel surface during drying.

a) Surface composition after 10 min drying

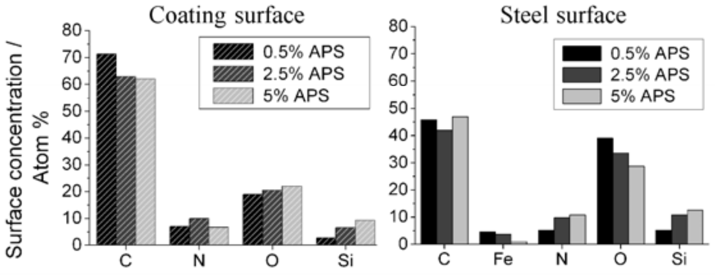

b) Surface composition after 3h drying

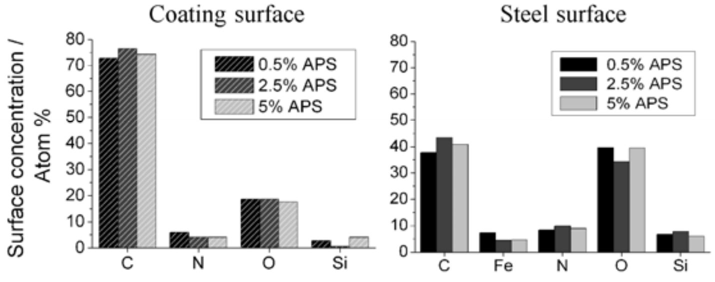

Fig. 5-14: Interphase composition of water borne polymer with 0.5 wt%, 2.5 wt% and 5 wt% APS on steel determined by XPS. a) Polymer and steel surface composition with 10 min and b) 3 hours drying period before peel test.

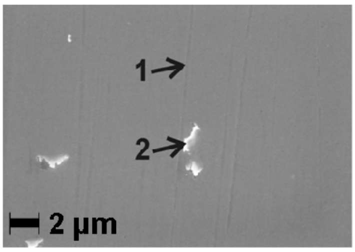

Element	Surface conc. / Atom %	
	1	2
C K	4.2	6.1
N K		
O K	3.2	7.5
Si K		
Fe L	92.6	86.5

Fig. 5-15: SEM analysis of 2.5 wt% APS containing solvent borne polymer after three hours drying time before peeling and EDX analysis of spots 1 and 2. SEM parameters: Mag = 15 kX, WD = 9 mm, EHT = 5 kV, Detector = Inlens.

SEM and EDX results of the solvent borne coating containing 2.5 wt% APS are displayed in Fig. 5-15. Small features with small amounts of carbon are detected, but silicon is not detected by EDX. Silicon was also not detected at higher APS concentration. This means that the EDX penetration is too high for detecting the nm-thin silicon layer. APS and the solvent borne polymer establish an intact coating, because no APS agglomerates are found at the interface after peel test in the dry state of the coating. Measurement of the solvent borne coating on an APS layer was not possible due to high adhesive forces.

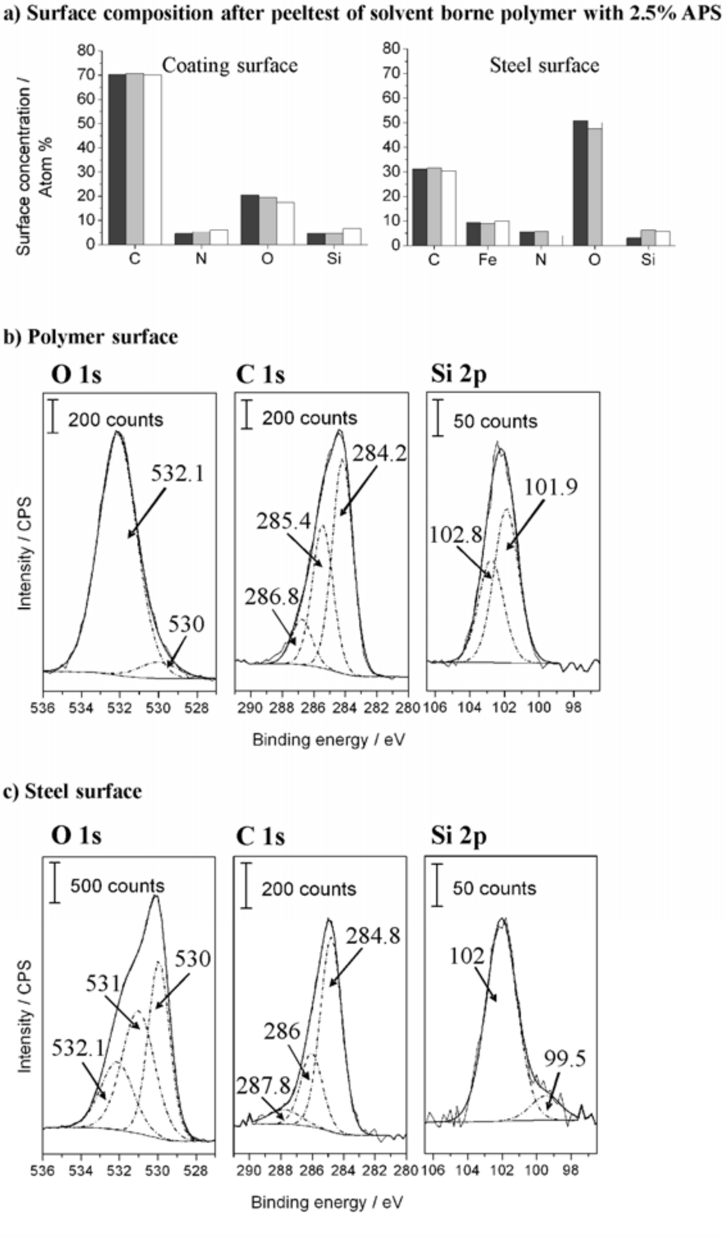

Fig. 5-16: Surface analysis after peeling solvent borne coating with 2.5 wt% APS. a) Surface concentration of elements detected by XPS on coating and steel surface after peel test at drying times of 10 min, 1 hour and 3 hours. b) High resolution spectra of polymer surface peeled after 1 hour of drying. c) High resolution spectra of steel surface peeled after 1 hour of drying.

XPS surface analysis of solvent borne polymer containing APS is displayed in Fig. 5-16 and Fig. 5-17. The surface composition of solvent borne polymer with 2.5 wt% APS is given in Fig. 5-16. With increased drying time silicon concentration on steel and polymer surface slightly increase (Fig. 5-16a) while nitrogen concentration diminishes on the steel surface. No changes of the components are observed in high resolution spectra of C 1s, O 1s and Si 2p. Fig. 5-16b and Fig. 5-16c display the surface composition of the polymer and steel surface. C 1s and O 1s of the steel surface resemble the spectra shown before in Fig. 5-9d and Fig. 5-10c. The polymer C 1s and O 1s spectra can be compared to the bare solvent borne polymer in Fig. 4-14. But the oxygen peak results at 532.1 eV instead of 531.6 eV on the unmodified solvent borne polymer. The Si 2p peak depends on the surface. It is Si^{+II} at 102 eV on the steel surface and a second component is detected at higher oxidation states at 102.8 eV in the polymer. N 1s is on both steel and polymer surface composed of unprotonated and protonated component.

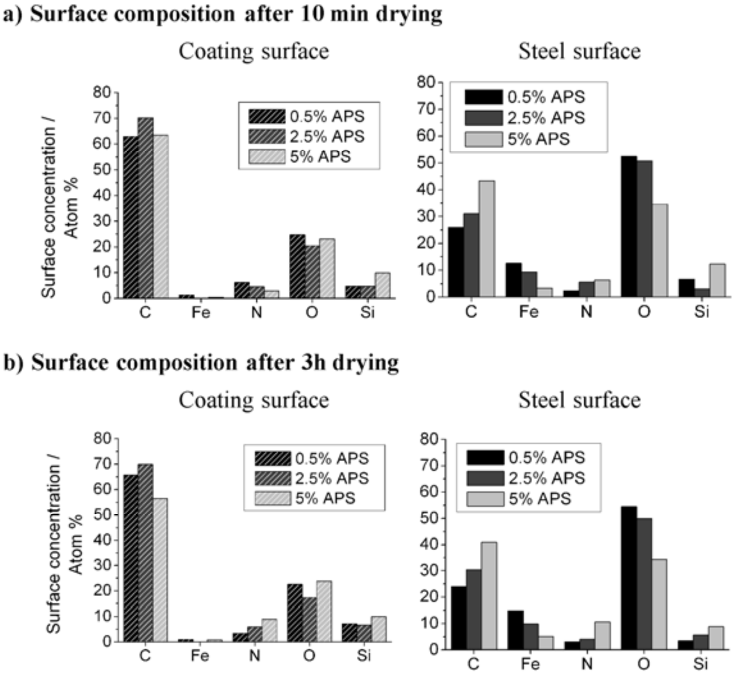

Fig. 5-17: Interphase composition of solvent borne polymer with 0.5 wt%, 2.5 wt% and 5 wt% APS on steel determined by XPS. a) Polymer and steel surface composition with 10 min and b) 3 hours drying period before peel test.

Fig. 5-17 shows that more silicon is detected on polymer and steel surface with higher APS concentration in the solvent borne polymer. A small amount of iron on the coating surface indicates that the plain of failure in peel test is next to the steel surface. Comparison of XPS results after three hours of drying show that detection of iron on the substrate surface decreases with increasing APS concentration. This indicates an increase in thickness of the adsorbed APS layer in the nanometer-range and polymer failure in the APS layer, but not in the polymer.

5.3 Conclusions

Organosilane adhesion promoters were applied in order to improve the interface stability of the water borne and the solvent borne epoxy-amine polymers. Addition of GPS to the polymer leads to the desired properties as shown by peel tests: the interface is more stable at immersion in electrolyte or exposure to high relative humidity and re-bonding during drying is observed for both the water and the solvent borne polymers. After peeling off the polymer a low amount of organic residues is detected at the water borne polymer/steel interface as well as for the solvent borne system. The failure is observed in the interphase adjacent to the steel surface.

At the same time, GPS has a positive effect on the bulk stability of the water borne epoxy-amine polymer. This effect further improves the interface stability by a reduction of the total water uptake. However, the peel forces of the wet water borne polymer films are smaller than for the solvent borne films even after addition of GPS. The reason is a significantly smaller water uptake in the solvent borne coating.

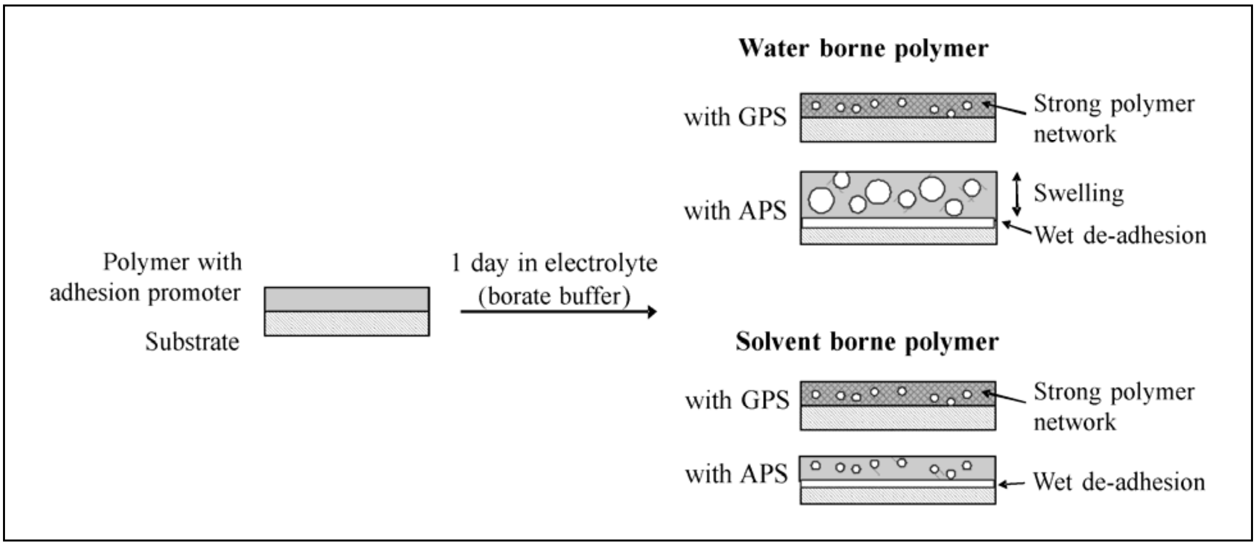

Fig. 5-18: Schematic: behaviour of the water borne and the solvent borne polymers with GPS or APS as adhesion promoters

In contrast to the effect of GPS addition, APS weakens the cohesive strength of the three-dimensional polymer network. Therefore, no peel test correlated to drying could be performed for polymer films containing 5 wt% APS due to cohesive failure of the polymer. In addition, peel tests show that APS as an additive does not improve adhesion for both the water borne and the solvent borne polymer films.

High APS concentration in the polymer/substrate interphase can cause a defective interphase structure due to a high amine concentration. As a result, the interface stability is lower than the bulk stability because of reduced crosslinking. A part of the functional groups reacts with the substrate surface. Thereby, more epoxy groups than amine groups are consumed. The reaction of epoxy groups is reduced with the addition of amine containing organosilanes. However, the amine concentration is further increased which results again in a high amine/epoxy ratio. Furthermore, silicon containing island-like particles are detected on the substrate after peeling off water borne coating and in the bulk polymer by means of SEM and EDX. This indicates a phase separation between APS and the water borne polymer. Such features are not found at the solvent borne coating/substrate interface. Consequently, a higher water uptake in the polymer bulk and in the interphase was detected for addition of 5 wt% APS. It leads to wet delamination even though an APS layer is present at the interface.

6 Kelvin probe studies of interfacial wet de-adhesion and corrosion [1]

A transport of hydrated ions along a polymer/oxide/metal interface is observed in humid air when a coating defect is covered by an electrolyte. The process of cathodic delamination is dominant on iron, steel and zinc substrates in such an environment [105,106,162-165]. A galvanic cell is generated with an increased metal dissolution at the local anode in the defect area and a reduction of oxygen molecules at the local cathode within the delaminated zone. Hydroxide species generated by oxygen reduction increase the pH of the interface and require a transport of cations from the defect electrolyte to the front of delamination for reasons of charge compensation [105,106,162-165]. The height regulated Scanning Kelvin Probe has been established as a method for non-destructive measurements of electrode potentials to monitor the ion transport [93,166-169]. Sigmoid SKP profiles are typically recorded and the turning point of the potential versus distance graph is assigned to the electrolyte front position [93,105,106,162-169]. It reflects the transition between intact interface sections and sample areas already deteriorated by cathodic delamination. In general it is expected that the ingress of defect electrolyte at the polymer/substrate interface causes a downshift of the electrode potential [105,106,162-165]. Nazarov et al. reported that a characteristic adjustment of the interface potential is also observed when water diffusion through the polymer bulk occurs and when this water reaches the polymer/substrate interface [170]. The detected potential shift was attributed to a correlated change of the interface dipole moment [170,171].

Epoxy-amine coated steel substrates were investigated by in-situ SKP experiments and ex-situ XPS measurements. Unusual potential profiles were recorded with the SKP for the water borne polymer during cathodic delamination processes at the interface, while common potential profiles were detected for the solvent borne polymer. These results seem to be connected to an increased interfacial water activity at the water borne polymer/steel substrate interface. An exact identification of the front position of cathodic delamination is difficult in this case and the interfacial ion transport mechanism differs from that usually reported for polymer coated iron and steel samples. Adhesion promoters as APS and GPS were shown to strongly influence water uptake and adhesion in high humidity. APS did thereby not show strong stabilisation. But stabilisation of the interface in corrosive environment by addition of GPS is expected.

---

[1] The content of this chapter is partially adopted from publications [159] and [169].

6.1 Cathodic delamination at the water and solvent borne epoxy-amine/steel interfaces

6.1.1 Cathodic delamination on iron-zinc samples

First measurements of the epoxy-amine polymers were performed on combined iron and zinc surfaces. A part of a zinc covered steel sample is submerged in hydrochloric acid in order to lay open the iron surface (Fig. 6-1b). Fig. 6-1a displays an SKP measurement on the iron/zinc sample covered with solvent borne polymer after short exposure to >96% relative humidity. The potentials detected on zinc are about 300 mV lower than on iron because oxygen reduction is inhibited on zinc. After three days of reaction time a part of the solvent borne polymer coated iron surface is corroded.

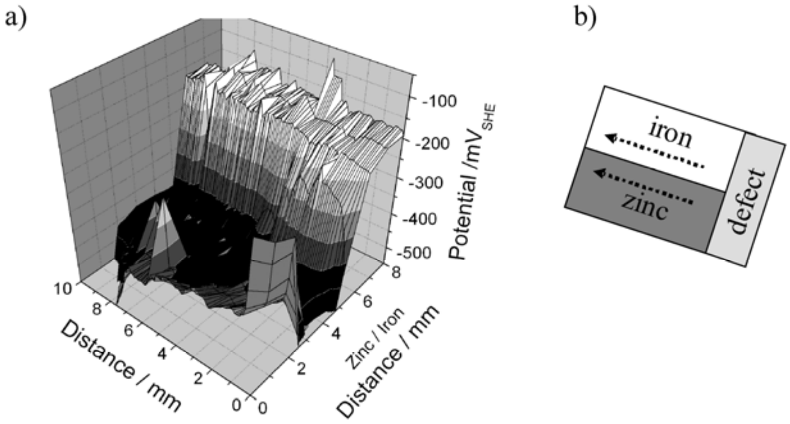

Fig. 6-1: SKP measurements of solvent borne polymer on iron/zinc substrates. a) Measurement after short exposure to high humidity (>96% r.h.). b) Sample setup used in (a).

The same experiment was performed with the water borne polymer. After 30 hours the potential decreased in the whole measured area to defect potential on the iron part (like displayed in Fig. 6-5). A slow decrease in the whole area rather than a clear delamination front is observed although visible changes happened on the coating surface: small water droplets formed on the coating surface near the defect area on water borne polymer. On zinc the potential is stable over the whole area. Furthermore, the water borne polymer could be peeled off the steel surface after exposure to humid air for six days whereas it adhered well on the zinc part of the sample. Comparison to peel tests in chapter 5.2 indicate that the behaviour of the water borne polymer can possibly be assigned to wet de-adhesion.

6.1.2 Cathodic delamination on steel substrates

Properties of water and solvent borne epoxy-amine polymers are different in terms of water uptake and adhesion at high humidities as shown in chapter 4. As a consequence also SKP measurements show clear differences.

Fig. 6-2c displays the typical sigmoid potential curve detected during cathodic delamination processes at the solvent borne polymer/iron interface [93,105,106,162-169]. A defect containing 0.5 molar KBr is prepared and the electrochemical reaction is initiated in air. A 0.5 molar KBr solution was applied as defect electrolyte and its viscosity was increased by the addition of approximately 3 % of agar and subsequent gentle heating before applying it to the sample. The composition of the sample is indicated in the inlet of Fig. 6-2c. Delamination of the solvent borne polymer is shown after three days of reaction time. The interface potential shifts from -50 mV$_{SHE}$ at the intact coating area to -200 mV$_{SHE}$ in the defect area.

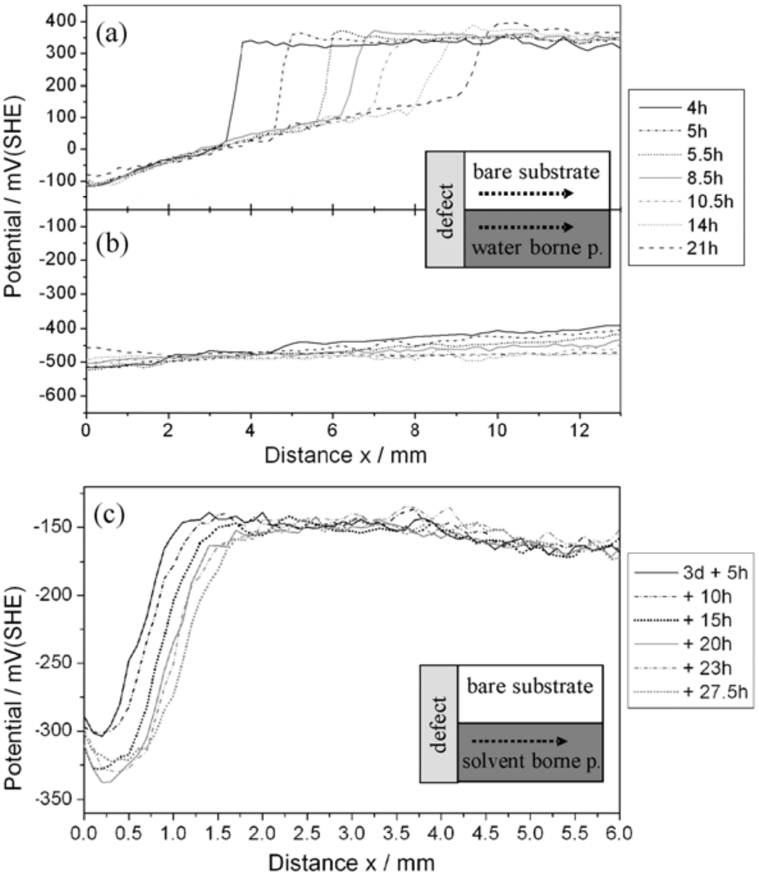

Fig. 6-2: SKP study of ion transport processes in ambient air of > 95 % relative humidity. 0.5 molar KBr solution was applied. Its viscosity was increased by approximately 3 % of agar. Dashed arrows indicate the direction of the SKP line scans in the schematic. a) Potential profiles of the progress of oxygen induced ion transport and liquid spreading processes along the bare low carbon steel substrate. b) Potential profiles recorded in parallel on the water borne polymer coated half of the sample sheet. c) Time dependent linescans of solvent borne polymer on steel.

A similar SKP experiment was performed with the water borne epoxy-amine film applied on a steel substrate. The steel sheet was half covered by the polymer and the other half of the surface remained uncoated. Fig. 6-2a presents the recorded SKP potential profiles on the bare steel surface after the exposition to humidified air with a relative humidity of more than 95 %. The formation of an electrolyte film was observed starting from the electrolyte droplet and proceeding along the uncoated substrate surface. The SKP measurement started after 4 hours reaction time. The recorded potential profiles can be interpreted in agreement with the results of previous studies that focused on the mechanism of oxygen reduction induced electrolyte spreading along bare metal surfaces [145,172-174]. It was pointed out that such processes strongly resemble the mechanism of cathodic delamination along polymer coated metals [145, 172-174]. The initial surface potential of the non-wetted, ‘intact’ area was around 350 mV_{SHE}. An initial reduction of atmospheric oxygen occurs, but any compensating oxidation process is indeed nearly completely inhibited in this section due to a depletion of donor states in the oxide layer [105,106,162-165]. Consequently, steady state conditions are reached at a high anodic overpotential. As soon as an electrolytic connection to the KBr bulk droplet area is established, the kinetic barrier for oxygen reduction diminishes and the interface potential in this section is shifted towards the defect potential. According to [105,106,145,162-165,173,174] the turning point of the sigmoid profile can be assigned to the ‘electrolyte front position’.

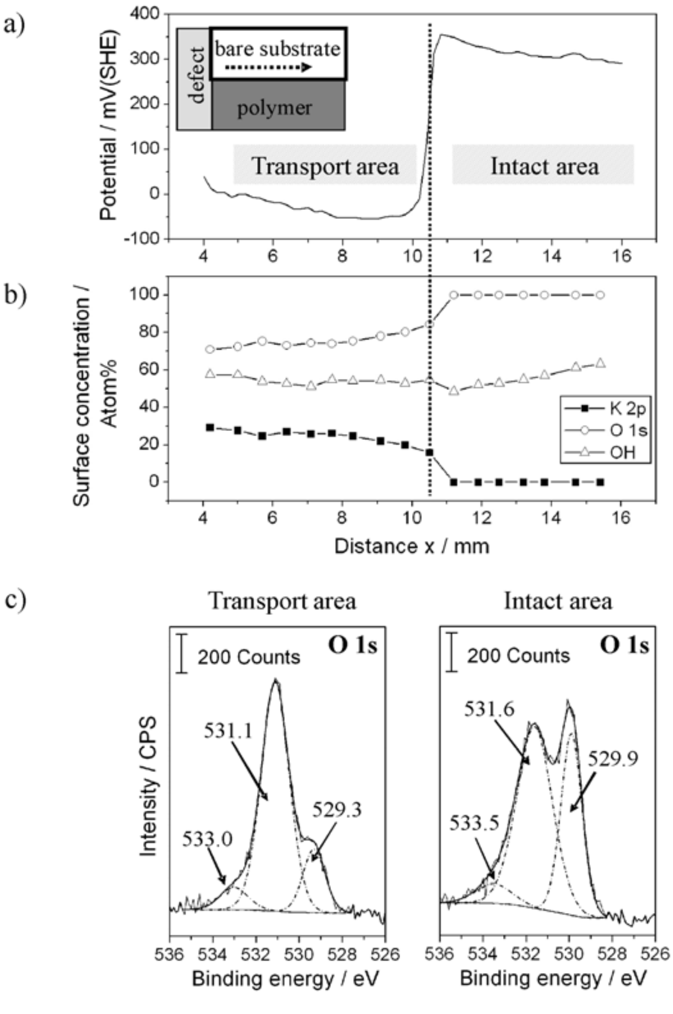

Fig. 6-3: SKP and XPS study of the electrolyte spreading process along the bare low carbon steel substrate in ambient air of > 90 % relative humidity. Defect electrolyte: 0.5 molar KBr solution. a) SKP potential profile recorded directly before the sample surface was dried. b) XPS line scan of the resulting ion distribution. The K 2p signal can be assigned to K^+ ions. Bromide was not detectable. c) XPS study of the local surface chemistry of the surface sections affected (‘transport area’) and unaffected by electrolyte spreading (‘intact area’). The O 1s and Fe 2p signals belong to the XPS line scan displayed in Fig. 6-3b.

Fig. 6-3a presents the resulting SKP potential profile recorded after the termination of the electrolyte spreading experiment on the bare substrate area after 10 hours reaction time in another experiment. Again the characteristic sigmoid graph was recorded. The resulting ion distribution on the sample surface was subsequently analysed by means of XPS. Fig. 6-3b illustrates the received data. In agreement with previous studies it can be concluded that cations of the defect electrolyte were obviously transported along the oxide covered iron interface [145,172-174]. The transition between defect and electrolyte spreading area is indicated by a distinct increase of the K^+ quantity, whereas the transition between spreading area and non-wetted, ‘intact’ surface sections is illustrated by a steep decrease of the potassium amount. Beyond the electrolyte front position at around 10.8 mm no K^+ was detected. Tof-SIMS measurements discussed in previous publications nevertheless confirmed that a low basic contamination level of potassium should be usually expected in this area. But it was also shown that such a basic K^+ concentration is not affected by any ion transport and oxygen reduction process at the surface [145,172-174]. The O 1s signal in Fig. 6-3c exhibits rather small peaks at 533.0 eV (e.g. assigned to C=O) and 529.3 eV (assigned to Fe-O). A dominant peak for hydroxide species is verifiable at 531.1 eV in the electrolyte spreading area compared to the O 1s signal recorded in the ‘intact’ surface section (see Fig. 6-3c). Hydroxide species obviously cover the substrate. The Fe $2p_{3/2}$ signal in Fig. 6-3c does not indicate a presence of metallic iron or of Fe^0 species at 706.8 eV, whereas a small peak is indeed detectable in Fig. 6-3c. These aspects underline a passivation of the steel surface at highly alkaline pH during the electrolyte spreading process [105,162,163]. In this context it is important to note that bromide ions were not verifiable in the ion transport area of Fig. 6-3a and Fig. 6-3b. It is thereby confirmed that no ion diffusion occurred and that wetting of the surface was determined by electrostatic effects induced by oxygen reduction processes at the steel surface [145,172-174].

Fig. 6-2b illustrates the SKP potential profiles recorded on the sample area coated with the water borne polymer. Obviously, delaminated and intact interface sections cannot be easily discerned. The graphs in contrast exhibit a slightly linear increase of the potential with rising distance to the defect area (typically around 150 mV for a distance of 12 mm). Based on the potential displayed in Fig. 6-2b profiles cathodic delamination processes are not verifiable at the interface. But they were expected to occur, because the presence of an electrolyte covered defect in the coating obviously affected the degradation of the coating during exposure to humid air. It was visually confirmed that droplets of liquid had formed on the polymer and that the droplet density decreased with increasing distance to the defect area. However, typical sigmoid shaped potential profiles could not be recorded even after several days of sample exposure and continuous SKP measurements.

A thin conductive water layer at the coating surface may form due to water uptake at high relative humidities and lead to the same potential on the whole substrate/coating interface. This was prevented here by the sample adopted from Fürbeth et al. (Fig. 1 in 106). The high water concentration at the interface can lead to diffusion processes of electrolyte ions at the interface or to faster transport of hydrated ions along the interface and thereby to fast lowering of the potential.

6.1.3 Effects of reduced humidity on the corrosion process

Influence of water at the polymer metal interface was described by Nazarov et al. [171]. Due to this, the influence of humidity on the water borne polymer/steel interface was examined without corrosion processes at the interface. Fig. 6-4 shows that detected potentials of -500 mV at the interface of water borne polymer and steel substrate in Fig. 6-2b result from high water activity at the interface. These potentials at high humidity are similar to potentials which are typically measured in the transport area of cathodic delamination processes. The goal is to understand how the high water activity influences the corrosion process and ion transport. High interphasial water activities and the thereby induced wet de-adhesion may affect ion transport processes along epoxy-amine/steel interfaces.

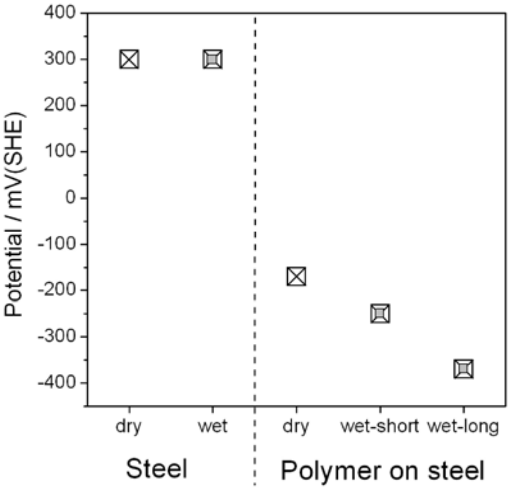

Fig. 6-4: Potential measured by SKP on steelsurface and water borne polymer covered steel surface depending on interfacial water activity (wet-short: exposure to high humidity for 30 min, wet-long: exposure for 2 hours).

The kinetics of cathodic delamination was shown to depend on the water activity in the polymer interphase adjacent to an oxide covered metal substrate. [99,168]. Fig. 6-5 displays the variation of potentials at reduced humidity on a steel substrate coated with water borne polymer. At time zero the corrosion reaction was induced by filling the defect with 0.5M KBr solution. After 10 hours the potential reaches a minimum at x = 0 mm and the potential in the whole observed area decreases after 30 hours until a constant level is reached after 65 hours. At 50 hours the relative humidity is increased to 90 %. However, the potential decrease at 70 % r.h. between 30 hours and 50 hours does not clearly increase at higher humidity.

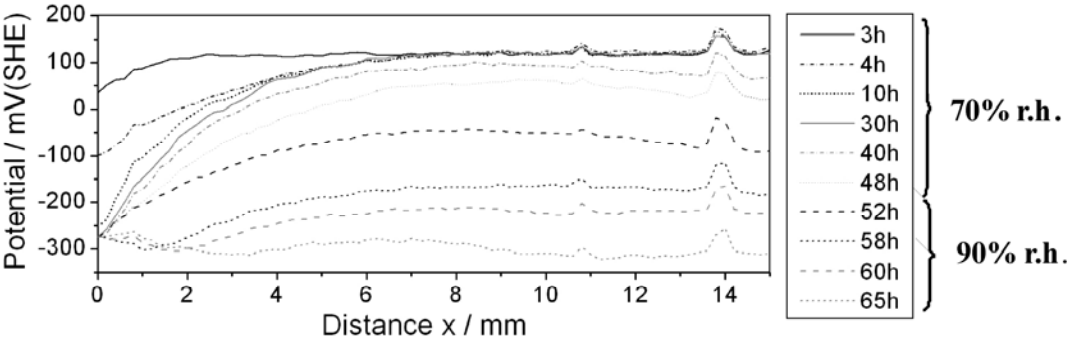

Fig. 6-5: SKP measurement of water borne polymer at reduced relative humidity (70 %) which was increased to 90 % after 50 hours.

It seems that the interfacial water activity reaches a maximum after 30 hours, which leads to wet de-adhesion. At 70% r.h. this process is slower than at 90% r.h. and changes at the interface can be followed better by SKP. With higher humidity the same process is faster and a flat potential is detected after 4 hours of reaction time in Fig. 6-2b.

Fig. 6-6a presents the development of potentials while drying of the water borne polymer. The corrosion reaction is going on for 10 hours. An unspecific linear slope dominates the profile geometry during the first hours of the experiment, similar to the characteristics of the profiles displayed in Fig. 6-2b. Between t = 2.5 h and t = 10 h a decrease of the slope is observed and the interface potentials near the defect and at larger distances to the defect partly equalise. Upon reducing the humidity the potential shifts upward by around 150 mV. Compared to Fig. 6-4 the potential of -220 mV can be interpreted as almost dry polymer/steel interface as it also resembles the potential at x = 15.8 mm after 1 hour of reaction time.

But for a detailed analysis of the corrosion process the polymer layer was carefully peeled off and the steel surface was analysed by XPS. the peel test is displayed in Fig. 6-6c and shows three distinct areas, although measured peel forces are very low. Between 1.5 and 2 mm distance from the defect the peel force is zero, it slightly increases to 0.01 N/mm due to the preliminary irreversible oxidative degradation of the interface [105]. Reversible wet de-adhesion processes at the interface section of x > 7.6 mm finally result in slightly higher adhesion forces of 0.017 N/mm maximum. Thus, the areas can be interpreted as defect, transport area and wet delaminated area.

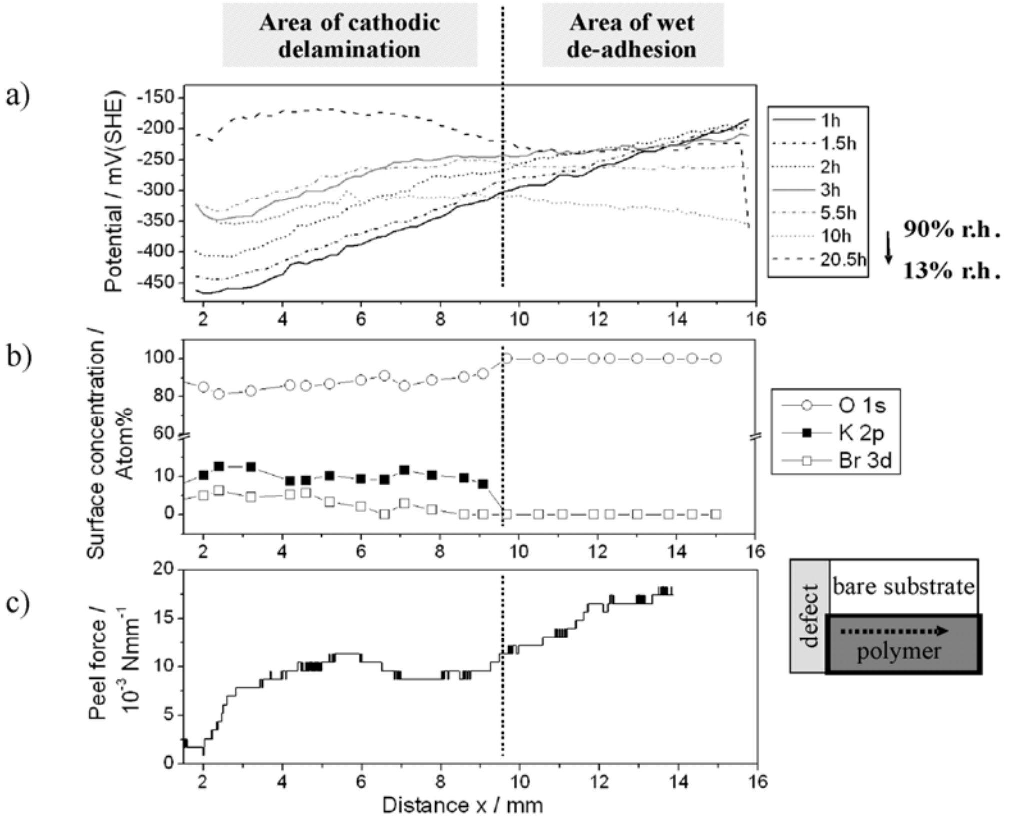

Fig. 6-6: SKP, XPS and peel test study on the water borne polymer coated half of a sample as presented in Fig. 6-3. a) Potential profiles for cathodic delamination in ambient air of >90 % r.h. KBr electrolyte was applied in the defect. b) Potential profiles after the reduction of the humidity at t = 10 hours. c) Forces detected during peeling of the polymer layer after termination of the SKP experiment. d) XPS line scan of the Br 3d, K 2p, O 1s signals and the OH peaks.

A clearer description of the corrosion process is gained by XPS surface analysis after peeling off the water borne polymer. Fig. 6-6b illustrates the resulting line scans for the K^+, Br^- and OH^-/O^{2-} ratio on the steel surface. Two areas can be distinguished. Between x = 0 mm and x = 7.6 mm potassium is present at the interface, but it is not detected at larger distances from the defect. This result corresponds to the expectation that cathodic delamination occurred at the interface next to the defect [172-174]. This can be interpreted as the ‘electrolyte front position’ [105,162,163,173,174]. Fig. 6-6c also displays that bromide ions are present in the area of electrolyte transport. This result allows conclusions towards the mechanism of interfacial ion transport processes.

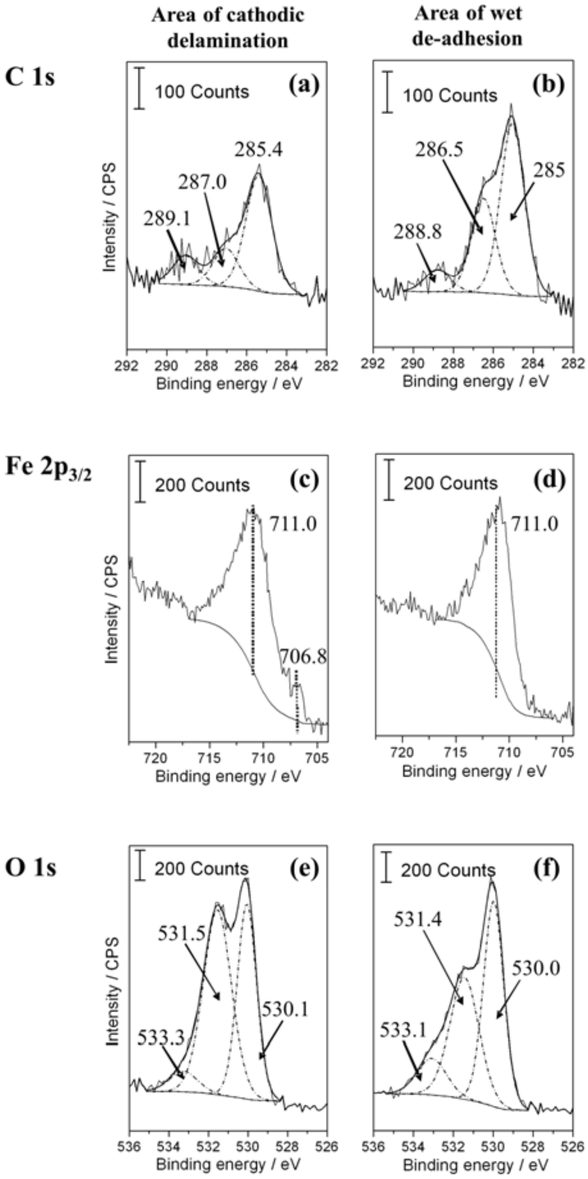

Fig. 6-7: XPS detail spectra recorded in the area of cathodic delamination (left column) and wet de-adhesion (right column). The C1s signal of (a) and (b), the Fe2p peaks of (c) and (d) as well as the O1s detail spectra of (e) and (f) belong to the XPS line scan displayed in Fig. 6-6b.

To support this result Fig. 6-7a and Fig. 6-7b present high resolution spectra of C 1s, Fe $2p_{3/2}$ and O 1s recorded in the two relevant sample sections: area of corrosive delamination and area of wet de-adhesion. Intensity of the carbon components is higher in the area of wet de-adhesion. At the same time the iron signal gives information about the coverage of the steel sample. The Fe^0 component at 706.8 eV is detected in the area of cathodic delamination where less carbon is detected. The O^{2-}/OH^- ratio changes from area of cathodic delamination to area of wet de-adhesion. A higher hydroxide surface concentration is detected in the area of cathodic delamination due to oxygen reduction and hydroxide formation. The C=O peak at 289 eV in the C 1s spectrum is higher in the area of cathodic delamination, but the H_2O/CO_3^{2-} peak at 533.3 eV in the O 1s spectrum is smaller in the same area. This can only be explained by H_2O inclusion at the area of wet de-adhesion.

Posner et al. showed that only cations are transported along polymer/oxide/iron interfaces in humid air and in a humid nitrogen atmosphere [145,173]. Iron substrates coated with non water borne epoxy-amine polymers or coatings based on water borne styrene/acrylate copolymer dispersions were investigated [145,173]. Wielant et al. reported the same preferential cation transport for polyurethane coated steel substrates with different iron oxide structures [174]. SKP potential profiles were also recorded during reactive liquid spreading along uncoated iron surfaces in humid air and humid nitrogen atmosphere [145,173,174]. The thereby detected profile characteristics strongly resemble those detected for cathodic delamination. The same applies to the resulting ion distribution at the surfaces [145,173,174]. These publications support the hypothesis that ion diffusion is not a parameter that affects cathodic delamination on polymer coated or reactive electrolyte spreading processes on uncoated iron, steel or zinc substrates on a macroscopic scale. It seems that rather electrostatic fields are determinant [145,172-175]. The here presented data confirm that this is also true for ion transport processes that proceed along uncoated low carbon steel surfaces (see Fig. 6-3).

However, when these low carbon steel surfaces are coated with the water borne epoxy-amine polymer bromide is detected together with K^+ in the delaminated area. The presence of Br^- shows that the ion transport mechanism in this case differs from the mechanisms discussed for cathodic delamination [105,145,162,163,173,174]. This result can be attributed to the high permeability for water of the water borne polymer, that leads to high water activity at the polymer/steel interface (chapter 4.2) and wet de-adhesion. Swelling of the interphasial polymer layer leads to a very fast diffusion of ions in the interphase region. The water rich interphase promotes the interfacial ingress of anions.

However, it was shown that interfacial ion transport processes could not be induced on zinc surfaces in a nitrogen atmosphere even in the case the substrates were coated with defect-rich styrene/acrylate copolymers [145,173]. The same applied to poorly adhering epoxy-amine layers and increased free volumes at the polymer/zinc oxide/zinc interface [145]. Moreover, it was shown that for polymers films that were deposited on steel from water borne styrene/acrylate copolymer dispersions, only cations of the defect electrolyte were verifiable at the interface [145]. Finally, during oxygen reduction induced electrolyte spreading the interfacial water activity is even higher, and a millimetre thick bulk water layer is proceeding along bare oxide surfaces. However, anions were not verifiable on iron substrates afterwards [173].

6.2 Cathodic delamination of the GPS-modified water borne epoxy-amine film

The effect of GPS on the epoxy-amine/steel interface potential as well as on cathodic delamination is investigated. GPS-modified water borne polymer was shown to be more stable in high humidity in chapter 5. Covalent bonds between polymer chains, GPS and the oxide layer are less sensitive to hydrolysis and provide a major contribution to the overall adhesion forces [63,86,155]. Experiments discussed within this chapter will also support the interpretation of electrochemical processes at steel substrates coated with unmodified water borne epoxy-amine presented in the previous chapter 6.1. With 2.5% GPS peel tests have shown in chapter 5.2 that the interface is stabilised, therefore only this system was used for further measurements in comparison to bare water borne polymer.

6.2.1 Cathodic delamination at reduced humidity

Fig. 6-8 displays SKP linescans of corrosive reaction on steel samples covered with 2.5 wt% GPS containing water borne polymer. The experiment was started at a relative atmospheric humidity of approx. 70 % which was increased to > 90 % after 55 hours. The observed characteristics of the potential profiles, in fact, were comparable when the measurement was started directly in highly humid air. Areas affected by cathodic delamination and intact interface sections can be easily distinguished in Fig. 6-8. The ingress of electrolyte leads to a reduction of the interface potential near the defect. However, the graphs do not exhibit a turning point. A transition area of several millimetres in width is observed between degraded and intact interface sections instead of a sharp potential drop. A similar shape of SKP potential profiles was reported for cathodic delamination processes along polymer coated iron samples that were protected against corrosion by an additional SiO_2 plasma polymer layer or a layer of APS [160]. It is not entirely clear whether a missing turning point in the potential profiles concerns intrinsic properties of an adhesion promoter or the presence of an additional insulating film between an epoxy coating and iron or steel substrates.

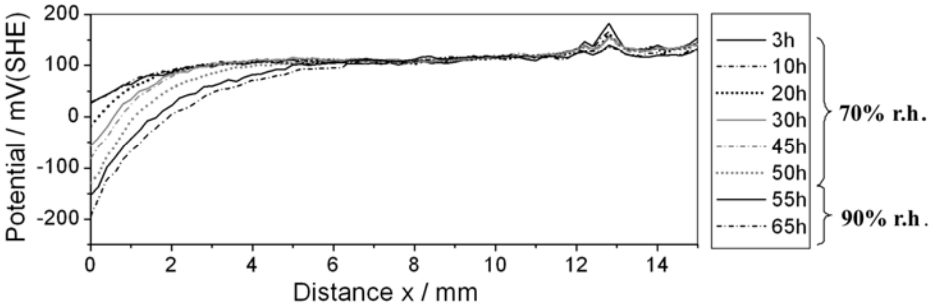

Fig. 6-8: SKP cathodic delamination study on low carbon steel substrates, coated with a GPS modified epoxy-amine (2.5 wt% GPS). Potential profiles were first recorded in ambient air of around 70 % relative humidity. After 50 hours the humidity was increased to > 90 % r.h.. 0.5 molar KBr solution was applied as electrolyte in the defect area.

The EIS and ATR-IR studies of chapter 4.1 indicate that the H_2O activity is reduced when GPS is present at the interface. Wet de-adhesion can be consequently excluded in the GPS-modified water borne polymer. Therefore a variation of the relative atmospheric humidity between 70 % and > 90 % does not influence the shape of the recorded SKP potential profiles (see Fig. 6-8). The ν(OH) peak shapes in ATR-IR spectra of the unmodified water borne polymer in Fig. 4-10a and of the GPS and APS modified water borne polymer in Fig. 5-3b and Fig. 5-6b indicate a similar distribution of water agglomerates in the polymer matrix for the unmodified and GPS modified water borne polymer. This means that the water distribution is obviously not primary responsible for any polarisation or masking effect.

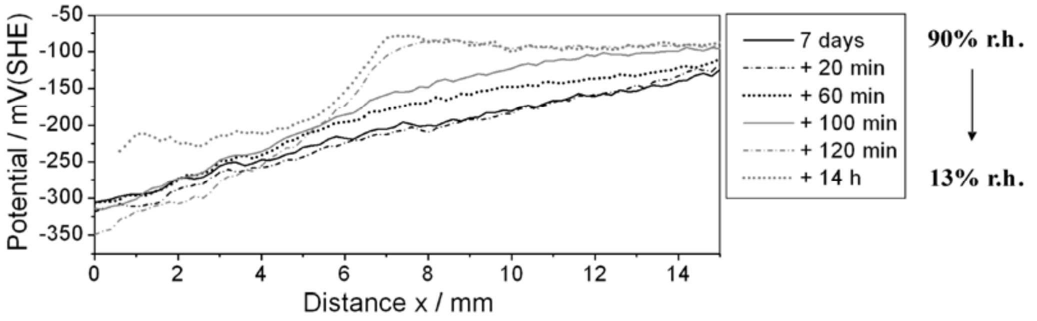

Fig. 6-9: SKP cathodic delamination study on steel, coated with GPS modified epoxy-amine. 0.5 molar KBr solution was applied as electrolyte in the defect area. The sample was exposed to humid air of >90 % r.h. for seven days prior to the SKP measurement. After the initial SKP line scan was recorded the atmospheric humidity has been continuously reduced, fell below approx. 50 % r.h. after two hours and reached around 13 % r.h. after 14 hours.

It is of interest to check whether the interface stabilising effect of GPS is enduring for the analysed water borne epoxy-amine coating. Therefore, the cathodic delamination experiment of Fig. 6-8 was repeated. But this time the sample was exposed to air with a relative humidity of >90 % for seven days prior to the SKP measurement. Fig. 6-9 presents the recorded potential profiles. The first linescan was performed at high humidity, then humidity was decreased down to 13% after 14 hours. The initial 'after 7 days'-graph exhibits a continuous and nearly linear increase of the potential with increasing distance to the defect. The slope is around 180 mV/15 mm (appr. 12 mV/mm) and no characteristic steep potential drop indicates the position of the electrolyte front. This profile strongly resembles the unmodified water borne polymer presented in Fig. 6-6. Even the slope is nearly the same in this particular case (for Fig. 6-2b it e.g. varies around 12.5 mV/mm). The linear slope of the SKP potential profiles reflects the physical and chemical properties of the polymer/steel interface. If the interface region provides a basic electrolytic conductivity, the slope could be at least partly attributed to a depolarisation effect caused by the defect area. A pronounced and steep potential drop between the area of cathodic delamination and the intact interface may be 'smeared' along the entirely coated sample area. Near the defect the SKP potential rather resembles the defect potential. At larger distances to the defect area the potential will reflect the intact interface and exhibit a more positive value. According to Ohm's law the observed linear potential increase then can be attributed to an IR drop (I: current), (R: resistance) [105,162,163]. Usually the SKP detects a strong potential shift nearly down to the defect potential in that case, because the ingress of cations provides a sufficiently conductive electrolytic connection to the defect. However, it is not clear which species are acting as charge carriers in this case. It cannot be explained why potassium cations, which enter the polymer/oxide/metal interface section during cathodic delamination, do not lead to a distinct depolarisation of the transport area in this case.

When the humidity of the surrounding atmosphere was slowly reduced and reached a threshold value of approximately 60 % r.h., a sigmoid potential profile is recorded. It seems that the part between x = 8 mm and 15 mm resembles the intact polymer/substrate interface. At x < 8 mm the lower potential indicates the area of cathodic delamination. Sigmoid potential profiles are usually associated with cathodic delamination [96,105,162,163,168] which obviously proceeds masked towards the detection by SKP unless the interface is dried. The interface stabilising effect of GPS seems to diminish when the GPS-modified water borne polymer coated steel substrates are exposed to humid air for longer times.

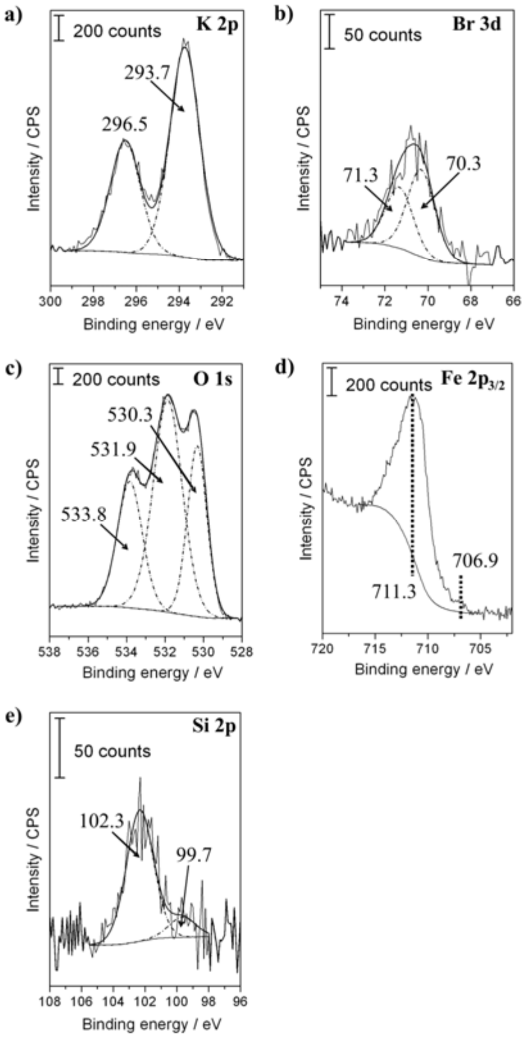

Fig. 6-10: XPS study of the local surface chemistry for the area of cathodic delamination. The detail spectra were recorded at x = 8 mm on the sample presented in Fig. 6-9 after termination of the SKP measurement and removal of the coating.

Fig. 6-10 displays XPS high resolution spectra of K 2p, Br 3d, O 1s and Fe $2p_{3/2}$. They were recorded in the area of cathodic delamination (Fig. 6-9) after the coating was removed from the substrate. The dry polymer was only removed in the transport area because rebonding of GPS-modified water borne polymer is fast during drying (see Fig. 5-8b). K^+ as well as Br^- were detected (Fig. 6-10a and Fig. 6-10b). It is consequently concluded that ion transport processes along steel surfaces that are coated with an unmodified or a GPS-modified water borne epoxy-amine layer proceed with a similar mechanism, at least after some days of exposure to humid air. In chapter 6.1.3 this result was attributed to interfacial capillary forces which promote the ingress of bromide ions. Ion diffusion on the other hand was not expected to be of macroscopic relevance.

The O 1s signal in Fig. 6-10c consists of carbonate or water at 533.8 eV, hydroxide or C-O at 531.9 eV and iron oxide 530.3 eV. Similar as in the area of cathodic delamination for unmodified water borne polymer the hydroxide component has the highest intensity. The shape of the Fe $2p_{3/2}$ signal is similar for both unmodified and GPS-modified samples (compare Fig. 6-10d to Fig. 6-7c), as also in non-corroded samples after peel tests (chapters 4.4 and 5.2). Silicon is verifiable in the area of cathodic delamination for the GPS-modified interface. Fig. 6-10e indicates the presence of Si^{+I} species (peak at 102.3 eV) and Si^0 (peak at 99.7 eV) similar to non-corroded steel surfaces after peel test (chapter 5.2). They can be obviously attributed to molecules or fragments of GPS.

In chapter 6.1.3 it was also concluded that interfacial water amount, wet de-adhesion of the polymer and the absence of sigmoid SKP potential profiles are connected to each other when investigating unmodified water borne polymer/substrate interfaces. The present experiment seems to confirm this. The application of GPS led to a reduction of the interfacial water activity and temporarily stabilised the polymer/steel interface. In contrast to experiments with the unmodified epoxy-amine coating cathodic delamination was verifiable with the SKP. After some days of sample exposure in humid air the stabilising effect of GPS diminished and electrochemical reactions as well as atmospheric corrosion proceeded masked towards a detection by SKP. The interfacial transport of anions together with cations of the defect electrolyte resulted in secondary degradation processes at the interface.

6.3 Cathodic delamination of the APS-modified water and solvent borne epoxy-amine film

Application of APS to the water and solvent borne epoxy-amine polymers leads to increased water activity at the interface to the substrate. Although a stabilising effect is not expected, the systems containing 2 wt% APS are subjected to conditions of cathodic delamination. After one day of reaction time at >96% relative humidity, a peel test gives the results presented in Fig. 6-11. The measurement can be separated in three areas. Section 1 is only assigned to the force curve of the water borne polymer. The coating does not adhere to the steel surface. Section 2 is represented by increased peel forces of 0.02 Nmm^{-1}. For the solvent borne polymer the peel forces are around 0.05 Nmm^{-1}. Section 3 shows a strong increase and a maximum of 0.12 Nmm^{-1} for the peel force of the water borne polymer. This increase results from increasing adhesion at the intact substrate/polymer interface where adhesion of the polymer is strong. The following decrease indicates the cohesive failure of the polymer. A similar curve is measured for the solvent borne polymer with the first maximum at 0.28 Nmm^{-1} and the second maximum at 0.34 Nmm^{-1}.

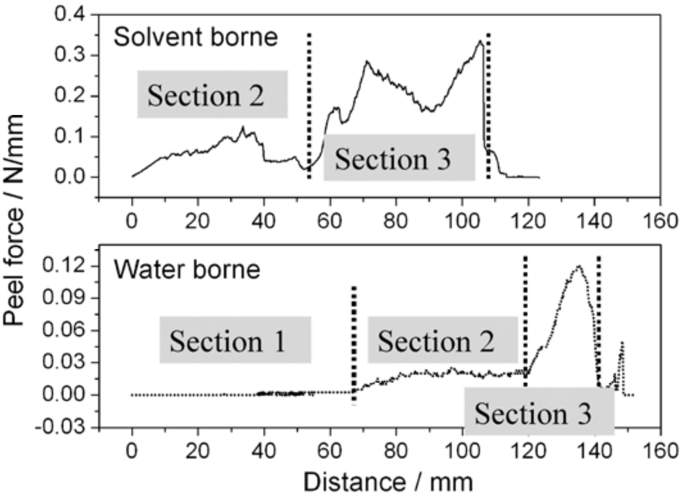

Fig. 6-11: Peel test of water and solvent borne polymer after inducing cathodic delamination with 0.5M KBr in the defect and exposure to humid atmosphere for one day.

Fig. 6-12a show results for water borne polymer with 2 wt% APS: in the first hour after induction of cathodic delamination with addition of the 0.5 molar KCl the potential decreases to defect potential next to the defect and small water droplets on the resin surface can be observed. The decrease of potential is again taking place over the whole range of the measurement and no typical delamination front is detected. Behaviour of solvent borne polymer at 5 µm thickness with 2 wt% APS is shown in Fig. 6-12b. Potential decrease is slower than in the water borne system and the intact interface is stable during one day. Due to lower water uptake of this system the interface exhibits lower water concentration and the system is more stable under conditions of high humidities as shown in the previous chapter.

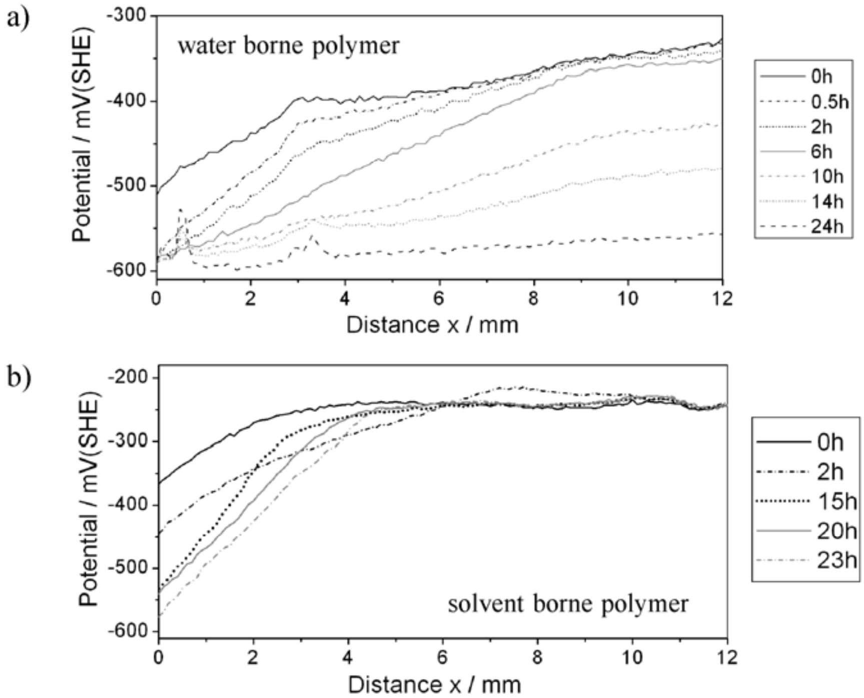

Fig. 6-12: a) SKP measurement of water borne polymer with 2 wt% APS and b) solvent borne polymer with 2 wt% APS

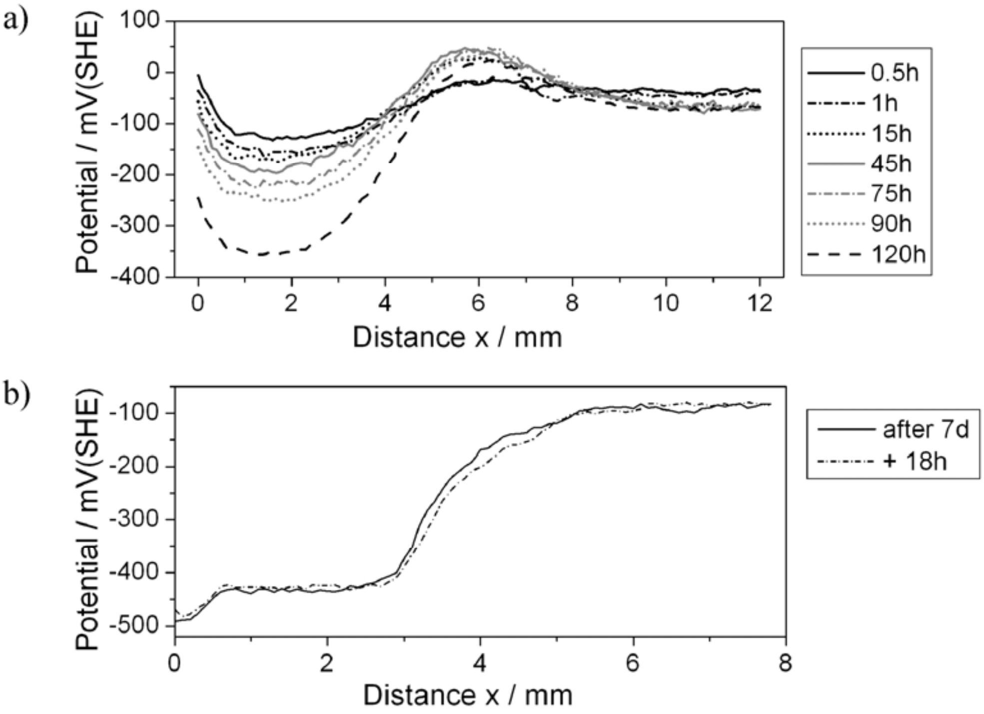

Fig. 6-13: a) SKP measurement of solvent borne polymer with 5 wt% APS and b) solvent borne polymer on APS primer.

The three sections of the peel tests in Fig. 6-11 can be explained with SKP measurements in Fig. 6-12. Section 1 of the force curve for water borne polymer represents the delaminated area whereas the second part represents the area where a broad front is detected by SKP.

When enough force is applied in the peel test, the coating can be completely removed also from the third part - the intact part of coating - due to partial wet deadhesion.

Furthermore, SKP profiles in Fig. 6-13 were acquired for solvent borne coatings with 5 wt% APS and on an APS primer. Water uptake at the interface was not influenced by addition of 5 wt% APS and peel tests showed high stability on the APS primer. When APS is present as a layer on the substrate surface, the sample is very stable under conditions of corrosive de-adhesion: after seven days of reaction time a large part of the sample is still intact and the delamination front does not proceed anymore.

6.4 Conclusions

The SKP technique was applied to study the influence of wet de-adhesion on the cathodic delamination process starting from a corroding defect. To date, there is hardly a study available that focuses in detail on the complex interaction of interface potential shifts caused by cathodic delamination and wet de-adhesion. In this context it was shown that sigmoid SKP potential profiles cannot be recorded on epoxy-amine covered steel substrates when the initial water activity at the interface is extremely high. The mechanism of cathodic delamination is shown to be different in that case, as well. Ex-situ XPS measurements helped to characterise the ion surface distribution. Peel tests were applied to distinguish between interface sections that are deteriorated by wet de-adhesion and areas degraded by simultaneously occurring wet de-adhesion and interfacial oxygen reduction processes.

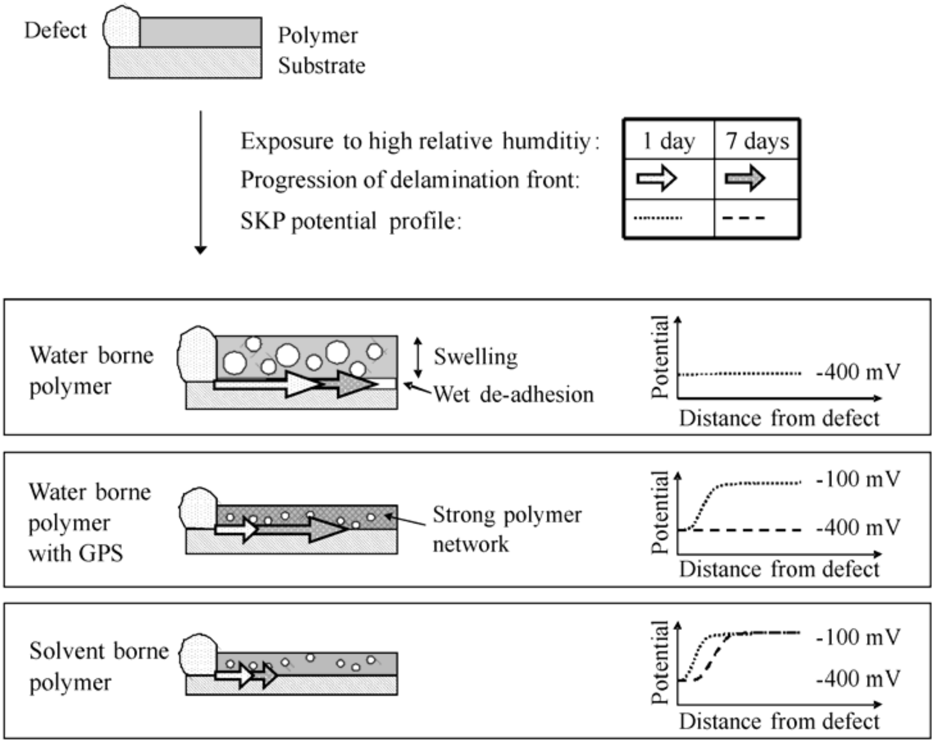

Fig. 6-14: Schematic: behaviour of different systems of water and solvent borne resin at exposure to corrosive environment

The schematic in Fig. 6-14 describes the main results related to the water borne polymer, the GPS modified water borne polymer and the solvent borne polymer. These samples show characteristic water uptake and interface stabilities which can be applied for the interpretation of the detected SKP potential profiles.

7 Molecular understanding of adhesion and diffusion in corrosion protection coatings

Adhesion of corrosion protection coatings is gained by interaction of functional groups with the substrate surface. In epoxy-amine polymers H-bonding or covalent bonding with the steel surface is established between hydroxides, ketons, amines and the oxidic substrate surface. An experiment modelling the behaviour of organosilane additives GPS and APS during film formation was set up. XPS surface analysis shows the simultaneous adsorption of epoxy-amine model molecules and organosilanes. The interface composition was further studied after variation of the organosilane concentration in the adsorption experiment.

Not only adsorption but also corrosion reactions are taking place on a microscopic scale. An in-situ backside SERS experiment was set up as a new method for detection of the electrochemical reaction at the substrate/polymer interface. A self-assembled monolayer of 2-mercaptobenzothiazole (MBT) was adsorbed onto SERS active gold and silver surfaces. Changes of the structural monolayer constitution were tracked in-situ by SERS and SKP during oxygen reduction induced ion transport and electrolyte spreading along the organic/substrate interfaces. SKP potential profiles and ToF-SIMS analysis of the ion distribution at the surface showed that the approach is suitable to simulate cathodic delamination processes. Complementary XPS studies helped to analyse organic species formed during the deterioration of the monolayer.

Diffusion of organic molecules through protective polymer films is important for self-healing processes during corrosion reactions at polymer/substrate interfaces. Diffusion kinetics strongly depend on structural properties of the polymer. Polyelectrolyte films built up from polyacrylic acid and polyallylamine hydrochloride were modified by loading with Ag nanoparticles and by curing at elevated temperatures. The in-situ backside SERS approach was applied to follow the diffusion of MBI in aqueous solution through the PE which depended on the post treatment. The stability of polyelectrolyte films during the experiments and chemical changes during post treatment were probed by FTIR spectroscopy. The barrier function of the polyelectrolyte towards water is determined by EIS.

7.1 Competitive adsorption of organosilanes and epoxy-amine model molecules on iron oxide surfaces

Polymer/metal interfaces were studied on a microscopic scale in order to understand and improve adhesion. Thereby the mechanical theory and adsorption theory of adhesion were developed [58,59,176]. Adsorption theory involves physical adsorption forces like van der Waals-forces and primary chemical bonding which is called chemisorption. On polished, cleaned surfaces adsorption of epoxy-amine model molecules can be examined as a function of chemical interaction with the substrate surface. Wielant et al. [177] found distinct adsorption geometries depending on the functional group of epoxy-amine model molecules. Adsorption of such molecules is explained by Brönsted and Lewis acid-base interactions with the oxidic metal surface [178,177]. Organosilanes form thin layers on iron oxide surface if adsorbed from aqueous solution. Binding to the substrate is established by Si-O groups or the functional groups that they carry [77,83]. Self-assembly is only found for organosilanes carrying long alkyl chains [75]. Organosilanes as additives in epoxy-amines are found at the interface after peel tests (chapter 5.2) due to segregation and diffusion.

Competitive adsorption of polymer functional groups and of organosilanes is studied. Water is used as solvent for adsorption of organosilanes. This experimental step does not only reveal adsorption of APS or GPS on an already covered substrate, but at the same time shows the behaviour of the adsorbed components in presence of water. Wet adhesion was shown before to be an important property of polymer components. The surface composition after all experimental steps is analysed by XPS, but high resolution spectra reveal the contribution of single components to the relative amount of detected elements.

Different additive concentrations are applied in the studies concerning water uptake and diffusion of water and solvent borne polymers. Increasing water uptake was determined in the polymer/substrate interphase by ATR-IR spectroscopy. But the amount of silicon at the substrate surface, i.e. the amount of organosilanes covalently bonded to the iron oxide was not determined. XPS will again reveal the interface composition depending on the organosilane concentration in the applied solution.

7.1.1 Adsorption of organosilanes on covered iron oxide surfaces

Amine and epoxy components of water and solvent borne polymers used in chapters 4, 5 and 6 were substituted by two model molecules: diethylentriamine (DETA) and diglycidylether-bisphenol A (DGEBA) (Fig. 7-1b and Fig. 7-1c) are used as model molecules for the hardener (amin component) and the binder (epoxy component), respectively. Adsorption of organosilanes from aqueous solution on a sample covered with DETA or DGEBA was observed according to the experimental procedure described in Fig. 7-1. APS adsorption was observed for a DETA covered substrate in order to observe only the adsorption behaviour of both molecules without a chemical reaction between the adsorbates. GPS adsorption was observed on a DGEBA covered sample, respectively.

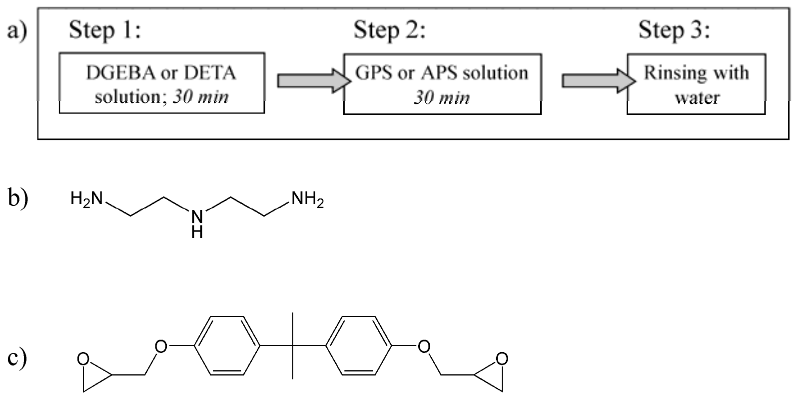

Fig. 7-1: a) 3-step adsorption experiment. Step 1: immersion of Fe (6.5nm thickness) covered silicon wafer in 10^{-5} molar solution of DGEBA or DETA for 30 min. Step 2: immersion in 10^{-5} molar solution of GPS or APS for 30 min. Step 3: rinsing with 10 ml deionised water. b) Diethylentriamine (DETA). d) Diglycidylether bisphenol-A (DGEBA).

The XPS analysis of the three steps of the DETA/APS adsorption onto an iron covered silicon wafer are displayed in Fig. 7-2. Ethanol was used as a solvent for DETA in order to achieve coverage of the substrate in the first step. APS was adsorbed in the second step from water. The intensities of Fe 2p and O 1s are higher after APS adoroption than after DETA adsorption. Of course the use of water as solvent for APS leads to a higher O 1s surface concentration. Furthermore the adsorbed layer thickness can play a role for the detection of the subjacent substrate surface: the result displayed in Fig. 7-2 indicates a thinner layer after APS adsorption compared to DETA adsorption.

After subsequent DETA and APS adsorption the sample shows contributions of both species. The Si 2p signal obviously results from APS adsorption. The C 1s detail spectra cannot be used for differentiating the adsorbates: the C 1s detail spectra of both adsorbates resemble each other because only CH_2 components are detected in both cases. The same applies to the N 1s detail spectra. In presence of water APS can replace adsorbed DETA, because interaction of H-OH and Si-OH with the iron oxide surface is stronger than NH_2 interaction with iron oxide. However, the surface concentration of C 1s is higher after subsequent DETA and APS adsorption than after the single APS adsorption step, which indicates that also DETA is present on the sample surface.

.

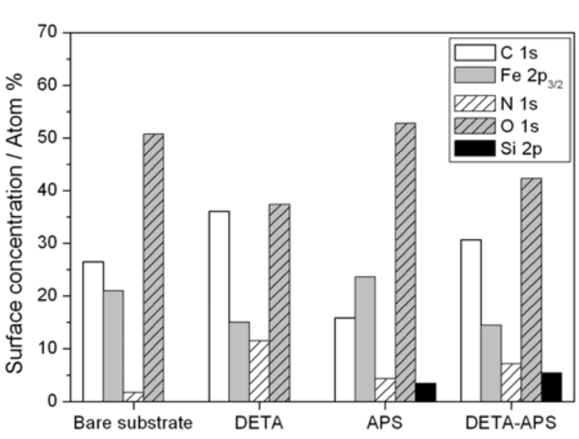

Fig. 7-2: XPS surface analysis of 3-step adsorption experiment with DETA and APS

Fig. 7-3 displays the DGEBA/GPS adsorption experiment: a DGEBA layer was adsorbed on the iron oxide substrate from tetrahydrofurane in the first step and GPS was adsorbed from water in the second step. In Fig. 7-3a the surface concentration of the detected elements are displayed on the iron oxide substrate before adsorption, after DGEBA adsorption (step 1), after GPS adsorption (only step 2) and after subsequent DGEBA and GPS adsorption.

After step 3 both DGEBA and GPS are detected on the substrate. The detection of the Si 2p signal again indicates the presence of the organosilane GPS. In the case of DGEBA and GPS both molecules can be discerned by their C 1s high resolution spectra: the C-C component in the C 1s spectrum is shifted from 284.8 eV (Fig. 7-3c) to 284.5 eV (Fig. 7-3d) due to contributions of the aromatic groups of DGEBA (284.3 eV in Fig. 7-3b). The intensity of the C 1s peaks shows higher coverage of the substrate after the subsequent DGEBA/GPS adsorption than after single GPS adsorption. Interaction of ether and OH groups of DGEBA is weak in comparison to silanol interaction of GPS with the iron oxide surface.

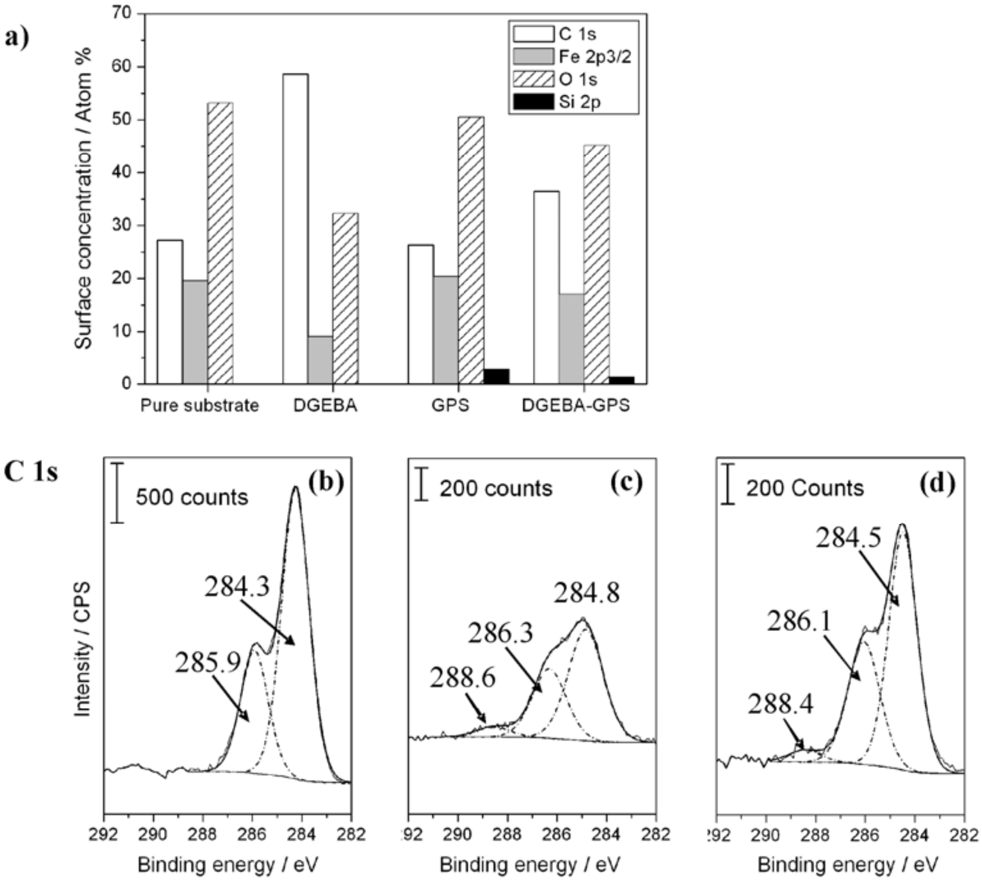

Fig. 7-3: XPS analysis of surface composition in 3-step adsorption experiment. a) Surface concentration of detected elements. C 1s high resolution spectra of b) single DGEBA adsorption, c) single GPS adsorption and d) after subsequent DGEBA and GPS adsorption as displayed in Fig. 7-1. High resolution spectra are referenced to the signal of Fe_2O_3 at 530 eV.

Also PM-IRRAS measurements were performed for both systems. They show the presence of organosilane by the Si-O-Si stretching vibration after the second step of the experiment and decreasing intensity of DETA or DGEBA, respectively. Also Senett et al. found that GPS adsorption on iron oxide was less influenced in presence of water than DGEBA adsorption [83].

7.1.2 Adsorption of hardener and APS on iron oxide depending on APS concentration

The addition of APS to the epoxy-amine polymers obviously leads to a different tendency of water uptake in impedance and ATR-IR results, depending on APS concentration. How organosilanes behave during film formation is partially answered by studies performed by Abel and coworkers [86]. Diffusion or segregation of APS to the interface has thereby been proven by different approaches. Drying times of several days of the studied water and solvent borne polymers assure APS diffusion to the substrate as observed by Wapner et al. [160] and shown in XPS studies in chapter 5, where silicon is detected on all surfaces.

Simultaneous adsorption of hardener (amine component of water borne polymer) and APS on the iron covered silicon wafer was studied depending on the APS concentration (0.5 wt%, 2.5 wt% and 5 wt%). The combination of hardener with APS was chosen to avoid chemical reactions which would modify the adsorption experiment. After immersion of the substrate for one hour in the hardener/APS solution, it was rinsed followed by 10 min of ultrasonic cleaning in order to remove excess unbonded molecules (Fig. 7-4).

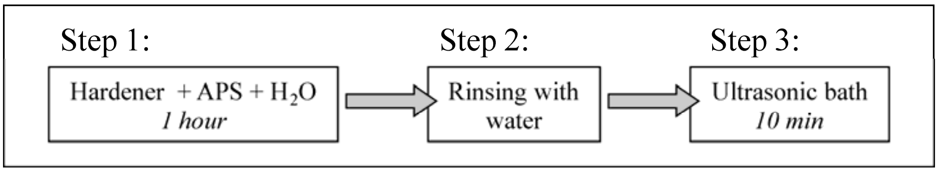

Fig. 7-4: 3-step adsorption experiment. Step 1: immersion of Fe (6.5nm thickness) covered silicon wafer in 10^{-5} molar solution of DGEBA or DETA for 30 min. Step 2: immersion in 10^{-5} molar solution of GPS or APS for 30 min.

Fig. 7-5 displays the XPS surface analysis after the above described experiment which was performed with aqueous solutions of pure hardener, pure APS and hardener with 0.5 wt%, 2.5 wt%, 5 wt% and 10 wt% APS. Surface concentrations of carbon, iron, oxygen, nitrogen and silicon are displayed as a function of the solution composition in Fig. 7-5a. A tendency of changing surface composition depending on APS concentration is not observed. In general, both molecules adsorb and silicon is always present on the surface, if APS is added to the solution. Fig. 7-5b, Fig. 7-5c and Fig. 7-5d display high resolution spectra of the hardener, of the mixtures and of APS. They show that the surface is mostly covered by the hardener.

The O 1s high resolution spectrum is composed of Fe_2O_3 (530 eV), OH (531.2) and C=O (533.2 eV) in Fig. 7-5c. The high intensity of the C=O peak is thereby comparable to the hardener O 1s spectrum in Fig. 7-5b. The C 1s high resolution spectrum detected after step 3 (Fig. 7-5c) is also very similar to the hardener spectrum (Fig. 7-5b). It consists of C-C (285.1 eV) and C-O (286.7 eV). At 291.7 eV in Fig. 7-5b and at 292 eV in Fig. 7-5c the π-π shake-up of an aromatic component of the hardener is detected. The N 1s spectrum shows a higher concentration of NH_2 at 399.7 eV than protonated NH_3^+ at 401.6 eV in Fig. 7-5b and Fig. 7-5c.

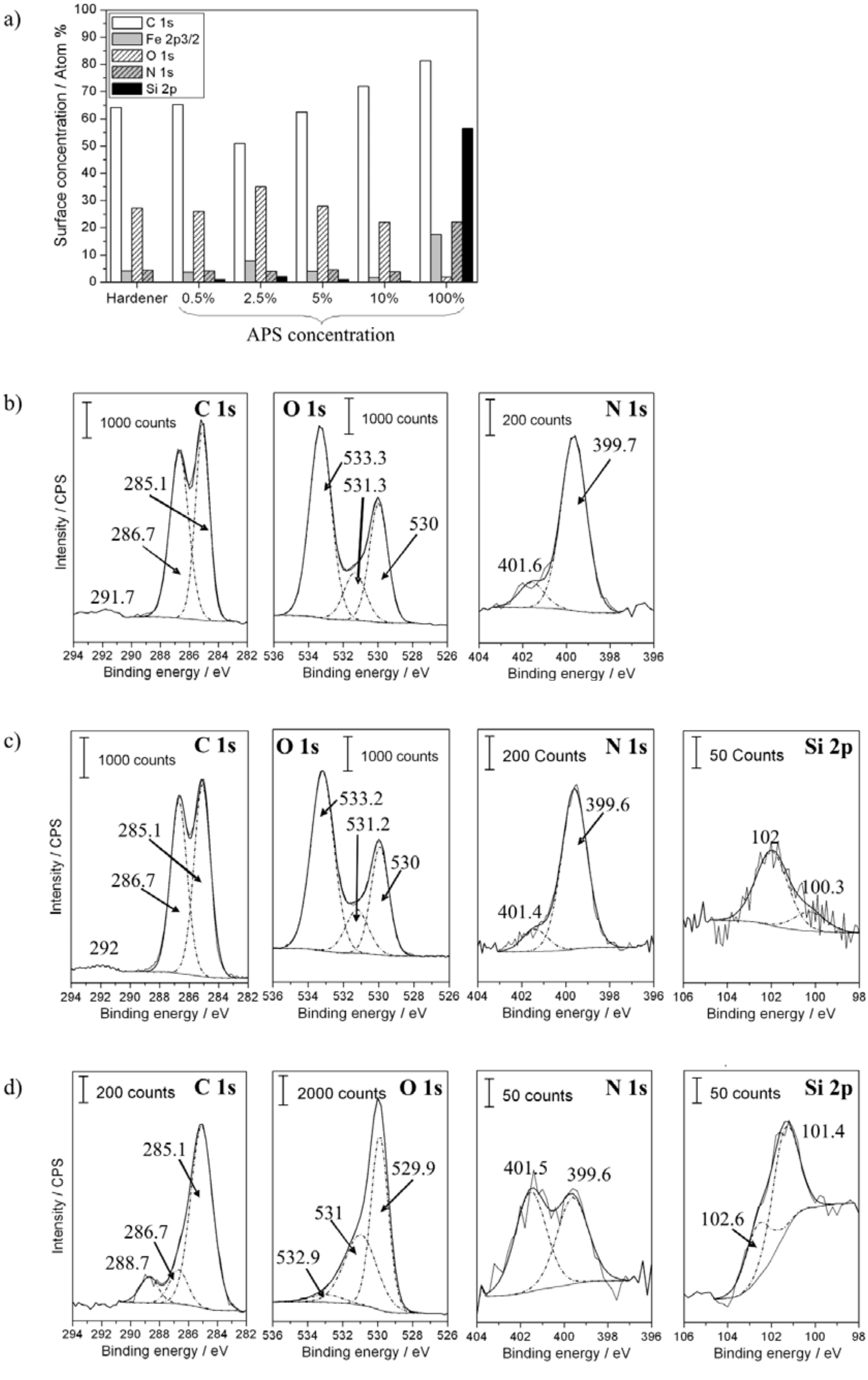

Fig. 7-5: Adsorption of hardener with 0 wt%, 0.5 wt%, 2.5 wt%, 5 wt%, 10 wt% APS and adsorption of pure APS from aqueous solution. a) XPS analysis of surface concentration of elements. High resolution spectra after b) pure hardener adsorption. c) hardener with 5 wt% APS, d) pure APS adsorption.

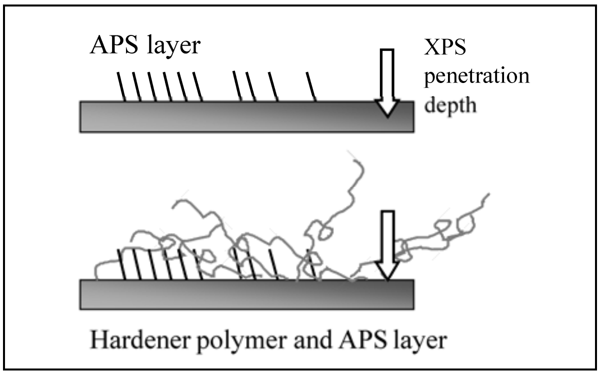

Fig. 7-6: Schematic of XPS measurement after APS adsorption and simultaneous hardener and APS adsorption on iron oxide surface

The presence of APS is only detectable in the Si 2p spectrum. Of course a lower intensity of Si 2p is measured after step 3 (Fig. 7-5c) than on the pure APS sample (Fig. 7-5d). Higher oxidation states are detected on the pure sample than on the mixed sample. Furthermore, the thickness of the adsorbed layer is determined by the hardener adsorption, because the Fe $2p_{3/2}$ surface concentration is higher after pure APS adsorption. In general, this shows that independent on the surface coverage of APS, the polymers of the aqueous hardener solution hide the substrate surface due to a high molecular mass compared to APS as described by the schematic in Fig. 7-6.

7.2 In-situ study of the deterioration of thiazole/gold and silver interfaces during interfacial ion transport processes [2]

Oxidative degradation of the polymer/substrate interface is a challenging economical problem. In many cases it leads to mechanical failure of adhesive joints as well as to a total loss of surface corrosion protection of metallic components. Cathodic delamination and interfacial ion transport processes are often responsible for proceeding interface deterioration and were introduced in detail in chapter 6.

Basic studies that focus on structural changes at the organic/substrate interface can be performed with simplified sample compositions. This in particular applies to monolayers adsorbed on metal or oxide surfaces. In fact, still little is known about the degradation of the organic structure during interfacial ion transport processes. Spectroscopic techniques are generally suited to characterise molecules, but only a few spectroscopic methods can be used to probe buried interfaces, as well. In the present study, a backside-SERS approach is introduced. Samples are probed in-situ while oxygen reduction induced ion transport is proceeding along the interface. Fig. 7-7 schematically displays the "backside" geometry for Raman spectroscopy experiments based on the Kretschmann design [179,180]. This approach prevents a degradation of the monolayer that could be caused by the incident laser beam itself. Self-assembled monolayers adsorbed on SERS active gold and silver surfaces are under investigation. Because thiol monolayers formed on gold are an already well-established system [110,181,182], MBT was selected for the experiments in the present study. Moreover, MBT is also known to function as a corrosion inhibitor for copper and its alloys [183-185]. At MBT/Au interfaces no complex oxide structures form during oxygen reduction induced ion transport processes [186]. Thus, SERS results can be exclusively attributed to chemical changes of the monolayer. An oxide layer can be generated on silver surfaces [186]. Consequently, effects observed at MBT/silver interfaces can be even better compared to the properties of iron, zinc and copper substrates.

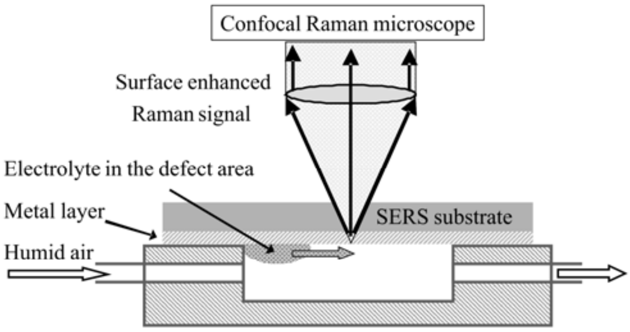

Fig. 7-7: Scheme of the applied backside-SERS setup for the in-situ investigation of ion transport processes along the sample surface. The viscosity of the defect electrolyte droplet is increased by agar and the cell volume is continuously purged with humid air.

---

[2] The text of section 7.2 was adopted from publication [172].

SERS spectra presented in this study will be correlated to an XPS analysis of the oxidation states of sulfidic MBT functionalities. Time-of-Flight Secondary Ion Mass Spectrometry (ToF-SIMS) is applied to reveal the local distribution of characteristic ionic species and will be compared to in-situ SKP measurements of the electrolyte wetting progress. It will be evaluated to what extent oxygen reduction induced ion transport processes along monolayer coated SERS substrates can be compared to the mechanisms of cathodic delamination. This is a prerequisite to succeed in a sophisticated analysis of molecular changes to complex polymer/substrate interfaces in the future.

7.2.1 Oxygen reduction induced ion transport processes along gold and silver substrates

Noble metals like Au and Ag are conductive. As a consequence it was expected that oxygen reduction induced ion transport processes can be initiated along their surfaces. Such processes should be determined by a mechanism similar to reactive electrolyte spreading, which was observed on uncoated zinc and iron substrates [145,173,174,187]. Electrolyte spreading on Zn and Fe, on the other hand, strongly resembled cathodic delamination at buried polymer/iron and polymer/zinc interfaces [145,173,174,187]. To simulate such processes also on surfaces of noble metals, zinc powder was brought onto gold and silver substrates and covered with a droplet of 0.5 molar KBr solution. The liquid was prevented from simple leaking by increasing its viscosity with the addition of around 3 % of agar and subsequent gentle heating before applying it to the sample [173,174]. Exposed to highly humidified air, the formation of a liquid film of low viscosity then could be observed starting from the electrolyte droplet and proceeding along the substrate surface. Without zinc, no or extremely slow electrolyte transport was detectable. The effect of Zn was interpreted as an accelerator for the anodic reaction in the bulk electrolyte covered defect area. In contrast to gold, zinc tends to dissolve [186] and obviously efficiently balances cathodic reduction processes of atmospheric oxygen at the edges of the electrolyte droplet and in the area of additional liquid spreading [145,173,174,187,188].

We were able to track the progress of electrolyte transport in-situ with the SKP. Fig. 7-8 presents the recorded potential profiles. Generally, two potential levels are characteristic. It will be shown below that they can be interpreted in the same way as usually done for SKP potential profiles received from cathodic delamination experiments e.g. at polymer/iron interfaces [93,105,106,145,162-165,173,174]. The initial surface potential of the non-wetted, “intact” area is around 800 mV_{SHE} for both the Au sample and the Ag sample. An initial reduction of atmospheric oxygen will occur, but any compensating oxidation process is indeed nearly completely inhibited in this section [105,106,162-165], especially due to the noble character of Au and Ag. Consequently, steady state conditions will be reached at a high anodic overpotential. As soon as an electrolytic connection to the KBr bulk droplet area is established, the kinetic barrier for oxygen reduction diminishes and the interface potential in this section is shifted down by approximately 250 mV for gold and by between 400 mV and 700 mV for silver. It should be noted that the potential of the wetted area does not correlate with the corrosion potential of zinc in this case, which is expected to vary usually around 800 mV_{SHE} [106,164,165].

Electrolyte ion transport obviously proceeds faster on gold (approx. 9 mm in around 90 min) than on silver (approx. 9 mm in around 150 min). This is surprising in the sense that the potential difference between intact and delaminated area, which was suggested to reflect the driving forces for cathodic delamination [105], is always smaller for gold than for silver (see Fig. 7-8). Obviously, it is not a suitable parameter to predict the progress of reactive electrolyte spreading. It rather can be expected that the oxygen reduction induced ion transport is inhibited on silver because an oxide layer is formed at high interfacial pH and in the presence of oxygen [186]. It will inhibit the electron transfer reactions. Fig. 7-8b furthermore displays that the surface potential of the defect area is continuously shifting up during the experiment. This was frequently observed on bare silver, not on bare gold and occasionally also detected when investigating electrolyte spreading processes along iron samples with different passive structure at the surface [174]. We assume that the mentioned effect can be attributed to silver oxide growth and/or its morphological and constitutional reorganisation at increasing pH during the ongoing reduction of atmospheric oxygen [186].

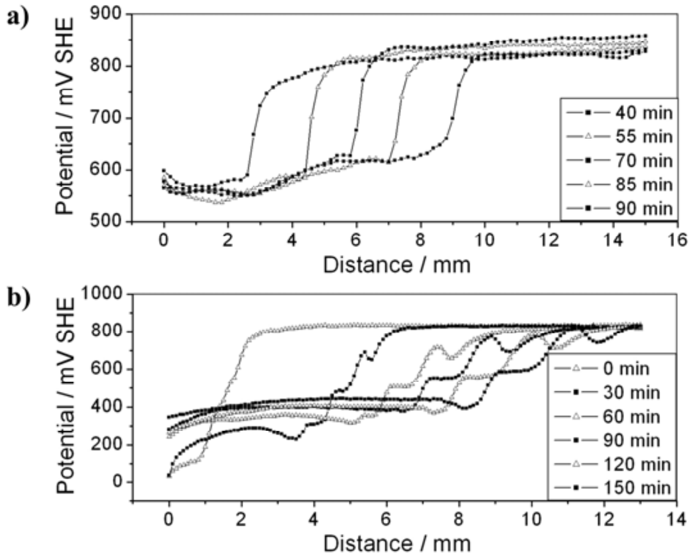

Fig. 7-8: SKP potential profiles of the ongoing ion transport process in humid air, a) on bare Au, b) on bare Ag. Applied electrolyte: highly viscous 0.5 molar KBr solution.

Fig. 7-9a exemplarily illustrates the expected oxygen reduction induced ion transport and electrolyte spreading mechanism on silver and gold. It was intended to study its effect on a self-assembled thiol monolayer. Therefore, ion transport processes along MBT/gold and MBT/silver interfaces were tracked with the SKP. Fig. 7-10a presents the received potential profiles recorded after MBT adsorption on a gold surface (see Fig. 7-9b). The basic characteristics of the graphs are comparable to those of Fig. 7-8. In contrast, rather a transition area of several millimetres in width was detectable between already wetted and intact interface sections instead of a sharp potential drop. It could not be entirely clarified whether this finding concerns intrinsic properties of the MBT/Au interface or just statistically occurs. However, a similar shape of SKP potential profiles was already reported for cathodic delamination processes along polymer coated iron samples, which were protected against corrosion by an additional SiO_2 plasma polymer layer or a layer of 3-aminopropyl-(trimethoxy)-silane (APS) [189].

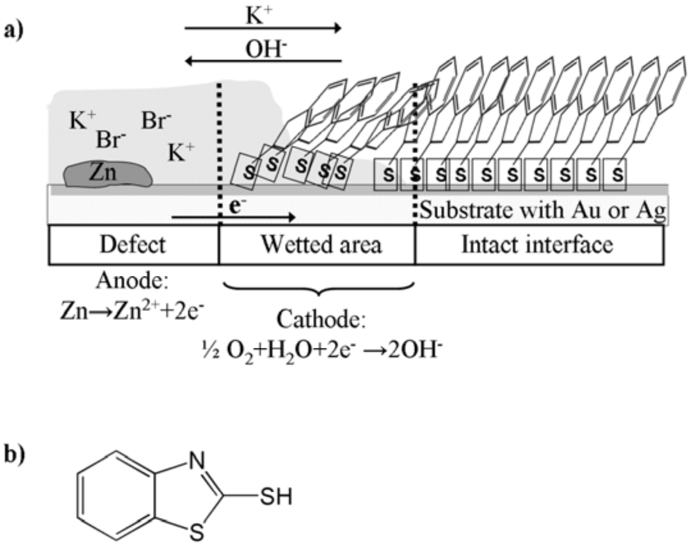

Fig. 7-9: a) Schematic illustration of the mechanism of oxygen reduction induced ion transport processes along thiol/gold and thiol/silver interfaces in humid air. A highly viscous droplet of 0.5 molar KBr solution was used as defect electrolyte for the experiments presented in this study. A layer of Zn powder in the defect area supports the anodic process of metal dissolution. b) Chemical formula of the MBT molecule.

Fig. 7-10b presents the resulting ion distribution, detected with ToF-SIMS after termination of the SKP measurement. According to the conclusions drawn in [145,173,174] three areas can be distinguished. Bromide was solely detectable within the defect area. At the borderline between defect area and area of electrolyte transport its amount reaches a basic contamination level [173,174]. The potassium distribution on the other hand corresponds to the SKP potential profiles. It indeed reflects the broad transition zone between wetted and non-wetted area. A continuous decrease is obvious between around x = 9 mm and x = 12 mm. Beyond this point a constant contamination level of K^+ is maintained. According to [145,173,174] it has to be expected that potassium recorded in the 'intact' area was not affected by any interfacial ion transport processes during the SKP experiment. The ion profiles, in fact, confirm that the composition of the spread liquid is different from that of the bulk KBr droplet in the defect area. Instead of bromide as counter ion for potassium, hydroxide was verifiable (see Fig. 7-10b). This result corresponds to ion distributions detected also on coated and uncoated iron and zinc samples after interfacial ion transport processes were initiated [145, 173,174]. That means that oxygen reduction processes occur within the area of reactive liquid spreading. They lead to hydroxide formation and – according to the mechanism of cathodic delamination [105,162,163] – alkalise the interface. This also explains why no relevant amount of zinc ions was detected in the area of interfacial ion transport. Zn^{2+} precipitates as $Zn(OH)_2$ in alkaline environment and consequently remains in the defect area. Zinc hydroxide may dissolve as zincates when the pH further increases [186], but due to the negative charge of the complexes, they will not be transported along the electrolyte spreading area. Fig. 7-10b also proves that the electrolyte spreading progress (around 12 mm in 105 min) at a thiol/Au interface does not necessarily proceed decelerated compared to the same process along pure gold surfaces (see above). An inhibiting effect of MBT is not verifiable.

Moreover, Fig. 7-10a displays that the MBT/gold interface potential is not stable during the SKP measurement; a continuous shift of the intact interface section to lower potential values is obvious in this case, but may also occur statistically [174]. Gold will remain an inert material during the exposure to humid air due to its noble character [186]. Consequently, it is speculated that the mentioned potential shift may be correlated to minor structural reorganisations of the monolayer. After the sample is transferred from ambient atmosphere to the SKP chamber with its high relative humidity, the water activity at the MBT/Au interface increases until it is in equilibrium with the surrounding atmosphere [99]. This may induce a change of the interfacial dipole moment [177] if the monolayer adsorption geometry and bonding adjusts to the increased interfacial water amount.

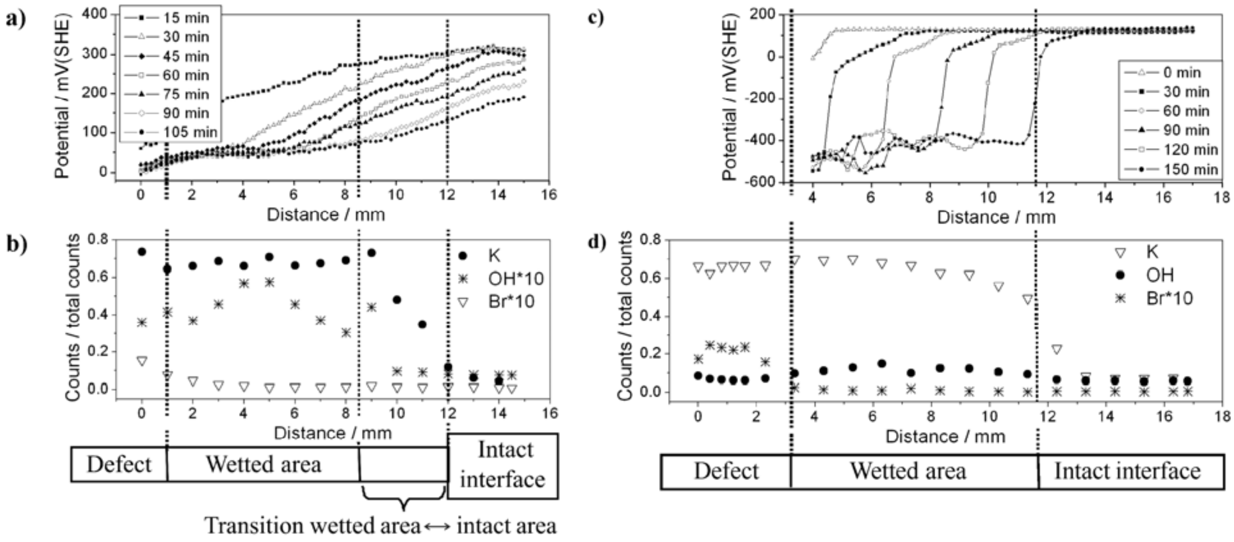

Fig. 7-10: a) Oxygen reduction induced ion transport processes along MBT/Au interfaces in humid air, applying highly viscous 0.5 molar KBr solution as defect electrolyte: SKP potential profiles, b) Resulting distribution of K^+, Br^- and hydroxide species after termination of the SKP measurement, detected by ToF-SIMS. c) Oxygen reduction induced ion transport processes along MBT/Ag interfaces in humid air, applying highly viscous 0.5 molar KBr solution as defect electrolyte: SKP potential profiles, d) Resulting distribution of K^+, Br^- and hydroxide species after termination of the SKP measurement, detected by ToF-SIMS.

Fig. 7-10c illustrates SKP potential profiles recorded during electrolyte transport processes along an MBT/Ag interface. In this case, a steep potential step indicates the borderline between the area of liquid spreading and interface sections entirely unaffected by ion transport. The wetting progress rate varies around 7.5 mm in 150 min and is slightly decreased compared to the process tracked on bare silver (see Fig. 7-8b). With respect to the results gained on gold (see Fig. 7-8a and Fig. 7-10a) it is interpreted that this deceleration is rather statistic. It may be attributed to the presence of MBT and the adsorption of MBT to silver, but the effect cannot be described as significant based on the available data. Fig. 7-10d confirms that electrolyte spreading along thiol/silver interfaces is dominated, as well, by a reduction process of atmospheric oxygen within the area of ion transport. The ToF-SIMS profiles reveal that no bromide enters this interface section and that in particular no insoluble AgBr is formed. The K^+ amount clearly reflects the ‘150 min’ SKP potential profile and indicates the maximum wetting progress with a distinct drop to its basic contamination level at x = 14.3 mm. The hydroxide quantity is increased in the electrolyte transport area. Its percentage of the total counts is smaller than the percentage detected on gold (compare Fig. 7-10b with Fig. 7-10d), but this does not necessarily mean that also the OH^- quantity is lower. The gold and silver matrices may differ; consequently, a direct comparison of the hydroxide percentage values is inappropriate.

7.2.2 Spectroscopic study of the MBT/Au interface degradation

In-situ SERS measurements were performed to track the degradation of the organic/solid interface structure during ongoing interfacial oxygen reduction and ion transport processes. Fig. 7-11 displays spectra recorded for a MBT monolayer adsorbed on gold. The cell design already introduced in Fig. 7-7 was applied and liquid spreading was initiated with KBr solution of high viscosity and Zn powder in the defect area (see Fig. 7-9a). Spectrum (a) can be assigned to the 'intact' MBT/Au interface, exposed to air of high humidity. Characteristic peaks occur at 393 cm^{-1} (benzene ring deformation vibration [190]), 601 cm^{-1} (C-S stretching vibration [190]), 707 cm^{-1} (C-S stretching and out-of-plane C-H deformation vibration [190]), 860 cm^{-1} (out-of-plane C-H deformation vibration [190]) and 1130 cm^{-1} (in-plane C-H deformation vibration [190]). Signals that result in more complex multi peak structures during interface degradation arise in the area around 501 cm^{-1} (benzene ring deformation vibrations [190]), 1009 cm^{-1} (C-H bending vibrations [190]) and 1241 cm^{-1} (in-plane C-H deformation vibration [34]/N-C-S ring stretch vibration [190]).

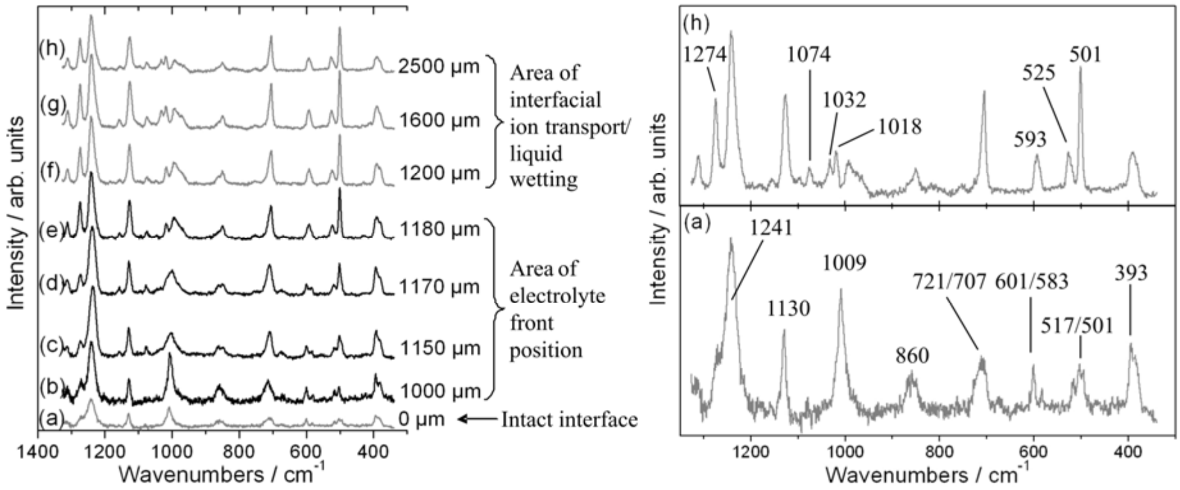

Fig. 7-11: In-situ SERS study of the MBT/Au interface degradation during ongoing oxygen reduction induced ion transport processes (see also Fig. 7-7). Spectra are displayed which are measured back-to-back at different locations on the sample. The first spectrum (a) was recorded in the intact interface section (referenced as position '0 µm' of the internal distance axis), the second (b) in the intact interface section but close to the expected electrolyte front position. Spectra (c), (d) and (e) characterise the electrolyte front position, spectra (f), (g) and (h) were recorded in the area of interfacial ion transport processes (see also Fig. 7-9a). The distance to the defect area decreases from (a) to (h) with increasing internal measurement position value, displayed in µm.

Some peak shapes of spectrum (a) change when interfacial electrolyte transport processes affect the interface. The doublet at 501/517 cm^{-1} is split in spectrum (h), because the intensity of the right peak (at lower wavenumbers) is increased compared to the left peak (at larger wavenumbers). The latter additionally shifts to the left by 8 cm^{-1}. The doublet at 601/583 cm^{-1} of spectrum (a) more and more coalesces during the initial stages of reactive wetting, illustrated by spectra (b) to (e). The signal finally seems to resemble nearly a single peak during ongoing interfacial oxygen reduction processes (see spectrum (h)). The intensity of the out-of-plane C-H deformation vibration at 721 cm^{-1} is distinctly decreased in spectrum (h).

Table 7-1: Assignment of SERS peaks of the MBT/Au interface in Fig. 7-11 (ν - stretching vibration, δ – deformation vibration, γ_r - rocking vibration, γ_w – wagging vibration, index ip - in plane vibration, op - out of plane vibration)

Wavenumber [cm^{-1}]	Assignment
1274	$\delta_{ip}(CH)$
1241	$\delta_{ip}(CH)/\ \nu(NCS)$
1130	$\delta_{ip}(CH)$
1074/1032/1018	sulphonate or sulphate vibrations
1009	$\delta(CH)$
860	$\delta_{op}(CH)$
721	$\delta_{op}(CH)$
707	$\nu(CS) + \delta_{op}(CH)$
601	$\nu(CS)$
501	$\delta(CC)$ aromatic ring
393	$\delta(CC)$ aromatic ring

In addition, the shape of the broad and intense peak at 1009 cm^{-1} remains unaffected during the initial stages of reactive wetting at or near the electrolyte front position (see spectra (a) to (d)). Then it resolves more and more into a multiplet during ongoing interfacial oxygen reduction processes (see spectra (e) to (h)) due to a strong intensity decrease of the benzene ring breathing vibration. This can be assigned to a simultaneous intensity decrease of the benzene breathing vibration and an intensity increase for signals that result from molecular species with oxidised sulphur atoms [191,192]. All mentioned peak changes underline that the geometry of the adsorbed monolayer obviously has changed during electrolyte wetting. The benzene breathing vibration is not perpendicular to the surface any longer. The flank peaks of the 1009 cm^{-1} signal area may be also slightly shifted to smaller and larger wavenumbers. However, it is obvious that new peaks emerge at 1074 cm^{-1}, 1032 cm^{-1}, 1018 cm^{-1}. They are assigned to sulphonate or sulphate vibrations and point at an oxidation of thiol functionalities during interfacial oxygen reduction processes [191,192]. Finally, it should be noted that the intensity of the signal at 1274 cm^{-1} continuously increases once the interface is in contact with electrolyte. It can be assigned to an in-plane C-H deformation vibration [190].

Based on their SERS results, Woods et al. proposed an adsorption of MBT on gold via a covalent S-Au bond [190] in agreement to previous studies of self assembled thiol monolayers on gold [110,193]. This can be confirmed regarding the S 2p signal of the XPS spectrum, displayed in Fig. 7-12a. It was recorded in the area of the ‘intact’ MBT/Au interface (see Fig. 7-9a) after termination of the SERS experiment. Peaks were fitted assuming an area ratio of 1:2 for S $2p_{1/2}$: S $2p_{3/2}$ and a splitting of 1.2 eV for the doublets [194,104]. The peak at 162.4 eV corresponds to exocyclic sulphur, the peak at 164.1 eV to the overlap of contributions from endocyclic sulphur, unbonded MBT and disulfide bridges of the MBT dimer 2,2’-dithiobisbenzothiazole [104,195-198]. It is unlikely that the monolayer degraded due to its exposure to X-ray radiation during the XPS measurement [193,199].

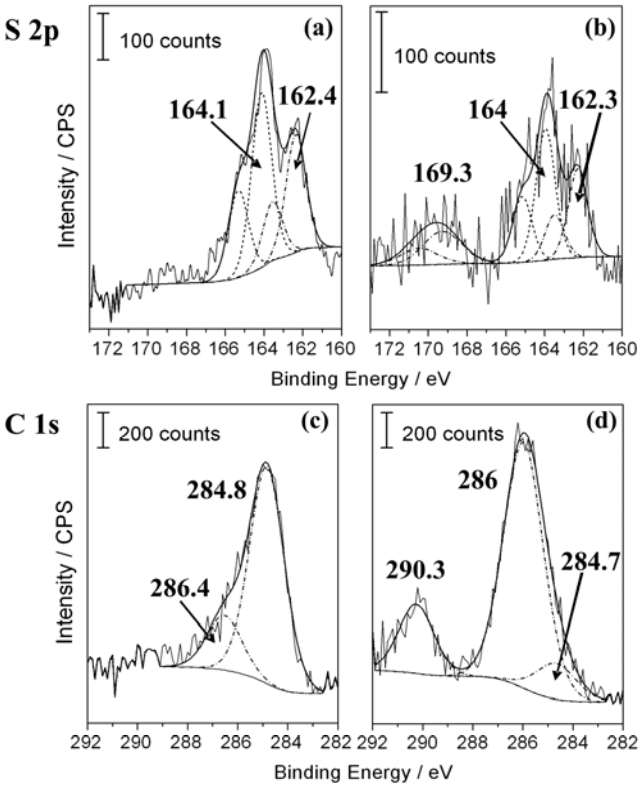

Fig. 7-12: XPS analysis of the MBT/Au interface. a) S 2p signal detected in the area of the intact interface, b) S 2p signal detected in the area of interfacial ion transport and oxygen reduction processes (see Fig. 7-9a). c) C 1s signal detected in the area of the intact interface, d) C 1s signal detected in the area of interfacial ion transport and oxygen reduction processes (see Fig. 7-9a).

Fig. 7-12b illustrates the S 2p signal recorded in the area of electrolyte transport, at a location relatively far away from the electrolyte front position. The peaks were consequently expected to reflect the SER spectra of the advanced state of the MBT/Au interface degradation (see spectra (f) to (h) of Fig. 7-12a). A new broad doublet is present at 169 eV and indicates the formation of sulphite/sulphate species on the surface [194,200]. The 162.4 eV peak intensity is decreased in Fig. 7-12b compared to Fig. 7-12a, but still present. This implies that the MBT monolayer was not completely desorbed from the surface and that the exocyclic sulphur of the MBT molecule is consequently just partially oxidised to sulphite/sulphate. A formation of benzothiazole-sulphonate, however, cannot be confirmed. The C 1s peaks of Fig. 7-12c and Fig. 7-12d moreover underline that not only sulphur, but also carbon components were oxidised during interfacial ion transport and oxygen reduction processes. This explains why the C-O signal at 286.1 eV is more intense than the C-C/C-H signal at 285 eV in Fig. 7-12d compared to Fig. 7-12c. As a conclusion, it is stated that the geometry of the ‘intact’ MBT monolayer re-adjusted on gold when it became affected by the electrolyte front [110]. A partial oxidation of the thiol functionality to a sulphate group was detectable in particular for the subsequent stages of ongoing oxygen reduction processes and high interfacial pH. A correlated partial desorption of MBT can be proposed as well based on the presented experimental and literature data.

7.2.3 Spectroscopic study of the MBT/Ag interface degradation

An in-situ SERS approach was also followed to investigate the MBT/Ag interface. In contrast to section 3.2 in this case no line was scanned. The measurement was performed on a single point in the 'intact' sample area instead and it was repeated periodically when the electrolyte front passed by Fig. 7-13 exemplarily presents some of the recorded spectra. Spectrum (a) reflects an interface still unaffected from any electrolyte spreading. It generally strongly resembles spectrum (a) of Fig. 7-11. However, a more detailed peak assignment is offered by literature studies [183,190,201]. Similar to the interpretation of the MBT/Au gold spectrum, e.g. the 831 cm^{-1} peak is correlated to a C-S stretching vibration and the 505 cm^{-1} to 521 cm^{-1} spectrum area is interpreted in terms of a partial overlap of benzene ring deformation vibrations, an in-plane C-H deformation vibration and C-N and N-H wagging vibrations [190,201]. Peaks in the area between around 1007 cm^{-1} and 1048 cm^{-1} were attributed to thiazole, N-H rocking, C-H-rocking, C-H-deformation, C-C-C deformation and C-C and C-H scissoring vibrations [183,190,201]. The intense peak at 1389 cm^{-1} was assigned to N-C-S ring stretching, C-C stretching, N-H, C-H or C-C rocking vibrations in different studies [183,190,201]. As a result, Lee et al. [201] and Yang et al. [183] assumed a perpendicular adsorption of MBT on silver via the exocyclic sulphur and nitrogen atom, whereas Woods et al. deny a bonding via nitrogen [190]. The most prominent changes on the monolayer covered silver surface occur again between 900 cm^{-1} and 1100 cm^{-1} (see Fig. 7-13, spectra (b) to (d)). Peak intensities at 1076 cm^{-1}, 1023 cm^{-1} and 985 cm^{-1} are distinctly increased and can be assigned to a change of the adsorption geometry of MBT on Ag and an oxidation of the thiol headgroup [190]. A similar conclusion was drawn for changes of the MBT spectrum on gold samples (see section 3.2). It should be noted that a general increase of peak intensities was detected on gold for interfaces exposed to electrolyte transport processes compared to spectra of the intact interface. In contrast, rather a decrease of the peak intensity is obvious on silver under these conditions (compare Fig. 7-11 with Fig. 7-13). We speculate that this finding is related to a change of the enhancement factor for Raman signals on Ag and Au during liquid wetting processes.

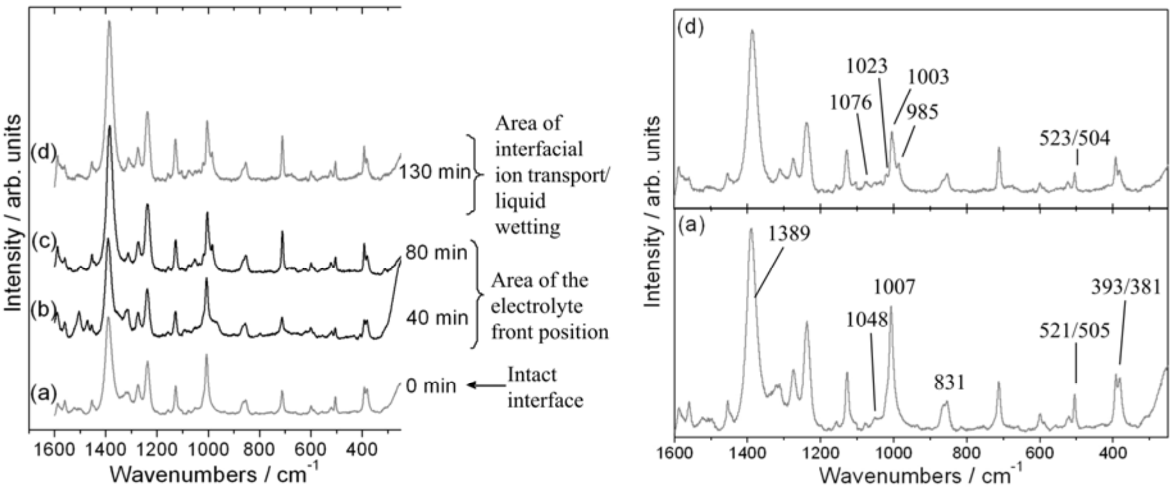

Fig. 7-13: In-situ SERS study of the MBT/Ag interface degradation. Measurements were performed at a fixed position on the sample while oxygen reduction induced ion transport processes proceeded along the interface. The first spectrum (a) was recorded when the investigated interface section was still unaffected from electrolyte spreading (internal reference time = 0 min). Spectra (b), (c) and (d) were monitored in 40- to 50-minute intervals after the electrolyte front passed the sample area under investigation.

Table 7-2: Assignment of SERS peaks of the MBT/Ag interface in Fig. 7-13 (ν - stretching vibration, δ – deformation vibration, γ_r - rocking vibration, γ_w – wagging vibration, index ip - in plane vibration)

Wavenumber [cm^{-1}]	Assignment
1427	ν(CN) + ν(CC) aromatic ring
1389	ν(NCS); ν(CC); ν(NH); γ_r(CH) or γ_r(CC) in different studies [184,191,202]
1274/1226	ν(CN)
985/1023/1076	sulphonate or sulphate vibrations
1009	δ(CH)
831	ν(CS)
505/521	δ(CC) aromatic ring; δ_{ip}(CH) + γ_w(CN) + γ_w(NH) in different studies [191,202]

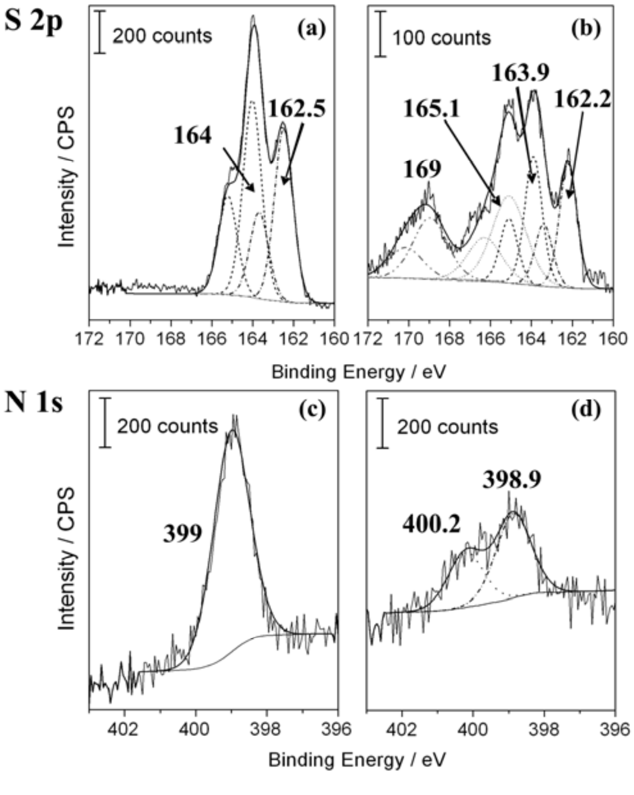

Fig. 7-14: XPS analysis of the MBT/Ag interface. a) S 2p signal detected in the area of the intact interface, b) S 2p signal detected in the area of interfacial ion transport and oxygen reduction processes (see Fig. 7-9a). c) N 1s signal detected in the area of the intact interface, d) N 1s signal detected in the area of interfacial ion transport and oxygen reduction processes.

Fig. 7-14 presents an XPS study of MBT/Ag interfaces. The S 2p signal of Fig. 7-14a, recorded at the 'intact' sample area, corresponds to the S 2p signal of the MBT/Au interface (see Fig. 7-12a). Fig. 7-14b illustrates the S 2p peaks received from the degraded MBT/Ag interface. The doublet at 169 eV is again attributed to highly oxidised sulphur species, in particular sulphite and sulphate. However, the S 2p signal obviously has to be fitted with another doublet at around 165 eV. It is distinctly broader than the sulphur peaks of the bonded MBT molecules at 162 eV and 164 eV, but its full width at half maximum is similar to that at

169 eV. It is consequently assigned to molecular sulphur species with an oxidation state of around +I which are not embedded in the monolayer [194]. Fig. 7-14c and Fig. 7-14d moreover exemplarily display the N 1s signal for the intact interface region and the area of electrolyte transport and oxygen reduction processes. In the wetted region, an additional peak at 400.2 eV can be identified (see Fig. 7-14d). Obviously, a nitrogen species with an increased oxidation number was formed.

In general, an exact assignment of SERS and XPS signals to certain MBT derivates is difficult. This is due to the fact that the interpretation of adsorption geometries of MBT on noble metals is still under discussion in literature [183,190,201]. However, it is clear that on both silver and gold substrates at least the exocyclic thiol functionalities of the MBT molecules are partially oxidised. Sulphonates and sulphates were formed. A complete desorption of the self assembled monolayer seems to be implausible. The degradation of the organic/substrate interface consequently seems to be confined to organic functionalities which are hydrolysis instable in alkaline environment and/or sensitive to oxidizing species near the interface [163,202]. A destruction of polymer backbones is not expected for these conditions; prospective in-situ SERS electrolyte wetting experiments on polymer/monolayer/substrate interfaces will have to clarify this aspect.

The presented SERS studies point at a slightly different degradation mechanism of the MBT/Ag interface compared to electrolyte transport processes that proceed along MBT/Au samples (compare Fig. 7-11 and Fig. 7-13). The 1009 cm^{-1} peak nearly completely diminishes on gold (see above), but not on silver. The XPS data on the other hand displays at least an additional sulphur species on silver, which was not detected on gold. The processes of oxygen reduction induced electrolyte spreading in fact will differ between gold and silver. Small variations in the adsorption geometry and packaging density of the monolayer on gold and silver surfaces should be already resulting from varying S-Au and S-Ag bonding parameters [198,203]. Moreover, the SKP reveals different potential levels for the areas of oxygen reduction. Consequently, also the reached current densities will not be the same. However, a polarisation of the interface to around -0.8 V_{SHE} is reached neither on Ag nor on Au which was expected as a sort of threshold value for reductive desorption of adsorbed thiols exposed to bulk electrolyte solution [110,183,204]. A different desorption mechanisms may be also correlated with different oxygen reduction pathways. Yeager et al. supposed a dominant peroxide mechanism with desorption of the peroxide anion on Au and a peroxide mechanism as well as direct O_2 reduction via a 4-electron pathway on Ag [205].

In general the presented data of intact and degraded MBT/Au and MBT/Ag interfaces are in good agreement with previous analytical studies of self assembled MBT monolayers adsorbed on noble metal surfaces [183,190,201]. For an exact identification of resulting molecular species, however, literature studies provide sets of data that are still too fragmentary. Prospective studies following the presented in-situ SERS approach will therefore benefit from cross-referencing wetting experiments with other monolayer molecules. Such species should exhibit a simplified molecular configuration, but will have to carry single functionalities that can be regarded as typical also for MBT.

7.3 Spectroscopic study of inhibitor diffusion in modified polyelectrolyte films [3]

Layer-by-layer (LbL) polyelectrolyte (PE) films are flexible, durable, inexpensive, light weight and transparent coatings that have received enormous attention during the past decades [206-209]. The LbL electrostatic assembly technique is a rich, versatile and quite inexpensive approach to the formation of thin films via alternating adsorption of positively and negatively charged macromolecules from aqueous solutions [210]. PE films have distinguishable properties like insolubility, infusibility, amorphous structure, permeability to water or impermeability to solutes, which can be used depending on the required applications. Their structure can be modified due to swelling and plasticizing by electrolytes [211], by blending with constituents on a molecular level or they can be used as nanoreactors [210]. They are attractive for sensing materials in electronics [211,212], electrochromic cells, batteries, fuel cells, ion-separation materials, enhanced chemical compatibility [213], corrosion protection [214] and drug delivery devices [215]. PE films are also studied as ion separation membranes due to selective permeability to polar or unpolar components of gases or liquids. Diffusion properties are modified by post treatments like insertion of silver nanoparticles [210], curing [216] or attachment of hydrophobic layers [217].

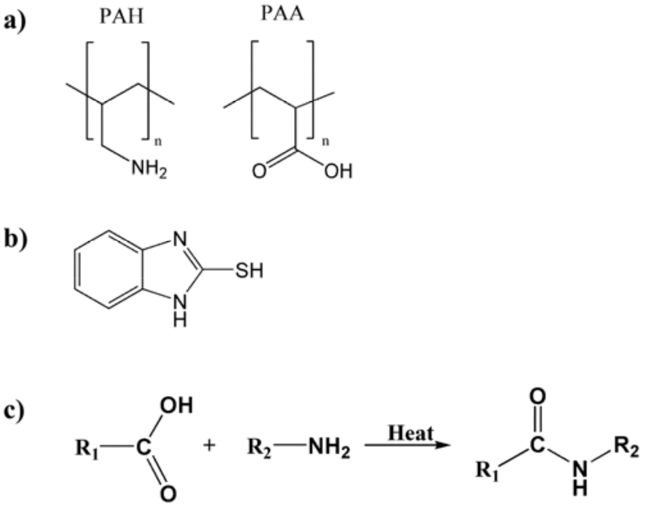

Fig. 7-15: Molecular structure of PAA and PAH (a) and 2-mercaptobenzoimidazole (MBI) (b); amidation during curing at elevated temperatures (c).

Several spectroscopic and electrochemical techniques were used to monitor the permeability of as-prepared and modified PE matrices. Bruening et al. applied cyclic voltammetry and in-situ spectroscopic ellipsometry to a poly(allylamine hydrochloride) / poly(styrenesulfonate) (PAH/PSS) matrix and showed that the permeability was highly dependent on the pH value of the used buffer solution [212]. Shiratori et al. [218] and Mendelsohn et al. [219] observed

---

[3] The approach presented in section 7.3 was developed together with Haybat Itani. The content of this section can also be found in Haybat's PhD thesis [221].

further that permeability of PAA/PAH films depended on the assembly conditions already like supporting electrolyte [212]. Ion diffusion in PAA/PAH is reported as function of crosslinking temperature by Stair et al. [216] and has been shown by conductance measurements or atomic absorption spectrometry.

In the present study an aqueous solution of 2-mercaptobenzimidazole (MBI, Fig. 7-15b) is applied to a LbL-PE multilayer films, composed of poly(allylamine hydrochloride) (PAH) and poly(acrylic acid) (PAA) (Fig. 7-15a). PAA/PAH permeability for MBI and water are investigated using in-situ backside surface enhanced Raman spectroscopy (in-situ SERS) [172] and electrochemical impedance spectroscopy (EIS) respectively. In-situ SERS enables the detection of MBI adsorbing to the SERS substrate/PE interface. Comparison of the growth of SERS signal was carried out for as-prepared films and different post treatments of PE films like loading with Ag-nanoparticles and curing at elevated temperatures. Carboxylic sites of the PAA layer allow the binding of Ag ions by ion exchange with protons. Metallic Ag-nanoparticles are formed after reduction [210]. Curing at elevated temperatures leads to formation of amides in the polymer matrix [220] (Fig. 7-15c). MBI diffusion is influenced by the interaction of PE with water. EIS measurements therefore reveal film behaviour during water uptake. Chemical changes of the PE film during immersion into MBI solution and curing are observed by Fourier Transform Infrared (FTIR) Spectroscopy.

7.3.1 Diffusion properties of PAA/PAH polyelectrolyte films

The results of the in-situ SERS experiment for MBI diffusion through the as-prepared PE film are displayed in Fig. 7-19b. The observed process consists of MBI diffusion through the PE film and afterwards adsorption of MBI on the SERS substrate beneath the PE film. Therefore, adsorption of MBI on the SERS substrate is examined. The SER spectrum of MBI is demonstrated in Fig. 7-19a. It corresponds to the measurement of Xue et al. [222] and peaks can be assigned according to former studies [222-224]. C-N stretching is observed at 1274 cm^{-1} and at 1226 cm^{-1}. The peak at 1427 cm^{-1} contains the C-N stretching vibration which is correlated with C-C stretching of the aromatic ring. The peak area of the C-H deformation in the aromatic ring at 1009 cm^{-1} is proportional to MBI concentration at the SERS substrate/PE interface. Peak area was determined for each measured spectrum by peak fitting (WiRE software) and then plotted for several times of immersion in Fig. 7-19c.

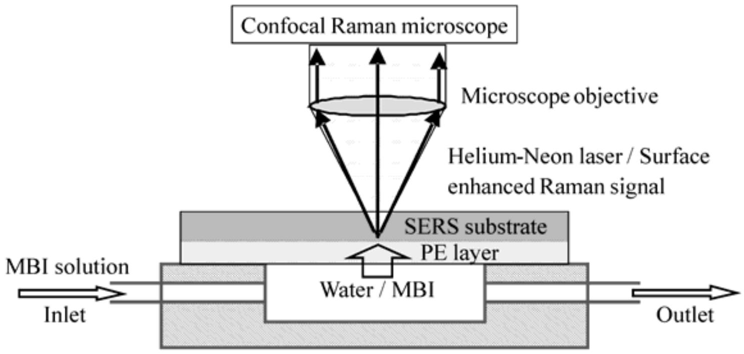

Fig. 7-16: Setup for in-situ SERS measurement of MBI diffusion from aqueous solution adoptet from [172]

Doneux et al. [223] conclude from DFT calculations and IR measurements of MBI and MBI bonded to Au that adsorption establishes by bond formation between sulphur and gold. According to the HSAB principle sulphur is more likely to form a bond with Au than N [225,226]. Whelan et al. [227] studied MBI adsorption on Au by XPS. They assume a second interaction of one deprotonated nitrogen with the gold surface additionally to the sulphur-gold bond. The molecular plane was concluded to be tilted from the "flat lying" adsorption geometry.

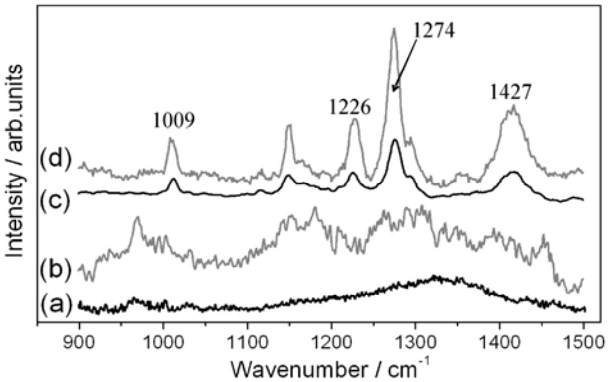

*Fig. 7-17: SERS spectra measured in backside geometry. a) Bare Ag surface of SERS substrate (intensity*10). b) PE on SERS substrate (intensity*5). c) MBI monolayer on bare Ag surface. d) PE covered Ag surface after 120 min of immersion into aqueous MBI solution.*

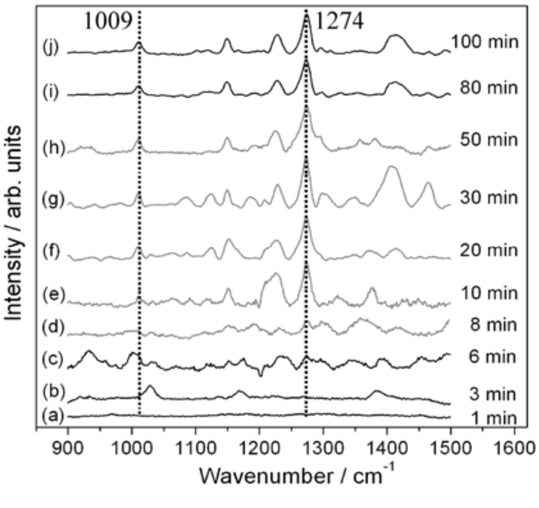

Fig. 7-18: MBI adsorption on PE covered Ag surface at different times after contact with MBI solution.

Adsorption kinetics of MBI on a pure SERS substrate is displayed in Fig. 7-19c. The rate of monolayer formation depends on temperature, solvent, rate of reaction with surface, concentration, chain length and structure of adsorbate [228]. The graph shows the pure MBI adsorption from aqueous solution. It can be divided into three sections. The first two sections are described by Schreiber and Ulman [203,229]. They summarise adsorption of alkanethiols from dilute solutions onto Au(111) as a two steps process. The first fast step is governed by Au-S interactions that form a less ordered monolayer in few minutes, followed by a slow step which lasts for several hours. The first step is diffusion controlled Langmuir adsorption and strongly depends on thiol concentration. Kinetics is governed by surface-head group reaction.

In this experiment thiol concentration is 10^{-2} mol/L. Due to Bain et al. [230] it reaches a stable thickness and contact angle are reached after 5 to10 min. In the graph the strong increase of peak area lasts for 15 min (Fig. 7-19c, section 1). It is followed by a slow decrease of peak area (Fig. 7-19c, section 2), which terminates after one hour and leads to a constant peak area (Fig. 7-19c, section 3). Due to Schreiber and Ulman [203,229] monolayer thickness and contact angles reach their final values at the end of the second step, which is a surface crystallization process [203,229,231]. Monolayer reorganisation leads thereby to changing adsorption geometry and decreasing peak area at 1009 cm^{-1} in section 2 before a constant value is reached in section 3 for the fully formed MBI monolayer.

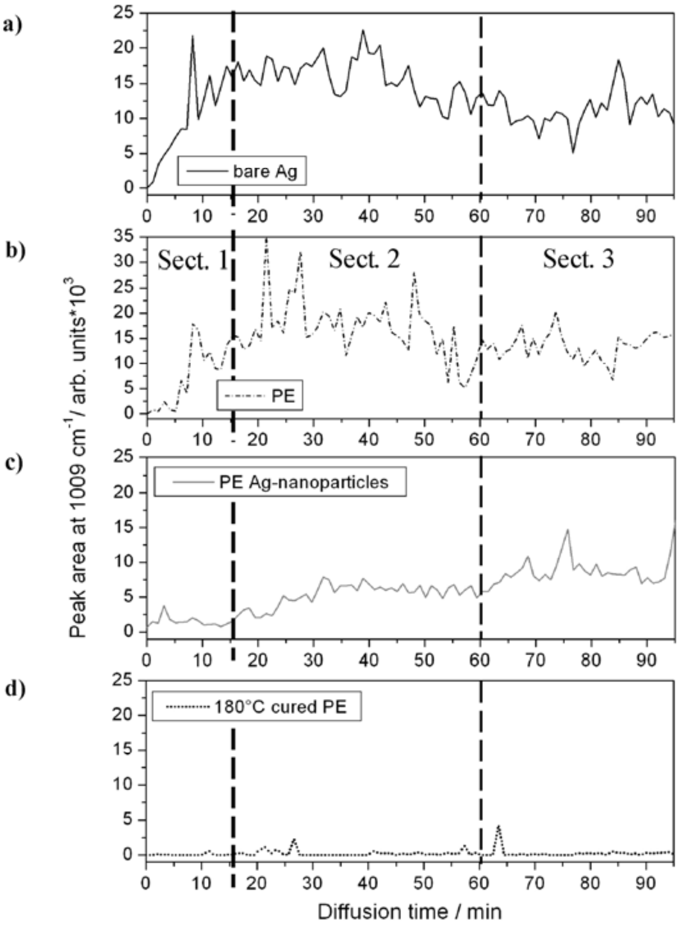

Fig. 7-19: In-situ SERS experiment of MBI adsorption on a) Ag surface of pure SERS substrate, b) SERS substrate covered with PE, c) SERS with PE containing Ag nanoparticles and d) PE cured at 180°C.

The in-situ SERS experiment of MBI diffusion through the PAA/PAH film is displayed in Fig. 7-19b. In situ SERS measurement was started when solution contacted the sample surface. In first minutes Raman peaks are detected at the interface, but they do not belong to the MBI SER spectrum (curves a-b). SERS is very sensitive to the interface. Already small amounts of organic matter lead to a spectrum due to high enhancement on the Ag surface [232]. The C-C backbone of PE appears as broad bands between 1300 cm^{-1} and 1500 cm^{-1}. Furthermore, diffusion and water uptake lead to changing adsorbate structure on the Ag surface due to coiling and flattening during swelling of the PE matrix. Therefore a fastly changing spectrum is detected [233,234]. After 6 to 9 min the MBI peaks are increasing

(Fig. 7-19b, curves d-e). Apart from the main peaks present in Fig. 7-19a changing spectra are recorded until 50 min after contact of the sample with MBI solution in curves d-h. In the same period decreasing intensity is detected in the progression of peak area at 1009 cm^{-1} (Fig. 7-19c, section 2). In section 3, peak area is constant between 60 and 100 min (Fig. 7-19c) and undisturbed MBI spectra are measured (Fig. 7-19b, curves i-j).

Peak area at 1009 cm^{-1} was only fitted if also the peak at 1274 cm^{-1} was detected. The peak at 1009 cm^{-1} was chosen because it does not interfere with increased baseline between 1300 cm^{-1} and 1500 cm^{-1}. Signal-to-noise ratio is lower for the PE covered SERS sample than for MBI adsorption on the bare Ag surface because of the fastly changing spectra presented in Fig. 7-19c.

The progression of the peak area with time of MBI diffusion through the PE film is similar to the pure Ag surface. After a fast increase in the section 1, slow decrease of the average signal is detected in section 2 from 25 to 60 min. That means section 1 which represents immediate adsorption [203,229,231] after diffusion through the PE film is few minutes longer than adsorption of MBI on the uncovered Ag surface. The average SERS signal is proportional to the amount of MBI at the interface. The delay in comparison to the pure Ag surface is due to diffusion through the PE film. Interaction of MBI with PE, pore size in presence of water, charging of bilayers, and interaction of PE with the Ag surface may lower MBI concentration at the interface and thereby delay adsorption. Section 3 in Fig. 7-19c shows similar peak areas for uncovered and PE covered Ag surface when the full monolayer coverage is reached.

IR measurement in 80° reflection geometry of the PE film was performed after the in-situ SERS experiment of MBI diffusion (Fig. 7-20, curve c). The PE film shows intense bands of carboxylate (COO^-) and carboxylic acid (COOH) groups of PAA. Asymmetric COO^- stretching appears at 1560 cm^{-1}, symmetric COO^- stretching at 1400 cm^{-1}, and the C=O stretching of the carboxylic acid groups at 1710 cm^{-1} [214,122]. After MBI diffusion a slight shift of the peak at 1710 cm^{-1} is observed in comparison to the as-prepared PE film (curve b in Fig. 7-20) due to changing hydrogen bonding of the carboxylic groups. Diffusion of MBI can be correlated to behaviour of PE in aqueous solution. The hydrophobic nature of the PAA/PAH polymer backbone forces the water molecules into a rigid, organized cluster of hydrogen bonded water molecules, together with carboxylic acid groups [235]. High water uptake leads to swelling because of weak interaction of bilayers and increasing free volume. However, integrity of PE films after the diffusion experiment in aqueous solution is assured by IR spectra. Additionally the two bands of MBI at 739 cm^{-1} and 1265 cm^{-1} are detected. The band at 739 cm^{-1} is the out-of-plane CH stretching which is typical for the 1,2-disubstituted benzene ring of MBI and C-N stretching vibration is detected at 1265 cm^{-1}. The MBI spectrum is given as a reference. Bands in the region between 1100 cm^{-1} and 1500 cm^{-1} reflect in plane deformation of C-H at 1110 cm^{-1}, SCN deformation at 1360 cm^{-1} and combined C-N and C-C deformation at 1420 cm^{-1} [223]. As a result, MBI is detected in the bulk of the PE film after immersion into aqueous MBI solution.

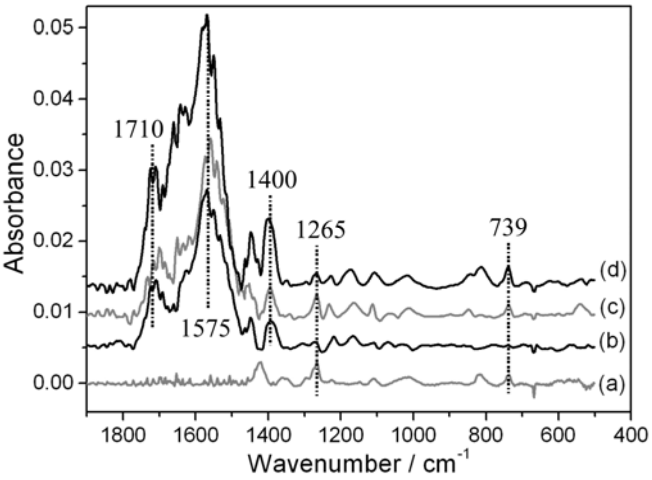

Fig. 7-20: IR spectroscopy in 80° reflection mode of (a) MBI monolayer on pure SERS substrate, (b) PE film, (c) PE film after MBI diffusion and (d) PE film cured at 180°C after MBI diffusion.

Table 7-3: Assignment of IR peaks inFig. 7-20

Wavenumber [cm^{-1}]	Assignment
1722-1710	ν(C=O) in carboxylic acid
1577-1560	$\nu_{as}(COO^-)$
1400	$\nu_s(COO^-)$
739	ν_{op}(CH) in 1,2-disubstituted benzene ring

Impedance measurements give information about permeability and barrier properties of the PE film during water uptake [236-238]. Absorption of water modifies the dielectric properties of the polymer film and thereby changes its capacitance as described in the experimental part of this work (chapter 3.1.2.2). The Bode plot in Fig. 7-21a shows the behaviour of the bare substrate and the PE covered substrate between 10 kHz and 1 Hz after 5 min of immersion into borate buffer. The Bode plot of the bare substrate shows the electrolyte resistance between 10 kHz and 600 Hz. The slope of the substrate impedance between 10 Hz and 1 Hz displays the pure double-layer capacitance at the substrate/electrolyte interface because of phase shift -90° in this frequency region. The PE impedance (curve RT) is slightly higher than the impedance of the bare substrate due to small contributions of the resistance of the PE film. Progression of the double layer capacitance determined at 1 Hz is displayed in Fig. 7-21c (curve RT). It is decreasing from 9.4 to 8.2 nF/cm^2 in 7 hours of immersion due to decreasing resistance of the PE film.

7.3.2 Effect of Ag nanoparticles on diffusion properties

PE films containing Ag nanoparticles are commonly used as SERS substrates or Ag nanoparticles coated with molecules with large Raman scattering cross sections SERS markers were applied [239,240]. Presence of Ag nanoparticles was confirmed by detection of the typical surface plasmon resonance peak with maximum at 440 nm in the UV-Vis absorption spectrum.

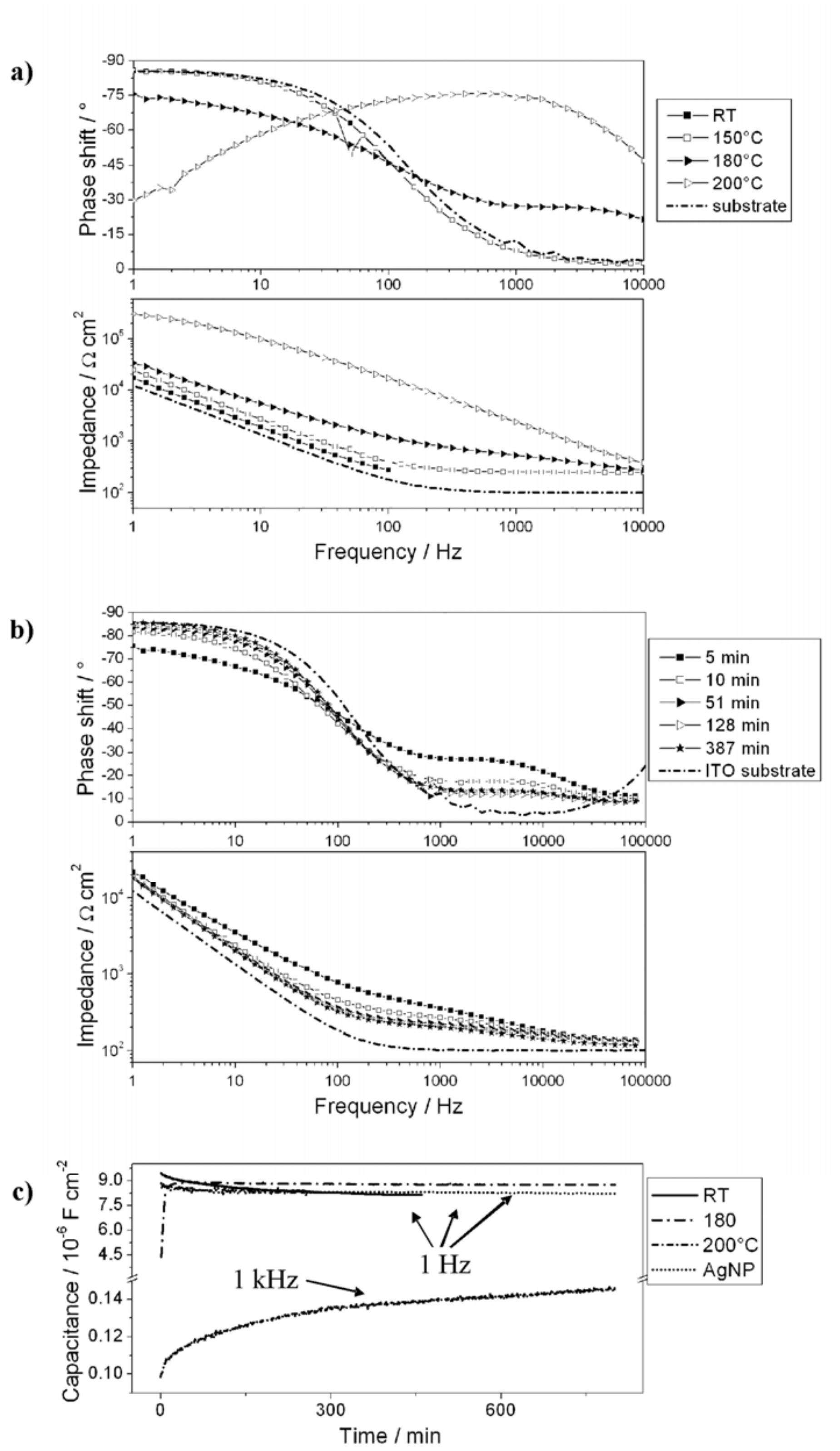

Fig. 7-21: a) Bode plots of uncured PE film (RT) and PE films cured at RT, 130°C, 150°C, 180°C, 200°C and ITO substrate as reference after 5 min of immersion in borate buffer. b) Bode plot of PE film cured at 180°C at increasing immersion times. c) Progression of double layer-capacitance of uncured (RT), Ag nanoparticles containing and 180°C cured PE film and progression of film capacitance of 200°C cured PE film during immersion for 900 min in borate buffer solution.

Growth of the MBI signal after diffusion through the Ag nanoparticles-modified PE film clearly differs from the as-prepared PE film (Fig. 7-19c). The adsorption process is much slower. Three sections can again be distinguished in the observed time scale. Slow increase of the MBI signal starts 15 min after contact of the probe with MBI solution. It reaches a constant level at 40 min. A further increase at 60 min leads to the peak area of full surface coverage with the MBI monolayer. This value is the same as reached after MBI diffusion through the as-prepared PE film.

The measured adsorption behaviour at the SERS substrate/PE interface can be correlated to a trapping effect induced by the Ag nanoparticles in the polymer bulk. In section 1 of Fig. 7-19c, MBI diffusing into the PE film reacts with Ag nanoparticles. Therefore MBI concentration is low at the SERS substrate surface and a low SERS signal is detected in the backside-geometry (Fig. 7-7 and [172]). Concentration at the substrate/PE interface increases in section 2 when the Ag nanoparticles are almost covered. The increase is slower compared to the as-prepared PE film. This may also be due to higher stability of the modified PE film in presence of water [241]. Therefore diffusion to the SERS substrate/PE interface may be slower. Furthermore, a part of MBI molecules is still consumed by Ag nanoparticles which are not fully covered. Changing adsorption geometry or further increase in MBI concentration in the polymer bulk can be reasons for the second step of increasing peak area at 1009 cm^{-1} which is detected at 60 min (Fig. 7-19c, section 3).

The Bode plot of Ag nanoparticles containing PE film after 5 min of immersion in electrolyte is similar to the uncoated substrate. Progression of the double layer capacitance at 1 Hz during water uptake is displayed in Fig. 7-21c. A slower decrease in capacitance is measured than for the as-prepared PE film. That can be interpreted as reduced swelling and correlated to the slow diffusion of MBI detected by in-situ SERS [241].

7.3.3 Diffusion properties of cured polyelectrolyte films

PE films were cured at room temperature (uncured film) and at 130°C, 150°C, 180°C and 200°C. The induced reaction leads to covalent bonding between PAA and PAH layers (Fig. 7-15c). FTIR measurements were performed in order to reveal the chemical composition of the PE film after curing (Fig. 7-22). All spectra display asymmetric CH_2 stretching at 2944 cm^{-1} and symmetric CH_2 stretching at 2866 cm^{-1} [242]. As curing temperature increases to 180°C a decrease of carboxylate bands at 1577 cm^{-1} and 1400 cm^{-1} can be observed. A shift in the peak position of the carboxylic groups from 1722 cm^{-1} to 1730 cm^{-1} can be explained by changing of the hydrogen bonding in the PE matrix. At the same time the amide formation is visible in the increase of the amide I peak at 1680 cm^{-1} (C=O stretch) and amide II peak (CN stretch and CNH deformation) at 1540 cm^{-1} [220]. Intensity of the NH_2 stretch at 3150 cm^{-1} decreases.

Observed chemical changes strongly influence the dielectric properties. Bode plots of cured samples are given in Fig. 7-21a after 5 min of immersion in electrolyte. The uncoated ITO substrate is displayed as a reference. The phase shift of the bare substrate is 0° at high frequencies, the measured impedance can therefore be interpreted as the electrolyte resistance [117]. In the low frequency region the impedance linearly increases. The capacitance of the electric double layer at the substrate/electrolyte interface is measured at phase shift -90° [117]. Samples cured from room temperature (RT) to 150°C behave similarly to the uncoated substrate. Although impedances are slightly higher, these PE films seem to be highly permeable for the aqueous electrolyte. Different behaviour is observed for curing temperatures of 180°C and 200°C. Bode plots of the sample cured at 180°C are displayed for increasing immersion times in Fig. 7-21b. 5 min after the immersion in the electrolyte, higher impedances are measured compared to the uncoated substrate. A clear difference is observed in the behaviour of phase shift. In the range of 1 to 10 kHz it is higher than the bare substrate. This indicates capacitive contributions of the PE film to the pure electrolyte resistance. At 1 Hz resistive behaviour is added to the electrolytic double layer leading to a lower phase shift. With longer immersion contributions of the PE film diminish. The Bode plot of 200°C curing temperature in Fig. 7-21a indicates complete film formation. The film impedance is around 10 times higher than impedances of the other systems in the displayed range. The phase shift of 75° indicates almost pure capacitive behaviour of the PE film at around 1 kHz.

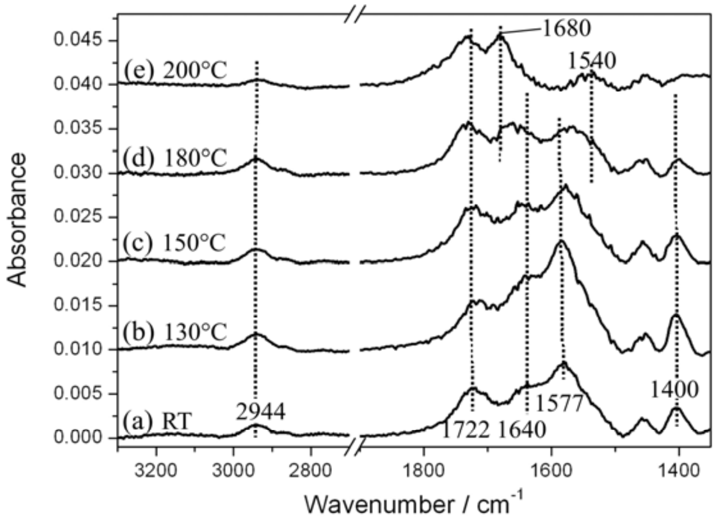

Fig. 7-22: FTIR spectra showing variation of the chemical composition of PE films with curing at 130°C (b), 150°C (c), 180°C (d) and 200°C (e). The spectrum at room temperature (RT) is given as a reference (a).

In-situ SERS diffusion experiments were performed with the 180°C cured PE film (Fig. 7-19c). Even after diffusion times of 12 h (not displayed here) MBI was not detected in the in-situ SERS measurements. Mobility of the polymer chains is decreased due to formation of amide bonds and diffusion of the water based solution is decelerated. Heating does not change the SERS activity of the used substrate. An ex-situ adsorption experiment assured that SERS activity of the Ag surface was not destroyed by simple curing in presence of oxygen. But in presence of PAA carboxylic acid groups will induce the formation of an oxide layer on the Ag surface [243,244] during curing at 180°C. Furthermore, PE binds covalently to the Ag substrate. In this case MBI cannot displace the PE from the Ag surface and is not detected by SERS. Nevertheless FTIR measurements of the cured sample (Fig. 7-20d) show the presence of MBI in the polymer bulk after the diffusion experiment. Its typical bands at 1265 cm^{-1} and 739 cm^{-1} are detected.

Capacitance variation with immersion time is displayed in Fig. 7-21c for uncured (RT) and cured PE films. Their clearly different behaviour supports the SERS diffusion measurements. Capacitance of the uncured PE film was evaluated at 1Hz. This means that the double layer capacitance is displayed with immersion time. Samples cured at 130°C and 150°C, and Ag nanoparticles containing film behave like the uncured PE film. Also capacitance of the 180°C cured film was calculated at 1 Hz although the phase shift is at 75° and shows contributions of the PE film resistance. The capacitance plot shows a fast increase due to interaction with the electrolyte. After 15 min the capacitance value of the electrolytic double layer is reached. The film capacitance after 200°C curing is obviously lower than the double layer capacitance. The intact PE film after 200°C curing allows determination of a water uptake of around 9 %, calculated from capacitance variation at 1 kHz (Fig. 7-21c).

The permeability of the PE film can be tuned by post treatments and by altering the assembly conditions. Diffusion is governed by electrostatic interaction, as shown for polar and non-polar gases [245]. Bilayers of this weak PE deposited at pH 3.5 form a loopy structure that swells in aqueous solution. Free volume in the film increases at the same time during water uptake. The low permeability of the cured PE film (180 and 200°C) is directly connected to the formation of covalent bonds between PE layers. The formation of amide bonds reduces the film free volume by forming a more compact structure and decreasing polymer chain mobility. But curing also leads to a modification of PE-substrate bonding and prevents detection of MBI diffusion via in-situ SERS.

7.4 Conclusions

Adhesion of epoxy-amine polymers on the iron oxide surface was observed on a molecular scale. Model molecules resembling the epoxy and the amine component were adsorbed in a thickness of few monolayers and their behaviour in presence of aqueous organosilane solutions was analysed. APS and GPS adsorb to an iron oxide surface which is covered with the epoxy-amine model molecules DETA or DGEBA, respectively. In presence of water, DETA adsorption to iron oxide is very low which indicates that amine groups in the polymer give low adhesion stability at high water concentration at the iron oxide/polymer interface. The experiment shows further that APS adsorbs to the surface from aqueous solution and can be therefore applied as adhesion promoter for the polymer. In the case of DGEBA, GPS adsorbs in presence of water and displaces DGEBA almost completely.

The simultaneous adsorption of the hardener of the water borne epoxy-amine polymer and of APS was observed from aqueous solution. The composition of the layers adsorbed again on an iron oxide surface is independent on the organosilane concentration. This shows that the adsorbed polymers of the aqueous hardener solution hide the substrate surface due to a high molecular mass compared to APS.

Further studies on the adsorption behaviour of the model molecules resembling the epoxy-amine polymers can be performed in the future by means of in-situ PM-IRRAS. It is suitable for studying in detail H_2O adsorption isotherms, adsorption geometries of adsorbates and for detecting the adsorption process in-situ.

The degradation of a self-assembled MBT monolayer was investigated on gold and silver. MBT/Au and MBT/Ag interfaces were exposed to electrolyte spreading and interfacial oxygen reduction processes. Electrolyte transport was initiated from a defect area covered by Zn powder and a droplet of highly viscous potassium bromide solution. SKP potential profiles tracking the liquid spreading along the samples exhibited characteristics that are typically attributed to the mechanism of cathodic delamination. ToF-SIMS experiments confirmed this and indicated a formation of hydroxide species in the region of electrolyte transport and an exclusion of bromide ions from the defect area. SKP potential profiles were reflected by the potassium distribution. The presence of MBT did not significantly inhibit the spreading process neither on gold nor on silver. SERS spectra showed that a degradation of the MBT/metal interface proceeds in two steps. When it is initially affected by the electrolyte front, the adsorption geometry of MBT readjusts. During the second deterioration stage a distinct geometrical reorganisation and partial desorption of the monolayer occurs. The thiol headgroup is oxidised to sulphite and sulphate during ongoing interfacial oxygen reduction processes at alkaline pH. Although SERS spectra are quite similar for MBT adsorption and monolayer degradation on Au and Ag, they nevertheless point at slightly different molecular geometries before and after interfacial electrolyte transport processes affect the monolayer. The presented in-situ SERS approach seems to be a promising tool for the prospective investigation of structural changes at polymer/oxide/metal interfaces during cathodic delamination.

Stability of PE film and diffusion of MBI depends on the applied post treatment. Diffusion kinetics is influenced by water diffusion and structural properties of the polymer layer [235,246]. Diffusion of MBI through PE films was investigated by in-situ SERS. Three sections of MBI diffusion are discernable in general: fast adsorption after diffusion through the PE film, changing adsorption geometry while reorganisation of the monolayer and a stable monolayer conformation in the last section. Kinetics of the first process depends on MBI diffusion through the polymer. Ag nanoparticles/PE nanocomposite showed a delay in the growth of the SERS signal due to a trapping effect. MBI molecules adsorb on the Ag nanoparticles surface and MBI concentration at the SERS substrate surface is lowered. PE films cured at 180°C did not reflect any SERS signal. Due to covalent binding of PE to the Ag surface an MBI SERS spectrum could not be measured, but IR spectra of the polymer bulk show MBI.

8 Overall conclusions and outlook

The aim of the presented work was to develop a deeper understanding of the mechanism of corrosion protection of the water borne epoxy-amine polymer. The performance and properties of the solvent borne epoxy-amine polymer were always used as a reference. In this context the influence of the known organosilane adhesion promoters APS and GPS were tested in form of primers and as additives.

This study implied the determination of polymer film stabilities at high humidities and in corrosive environment. ATR-IR spectroscopy, EIS, 90°-Peel tests, XPS and SEM were applied as well-known physicochemical methods for the detection of water uptake and diffusion, for the determination of interface stability and surface analysis. Further, in-situ backside SERS was established as a new method which enables the detection of chemical changes at buried interfaces.

The experiments showed that polarity of the polymer film and water uptake have a high influence on the behaviour in wet and corrosive environments. The water borne polymer exhibits a higher polarity and a higher water uptake compared to the solvent borne polymer. De-adhesion of the water borne polymer from the steel surface happens therefore earlier at high humidities compared to the solvent borne polymer. The interface stability of the water borne polymer on steel can be improved by addition of the adhesion promoting organosilane GPS: lower water uptake and higher interface stability at high humidity lead to higher corrosion resistance. Addition of APS results in higher water uptake and thereby reduces the interface stability and corrosion stability. APS was observed to form islands on the substrate and in the polymer bulk which are loosely bonded to the polymer. During drying of the sample after exposure to a humid environment, re-bonding is therefore not enhanced by APS.

Due to the described differences between the water borne and the solvent borne polymers, the corrosion mechanism is different in the water borne polymer than in previously studied systems. Also anions are detected at the degraded interface after cathodic delamination of the water borne polymer, whereas only cations enter the interface of previously observed coatings. Cation migration happens for reasons of electroneutrality in the degraded interface part which exhibits high hydroxide concentrations after oxygen reduction. In the case of the water borne polymer the electrolyte is additionally transported out of the defect into the interface due to capillary forces induced by high swelling and high water activity at the water borne polymer/steel interface. The value of water uptake plays obviously a central reole in the corrosion protection properties of the water borne polymer.

After addition of GPS to the water borne polymer the experimental results indicate that the interface stability in high humidity is strongly improved. However, at longer exposure (one week) to a corrosive environment, the GPS-modified water borne polymer/steel interface is less stable than the solvent borne polymer/steel interface.

In-situ backside SERS was developed in order to gain further insight into chemical degradation of the polymer during cathodic delamination. It was applied as a method to detect buried interfaces with high interface sensitivity. Effects of cathodic delamination on the first monolayer were examined. Instead of an epoxy-amine polymer on iron oxide an MBT monolayer was deposited on SERS active gold and silver surfaces. The simple structure of the model substrate enabled the correlation of SKP and XPS results with in-situ SERS results. Partial oxidative degradation of the monolayer was observed in the wetted area (Fig. 7-9a). Further, a change of the adsorption geometry was observed on gold and on silver substrates.

In-situ SERS was introduced as a promising method for analysis of buried interfaces and applied to to MBI diffusion through polyelectrolytes with different post treatments. Diffusion of small molecules in polymers is important for diffusion of gases like oxygen or corrosive gases, water and water vapour, but also for corrosion protection concerning diffusion of self-healing components. It was shown that loading of PE with Ag nanoparticles or curing at elevated temperatures leads to distinct diffusion behaviours. MBI concentration is decreased in presence of Ag nanoparticles in the PE bulk and MBI adsorption at the PE/SERS substrate interface is delayed. After curing at elevated temperatures, the PE is covalently bonded to the Ag surface of the substrate. MBI adsorption to the Ag surface is not possible and therefore not detected by in-situ SERS. This shows that the functionality of additives improving corrosion protection can be inhibited by a treatment of the polymer matrix.

In the presented studies the polymer properties were varied and described whereas the substrate surface was kept constant. In the future, the influence of the substrate surface composition on the interface properties of the polymer has to be studied. The contact of water during application of the water borne polymer was shown to increase the hydroxide surface concentration of the steel substrate in comparison to the solvent borne polymer. It has to be clarified if the adhesion stability of the polymer depends on a certain steel surface particularly in view of the effect that the polymer solvent has during application on the substrate.

Furthermore, the parameters of the corrosive environment can be varied in order to approach the real corrosion conditions. Wet-dry cycles of the humid and corrosive atmosphere relate properties detected during corrosive de-adhesion and re-bonding observed in the 90°-peel test. The influence of temperature on the corrosion reaction has not been considered. Also a mechanical load of the polymer may modify the observed corrosion behaviour of the water borne polymer. To date such an experiment is performed by blister tests where the electrolyte is applied with a pressure at the polymer/substrate interface through a hole in the substrate.

The application of SERS to the detection of a corrosion reaction can be extended from the first studies at polymer/noble metal interfaces to real polymer/iron oxide interfaces. The possibility to work with polymers has already been shown by the experiment concerning diffusion of MBI through the PAA/PAAH polyelectrolyte. The sample setup showed that the measurement is sensitive only to the first monolayer adsorbed on the metal surface. In future studies in-situ backside SERS will be applied to chemical changes resulting during corrosion or polarisation of buried polymer/substrate interfaces.

Understanding the processes at the substrate/polymer interface was shown to be crucial for explaining the performance of corrosion protection of the water borne polymer. But some questions related to the characterisation of the interphase are still open, e.g. the experiments of simultaneous adsorption of the amine component of the water borne polymer and APS show an independence on the APS concentration – in-situ experiments performed by PM-IRRAS could be a possibility to understand this result.

9 Tables of IR, SERS and XPS peak assignment

Table 9-1: Assignment of IR peak (ν - stretching vibration, δ – deformation vibration, sciss - scissoring vibration, index s - symmetric, as - asymmetric, ip - in plane vibration, op - out of plane vibration)

Wavenumber [cm^{-1}]	Assignment
3600-3100	ν(OH)
3300	ν(NH)
3150	$\nu(NH_2)$
3040-3036	ν(CH) aromatic group
2966-2960	$\nu_{as}(CH_3)$
2944-2925	$\nu_{as}(CH_2)$
2870	$\nu_s(CH_2)$
2866-2820	$\nu_s(CH_3)$
2810	ν(CH) in CHO
2500	ν(OD)
1722-1710	ν(C=O) in carboxylic acid
1680-1648	ν(C=O) amide I
1645-1629	δ(OH)
1608	ν(CC) aryl group
1580	ν(CC) aryl group
1577-1560	$\nu_{as}(COO^-)$
1540	ν(CN) + δ(CNH) amide II
1509	ν(CC) aryl group
1458	sciss(CH_2) + $\delta_{as}(CH_2)$; sciss(CH_3) + $\delta_{as}(CH_3)$
1420	δ(C-N) + δ(C-C)
1400	$\nu_s(COO^-)$
1360	δ(SCN)
1265	ν(C-N)
1246-1242	ν(COC) aryl ether
1110	δ_{ip}(C-H)
739	ν_{op}(CH) in 1,2-disubstituted benzene ring

Table 9-2: Assignment of SERS peaks (ν - stretching vibration, δ – deformation vibration, γ_r - rocking vibration, γ_w – wagging vibration, index ip - in plane vibration, op - out of plane vibration)

Wavenumber [cm^{-1}]	Surface	Assignment
1427	Ag	ν(CN) + ν(CC) aromatic ring
1389	Ag	ν(NCS); ν(CC); ν(NH); γ_r(CH) or γ_r(CC) in different studies [184,191,202]
1274	Au	δ_{ip}(CH)
1274/1226	Ag	ν(CN)
1241	Au	δ_{ip}(CH)/ ν(NCS)
1130	Au	δ_{ip}(CH)
1074/1032/1018	Au	sulphonate or sulphate vibrations
985/1023/1076	Ag	sulphonate or sulphate vibrations
1009	Au/Ag	δ(CH)
860	Au	δ_{op}(CH)
831	Ag	ν(CS)
721	Au	δ_{op}(CH)
707	Au	ν(CS) + δ_{op}(CH)
601	Au	ν(CS)
505/521	Ag	δ(CC) aromatic ring; δ_{ip}(CH) + γ_w(CN) + γ_w(NH) in different studies [191,202]
501	Au	δ(CC) aromatic ring
393	Au	δ(CC) aromatic ring

Table 9-3: Assignment of XPS peaks

Signal	Binding energy [eV]	Assignment
Si 2p	99.3	Si^0
	101.6 - 102	Si^{+II}
	102.8	Si^{+IIi}/ Si^{+Iv}
S 2p	162 – 162.4	Exocyclic sulphur in MBT
	164	Endocyclic sulphur in MBT
	169	Sulphite/ sulphate
C 1s	284.3	Aromatic compound
	284.9 – 285.1	C-C, C-H
	286.1 – 286.7	C-O
	289	C=O
	291.7 - 292	$\pi-\pi$ shake up satellite of aromatic compound
N 1s	399.7	NH_2
	401.6	NH_3^+
O 1s	530	Fe_2O_3
	531 – 531.4	OH
	531.9	C-O
	532.4 – 533.2	C=O, CO_3^{2-}, H_2O
	533.8	C=O, CO_3^{2-}
Fe 2p	706.8 - 707	Fe^0
	710.8	Fe^{2+}/Fe^{3+}

10 Abbreviations and symbols

APS	3-aminopropyl(trimethoxy)silane
ATR	attenuated total reflection
DETA	diethylentriamine
DGEBA	diglycidylether bisphenol-A
EDX	electron dispersive X-ray analysis
EIS	electrochemical impedance spectroscopy
ϕ	water uptake
GPS	3-glycidoxypropyl(trimethoxy)silane
IRRAS	infrared reflection absorption spectroscopy
LBL-PE	Layer-by-layer polyelectrolyte
PM-IRRAS	polarisation modulated IRRAS
$\Delta\Phi_S^{Ref}$	Voltapotential measured by scanning Kelvin probe
r.h.	relative humidity
SEIRA	surface enhanced infrared absorption
SEM	scanning electron microscopy
SERS	surface enhanced Raman spectroscopy
SFG	sum frequency generation
SIMS	static secondary ion mass spectrometry
SKP	scanning Kelvin probe
T_g	glass transition temperature
ToF-SIMS	time of flight-SIMS
wt%	weight %
XPS	X-ray photoelectron spectroscopy

11 References

[1] P.A. Sørensen, S. Kiil, K. Dam-Johansen, C.E. Weinell, J. Coat. Technol. Res. 6(2) (2009) 135

[2] C. Le Pen, C. Lacabanne, N. Pébère, Prog. Org. Coat. 39(2-4) (2000) 167

[3] B.S. Skerry, C.T. Chen, C.J. Ray, J. Coating Technol. 64(806) (1992) 77

[4] F. Galliano, D. Landoldt, Prog. Org. Coat. 44 (2002) 217

[5] M.L. Bruening, D.M. Dotzauer, P. Jain, L. Ouyang, G.L. Baker, Langmuir 24 (2008) 7663

[6] T. Alfrey, E.F. Gurnee, W.G. Lloyd, J. Polym. Sci. C 12 (1966) 249

[7] A. Apicella, L. Nicolais, W.J. Mikols, J. C. Seferis; J.C. Seferis, P.S. Theocaris, Eds; Interrelations between Processing Structure and Properties of Polymeric Materials; Elsevier, Amsterdam (1984)

[8] A. Apicella, L. Nicolais, C. Cataldis, Adv. Polym. Sci. 66 (1985) 189

[9] M.C. Lee, N.A. Peppas, Prog. Polym. Sci. 18 (1993) 947

[10] P. Nogueira, C. Ramírez, A. Torres, M.J. Abad, J. Cano, J. López, I. López-Bueno, L. Barral, J. Appl. Polym. Sci. 80 (2001) 71

[11] C.L. Soles, F.T. Chang, A. Bolan, H. A. Hristov, D.W. Gidley, A.F. Yee, J. Polym. Sci. B. 36 (1998) 3035

[12] C.L. Soles, A.F. Yee, J. Polym. Sci. B 38 (2000) 792

[13] F. Deflorian, S. Rossi, Electrochim. Acta 52 (2006) 1736

[14] L. Philippe, C. Sammon, S.B. Lyon, J. Yarwood, Prog. Org. Coat. 49 (2004) 302

[15] P. Moy, F.E. Karasz, Polym. Eng. Sci. 20 (1980) 315

[16] S. Cotugno, D. Larobina, G. Mensitieri, P. Musto, G. Ragosta, Polymer 42 (2001) 6431

[17] G. Mensitieri, M. Lavorgna, P. Musto, G. Ragosta, Polymer 47 (2006) 8326

[18] P. Wang, D.W. Schaefer, Langmuir 24 (2008) 13496

[19] R.G. Duarte, A.S. Castela, M.G.S. Ferreira, Prog. Org. Coat. 57 (2006) 408

[20] J. Crank, G.S. Park, Diffusion in Polymers; Academic Press, London (1968)

[21] E.P.M. van Westing, G.M. Ferrari, J.H.W. de Wit, Corr. Sci. 36(6) (1994) 957

[22] G.T. Fieldson, T.A. Barbari, Polymer 34(6) (1993) 1146

[23] G.T. Fieldson, T.A. Barbari, AIchE Journal 41(4) (1995) 795

[24] B.R. Hinderliter, K.N. Allahar, G.P. Bierwagen, D.E. Tallman, S.G. Croll, J. Coat.

Technol. Res. 5(4) (2008) 431

[25] M. Tagliazucci, F.J. Williams, E.J. Calvo, J. Phys. Chem. B 111 (2007) 8105

[26] E.J. Calvo, A. Wolosiuk, J. Am. Chem. Soc. 124 (2002) 8490

[27] C.H. Hamann, W. Vielstich, Elektrochemie; Wiley-VCH Weinheim (1998)

[28] O.A. Stafford, B.R. Hinderliter, S.G. Croll, Electrochim. Acta 52 (2006) 1339

[29] J. Kittel, N. Celati, M. Keddam, H. Takenouti, Prog. Org. Coat. 41 (2001) 93

[30] J. Kittel, N. Celati, M. Keddam, H. Takenouti, Prog. Org. Coat. 46 (2003) 135

[31] W. Funke, JOCCA-Surf. Coat. Int. 62 (1979) 63

[32] H. Leidheiser, W. Funke, JOCCA-Surf. Coat. Int. 70 (1987) 121

[33] O. Negele, W. Funke, Prog. Org. Coat. 28 (1996) 285

[34] A. Tomandl, M. Wolpers, K. Ogle, Corr. Sci. 46(4) (2004) 997

[35] K. Wapner, G. Grundmeier, Int. J. Adhes. Adhes. 24 (2004) 193

[36] D. Chidambaram, G.P. Halada, C.R. Clayton, Electrochem. Sol. St. 7(9) (2004) B31

[37] G. Grundmeier, M.Stratmann, Ann. Rev. Mat. Res. 35 (2005) 571

[38] M.G. Hosseini, M. Raghibi-Boroujeni, I. Ahadzadeh, R. Najjar, M.S.S. Dorraji, Prog. Org. Coat. 66(3) (2009) 321

[39] T. van Schaftinghen, S. Joiret, C. Delouis, H. Terryn, J. Phys. Chem. C 111(39) (2007) 14400

[40] W. Possart, J.K. Krüger, C. Wehlack, U. Müller, C. Petersen, R. Bactavatchalou, A. Meiser, C.R. Chimie 9 (2006) 60

[41] J. Telegi, T. Rigo, E. Pfeiffer, T. Keszthelyi, E. Kalman, Colloids for Nano- and Biotechnology; Eds. Z.D. Horvolgvi, E. Kiss, Prog. Coll. Pol. Sci. 135 (2008) 77

[42] G. Steiner, V. Sablinskas, W. Seidel, R. Salzer, Anal. Bioanal. Chem. 395(6) (2009) 1641

[43] I. Zawisza, A. Lachenwitzer, V. Zamlynny, S.L. Horswell, J.D. Goddard, J. Lipkowski, Biophysical Journal 85 (2003) 4055

[44] X.M. Bin, I. Zawisza, J.D. Goddard, J. Lipkowski, Langmuir 21 (2005) 330

[45] G. Grundmeier, M. Stratmann, Ber. Bunsenges. Phys. Chem. 11 (1995) 1387

[46] X.L. Lu, D.W. Li, C.B. Kristalyn, J.L. Han, N. Shepard, S. Rhodes, G. Xue, Z. Chen, Macromolecules 42(22) (2009) 9052

[47] F.J. Boerio, M.J. Starr, J. Adhesion 84(10) (2008) 874

[48] A. Meiser, K. Willstrand, P. Fehling, W. Possart, J. Adhesion 84(4) (2008) 229

[49] M. Gemmei-Ide, T. Motonaga, H. Kitano, Langmuir 22 (2006) 2422

[50] H. Asanuma, H. Noguchi, K. Uosaki, U.Z. Yu, J. Phys. Chem. C 113(50) (2009) 21155

[51] R. Vlasak, I. Klüppel, G. Grundmeier, Electrochim. Acta 52 (2007) 8075

[52] D.B. Asay, S.H. Kim, J. Chem. Phys. B 109 (2005) 16760

[53] P. Sutandar, D.J. Ahn, E.I. Franses, Macromolecules 27 (1994) 7316

[54] Y.P. Sun, W. Song, X. Zhu, R. Zhang, Q.Y. Pang, Z.R. Zhang, H.F. Yang, J. Raman Spectrosc. 40(9) (2009) 1306

[55] H.F. Yang, Y.P. Sun J.H. Ji, W. Song, X. Zhu, Y.Y. Yao, Z.R. Zhang, Corr. Sci. 50(11) (2008) 3160

[56] G.P. Halada, C.R. Clayton, eds. D.R. Baer, C.R. Clayton, G.D. Davis, G.P. Halada, State-of-the art application of surface and interface analysis methods to environmental materials interactions: in honor of James E. Castle's 65th year, Proceedings; Electrochemical Society Series 2001(5) (2001) 149

[57] F. Awaja, M. Gilbert, G. Kelly, B. Fox, P.J. Pigram, Progr. Polym. Sci. 34 (2009) 948

[58] D.E. Packham, J. Adhesion 84 (2008) 240

[59] J.W. McBain, D.G. Hopkins, J. Phys. Chem. 29 (1925) 188

[60] B.V. Deryagin, N.A. Krotova, Doklady Akad. Nauk SSSR 61 (1948) 849

[61] S.S. Voyutskii, Autohesion and Adhesion of High Polymers, Interscience (1963)

[62] J.F. Watts, Microchim. Acta 164(3-4) (2009) 379

[63] E.P. Plueddemann, P.G. Pape, H.M. Bank, Polym.-Plast. Technol. 25 (1986) 223

[64] E.P. Plueddemann, Silane Coupling Agents; Plenum press, New York (1991)

[65] A.J. Kinloch, Adheison and Adhesives: Science and Technology; Chapman and Hall, London (1987)

[66] K.L. Mittal, Silanes and Other Coupling Agents Eds.; VSP, Utrecht (1992)

[67] E.G. Plueddemann, J. Adhesion Sci. Technol. 2(3) (1988) 179

[68] M. Fedel, M. Olivier, M. Poelman, F. Deflorian, S. Rossi, M.-E. Druart, Prog. Org. Coat. 66(2) (2009) 118

[69] S. Dieckhoff, H. Van Eys-Schafer, M. Kaune, T. Kowalik, C. Kubell, A. Seiler, M. Beneke, A. Fangmeier, E. Kock, Corr. Reviews 25(5-6) (2007) 523

[70] D.A. Ramrus, J.C. Berg, J. Adhesion Sci. Technol. 20(14) (2006) 1615

[71] M.K. Joshy, L. Mathew, R. Joseph, Intern. J. Polym. Mat. 58(1) (2009) 2

[72] P.K. Kushwaha, R. Kumar, J. Appl. Polym. Sci. 115(3) (2010) 184

[73] A. Seth, W.J. van Ooij, JMEPEG 13 (2004) 468

[74] P.M. Hobbs and A.J. Kinloch, J. Adhesion 66 (1998) 203

[75] N.G. Cave, A.J. Kinloch, Polymer 33 (1992) 1162

[76] A.J. Kinloch, K.T. Tan, J.F. Watts, J. Adhesion 82 (2006) 1117

[77] M. Gettings, J.A. Kinloch, J. Mater. Sci. 12 (1977) 2511

[78] W.J. van Ooji, A. Sabata, J. Adhes. Sci. Techn. 5(10) (1991) 843

[79] M.-L. Abel, R.P. Digby, I.W. Fletcher, J.F. Watts, Surf. Interface Analysis 29 (2000) 115

[80] S.R. Wasserman, Y.-T. Tao, G.M. Whitesides, Langmuir 5 (1989) 1074

[81] G. Grundmeier, E. Matheisen, M. Stratmann, J. Adhesion Sci. Technol. 10(6) (1996) 573

[82] J.F. Watts, A. Rattana, M.-L. Abel, Surf. Interface Analysis 36(11) (2004) 1149

[83] M.S. Senett, S. E. Wentworth, A.J. Kinloch, J. Adhesion 54 (1995) 23

[84] J. Quinton, L. Thomsen, P. Dastoor, Surf. Interface Analysis 25 (1997) 931

[85] R. Rodríguez, S. Jiménez-Sandoval, M. Estévez, S. Vargas, J. Non-Cryst. Solids 354 (2008) 2623

[86] M.-L. Abel, J. F. Watts, Surf. Interface Anal. 41 (2009) 508

[87] J. Bertho, V. Stolojan, M.-L. Abel, J.F. Watts, Micron 41(2) (2010) 130

[88] Z.C. Wang, J.P. Suo, J. Li, J. Appl. Polym. Sci. 114(4) (2009) 2388

[89] W.G. Ji, J.-M. Hu, J.Q. Zhang, C.N. Cao, Corr. Sci. 48 (2006) 3731

[90] W.G. Ji, J.M. Hu, J.Q. Zhang, C.N. Cao, Surf. Coat. Technol. 201 (2007) 4789

[91] M. Stratmann, H. Streckel, Ber. Bunsenges. Phys. Chemie 92 (1988) 1244

[92] K. Oura, V.G. Lifshits, A.A. Saranin, A.V. Zotov, M. Katayama, Surface Science, An Introduction; Springer Berlin –Heidelberg (2003)

[93] K. Wapner, B. Schönberger, M. Stratmann, G. Grundmeier, J. Electrochem. Soc. 152 (2005) E 114

[94] M. Stratmann, H. Streckel, R. Feser, Corr. Sci. 32 (1991) 467

[95] D.M. Brasher, A.H. Kingsbury, J. Appl. Chem. 4 (1954) 62

[96] R. Posner, K. Wapner, S. Amthor, K.J. Roschmann, G. Grundmeier, Corr. Sci. 52(1) (2010) 37

[97] J.T. Zhang, J.M. Hu, J.Q. Zhang, C.N. Cao, Prog. Org. Coat. 49 (2004) 293

[98] R. Posner, M. Marazita, S. Amthor, K.J. Roschmann, G. Grundmeier, Corr. Sci. 52(3) (2010) 754

[99] R. Posner, G. Giza, R. Vlasak, G. Grundmeier, Electrochim. Acta 54 (2009) 4837

[100] I. Mrozek, A. Otto, J. Electron Spectrosc. 54/55 (1990) 895

[101] A. Otto, J. Raman Spectrosc. 36 (2005) 497

[102] A. Otto, M. Futamata in: K. Kneipp, M. Moskovits, H. Kneipp (Eds.): Surface Enhanced Raman Scattering – Physics and Applications, Topics Appl. Phys. 103 (2006) 147

[103] A. Otto, J. Raman Spectrosc. 37 (2006) 937

[104] D.G. Castner, K. Hinds, D.W. Grainger, Langmuir 21 (1996) 5083

[105] A. Leng, H. Streckel, M. Stratmann, Corr. Sci. 41 (1999) 547

[106] W. Fürbeth, M. Stratmann, Corr. Sci. 43 (2001) 207

[107] N. Fink, B. Wilson, G. Grundmeier, Electrochim. Acta 51 (2006) 2956

[108] K. Wapner, M. Stratmann, G. Grundmeier, Electrochim. Acta 51 (2006) 3303

[109] G. Sun, G. Grundmeier, Thin Solid Films 515 (2006) 1266

[110] J.C. Love, L.A. Estroff, J.K. Kriebel, R.G. Nuzzo, G.M. Whitesides, Chem. Rev. 105 (2005) 1103

[111] F. Richardson, Pigment and Resin Techn. 5 (1973) 41

[112] D.J. Weinmann, JOCCA-Surf. Coat. Int. 81(4) (1998) 186

[113] G.A. Howarth, JOCCA-Surf. Coat. Int. 82(9) (1999) 460

[114] J. Wielant, T. Hauffman, O. Blajiev, R. Hausbrand, H. Terryn, J. Phys. Chem. C 111 (2007) 13177

[115] M.I. Cook, F.H. Walter, D.A. Dubowik, JOCCA-Surf. Coat. Int. 82(11) (1999) 528

[116] P. Birnbrich, G. Bourscheidt, U. Nagorny, T. Roloff, H.-J. Thomas, G. Sabbadini, KGK 3(60) (2007) 86

[117] F. Mansfeld, J. Appl. Electrochem. 25 (1995) 187

[118] K. Wapner, Dissertation Bochum (2006)

[119] K. Dusek, M. Duskova-Smrckova, Prog. Polym. Sci. 25 (2000) 1215

[120] M. Öhman, D. Persson, Electrochim. Acta 52 (2007) 5159

[121] R.A. Veselkowsky, V.N. Kestelman, Adhesion of Polymers, 2002, McGraw-Hill Companies, Inc., USA

[122] L.V. Daimay, N.B. Colthup, W.G. Fateley, J.G. Graselli; The Handbook of Infrared and Raman Characteristic Frequencies of Organic Molecules, Academic Press, San Diego California (1991)

[123] N.T. Correia, J.J. Moura Ramos, B.J.V. Saramago, J.C.G. Calado, J. Colloid Interf. Sci. 189 (1997) 361

[124] G. Menges, E. Haberstroh, W. Michaeli, E. Schmachtenberg, Werkstoffkunde Kunststoffe, Carl Hanser Verlag, München/Wien, 2002

[125] M.Y.M. Chiang, M. Fernandez-Garcia, J. Polym. Sci. 87 (2003) 1436

[126] J. Feng, K.R. Berger, E.P. Douglas, J. Mater. Sci. 39 (2004) 3413

[127] I. Linossier, M. Gaillard, M. Romand, J. Adhesion 70 (1999) 221

[128] G. Bierwagen, D. Tallman, J.P. Li, L.Y. He, D. Jeffcoate, Prog. Org. Coat. 46 (2003) 148

[129] G. Bierwagen, J. Coat. Technol. Res. 5 (2008), 133

[130] A.S. Castela, A.M. Simoes, Corr. Sci. 45 (2003) 1631

[131] J.M. Hu, J.T. Zhang, J.Q. Zhang, C.N. Cao., J. Mater. Sci. 39 (2004) 4475

[132] G. Grundmeier, W. Schmidt, M. Stratmann, Electrochim. Acta 45 (2000) 2515

[133] G.T. Fieldson, T.A. Barbari, Polymer 34(6) (1993) 1146

[134] L. Philippe, C. Sammon, S.B. Lyon, J. Yarwood, Prog. Org. Coat. 49 (2004) 302

[135] L. Philippe, C. Sammon, S.B. Lyon, J. Yarwood, Prog. Org. Coat. 49 (2004) 315

[136] R. Touhsaent, H. Leidheiser, Corrosion 28 (1972) 435

[137] A.S. Castela, L. De Rosa, T. Monetta, D.B. Mitton, F. Bellucci, J. Electrochem. Soc. 145 (1998) 3830

[138] M. Destreri, J. Vogelsang, L. Fedrizzi, F. Deflorian, Prog. Org. Coat. 37 (1999) 69

[139] Z. Kolek, Prog. Org. Coat. 30 (1997) 287

[140] B.N. Popov, M.A. Alwohaibi, R.E. White, J. Electrochem. Soc. 140(4) (1993) 945

[141] G. Lendvay-Györik, T. Pajkossy, B. Lengyel, Prog. Org. Coat. 59 (2007) 95

[142] J. Crank (ed.), The Mathematics of Diffusion, Vol. 2, Clarendon Press, Oxford, 1994

[143] M.C.S.S. Macedo, I.C.P. Margarit-Mattos, F.L. Fragata, J.-B. Jorcin, N. Pébère, O.R. Mattos, Corr. Sci. 51 (2009) 1322

[144] G. Bierwagen, L. He, D. Tallman, Macromol. Sy. 187 (2002) 909

[145] R. Posner, K. Wapner, M. Stratmann, G. Grundmeier, Electrochim. Acta 54 (2009) 891

[146] Y.C. Lin, J. Polym. Res. 13 (2006) 369

[147] K.N. Allahar, B. Hinderliter, A.M. Simoes, D. Tallman, G.P. Bierwagen, Croll S.G., J. Electrochem. Soc. 154(10) (2007) F177

[148] H. Ochs, J. Vogelsang, Electrochim. Acta 49 (2004) 2973

[149] J.J. Max, C. Chapados, J. Chem. Phys. 116(11) (2002) 4626

[150] Y. Maréchal, J. Chem. Phys. 95(8) (1991) 5565

[151] R.A. Gledhill, A.J. Kinloch, J. Adhesion 6 (1974) 315

[152] J.E. Castle, J. Adhesion 84(4) (2008) 368

[153] J.H. Park, G.D Lee, H. Ooshige, A. Nishikata, T. Tsuru, Corr. Sci. 45 (2003) 1881

[154] A.P. Grosvenor, B.A. Kobe, M.C. Biesinger, N.S. McIntyre, Surf. Interface Anal. 36 (2004) 1564

[155] M.-L. Abel, J.F. Watts, R.P. Digby, J. Adhesion 80 (2004) 291

[156] K. Shimizu, M.-L. Abel, J.F. Watts, J. Adhesion 84(8) (2008) 72

[157] B.B. Johnson, K. Olafsen, A. Stori K. Vinje, J. Adhesion Sci. Technol. 16(14) (2002) 1931

[158] B.B. Johnson, K. Olafsen, A. Stori K. Vinje, J. Adhesion Sci. Technol. 17(9) (2003) 1283

[159] R. Posner, M. Santa, G. Grundmeier, in preparation

[160] K. Wapner, G. Grundmeier, Adv. Eng. Mat. 6 (2004) 163

[161] M. Guivenchuy, J.F. Watts, M.-L. Abel, M. Audenaert, Surf. Interface Anal. 38 (2006) 168

[162] A. Leng, H. Streckel, M. Stratmann, Corr. Sci. 41 (1999) 579

[163] A. Leng, H. Streckel, K. Hofmann, M. Stratmann, Corr. Sci. 41 (1999) 599

[164] W. Fürbeth, M. Stratmann, Corr. Sci. 43 (2001) 229

[165] W. Fürbeth, M. Stratmann, Corr. Sci. 43 (2001) 243

[166] G. Williams, H.N. Mc Murray, Electrochim. Acta 54 (2009) 4245

[167] M. Rohwerder, P. Leblanc, G.S. Frankel, M. Stratmann in P. Marcus, F. Mansfeld (Eds.), Analytical Methods for Corrosion Science and Engineering, Marcel Dekker Ltd., 2005, p. 605

[168] R. Posner, G. Giza, M. Marazita, G. Grundmeier, Corr. Sci. 52(5) (2010) 1838

[169] M. Santa, R. Posner, G. Grundmeier, in preparation

[170] A. Nazarov, T. Prosek, D. Thierry, Electrochim. Acta. 53 (2008), 7531

[171] A. Nazarov, D. Thierry, Protection of Metals 39 (2003), 55

[172] M. Santa, R. Posner, G. Grundmeier, J. Electroanal. Chem. 643 (2010) 94

[173] R. Posner, T. Titz, K. Wapner, M. Stratmann, G. Grundmeier, Electrochim. Acta 54 (2009) 900

[174] J. Wielant, R. Posner, G. Grundmeier, H. Terryn, Corr. Sci. 51 (2009) 1664

[175] R. Posner, Thesis, University of Paderborn (Germany), 2009

[176] A.J. Kinloch, J. Mater. Sci. 15 (1980) 2141

[177] J. Wielant, R. Posner, G. Grundmeier, H. Terryn, J. of Phys. Chem. C 112 (2008) 12951

[178] P.C.J. Beentjes, J. Van den Brand, J.H.W. de Wit, J. Adhesion Sci. Technol. 20(1) (2006) 1

[179] E. Kretschmann, Z. Physik 241 (1971) 313

[180] A. Hatta, Y. Chiba, W. Suetaka, Surf. Sci. 158 (1985) 616

[181] G.E. Poirier, E.D. Pylant, Science 272 (1996) 1145

[182] L.H. Dubois, R.G. Nuzzo, Annu. Rev. Phys. Chem. 43 (1992) 437

[183] H. Yang, Y. Sun, J. Li, W. Song, X. Zhu, Y. Yao, Z. Zhang, Corr. Science 50 (2008) 3160

[184] M. Ohsawa, W. Suetaka, Corrosion Science 19 (10) (1979) 709

[185] Y.S. Tan, M.P. Srinivasan, S.O. Pehkonen, S.Y.M. Chooi, J. Vac. Sci. Technol. A 22 (4) (2004) 1917

[186] M. Pourbaix, Atlas of Electrochemical Equilibria in Aqueous Solutions; Pergamon Press, Oxford (1966)

[187] Z.Y. Chen, D. Persson, C. Leygraf, Corr. Sci. 50 (2008) 111

[188] A.K. Neufeld, I.S. Cole, A.M. Bond, S.A. Furman, Corr. Sci. 44 (2002) 555

[189] K. Wapner, G. Grundmeier, Adv. Eng. Mat. 6 (2004) 163

[190] R. Woods, G.A. Hope, K. Watling, J. Appl. Electrochem. 30 (2000) 1209

[191] M.H. Schoenfisch, J.E. Pemberton, J. Am. Chem. Soc. 120 (1998) 4502

[192] R.L. Garrell, J.E. Chadwick, D.L. Severance, N.A. McDonald, D.C. Myles, J. Am. Chem. Soc. 117 (1995) 11563

[193] P.E. Laibinis, G.M. Whitesides, D.L. Allara, Y.T. Tao, A.N. Parikh, R.G. Nuzzo, J. Am. Chem. Soc. 113 (1991) 7152

[194] B.J. Lindberg, K. Hamrin, G. Johansson, U. Gelius, A. Fahlman, C. Nordling, K. Siegbahn, Physica Scripta 1 (1970) 286

[195] R. Szargan R., I. Uhlig, G. Wittstock, P. Rossbach, Int. J. Mineral. Process. 51 (1997) 151

[196] A. Schaufuss, P. Rossbach, I. Uhlig, R. Szargan, Fresenius J. Anal. Chem 358 (1997) 262

[197] D. Zerulla, I. Uhlig, R. Szargan, T. Chassé, Surf. Sci. 402-404 (1998) 604

[198] M. Zharnikov, S. Frey, K. Heister, M. Grunze, Langmuir 16 (2000) 2697

[199] K. Weldige, M. Rohwerder, E.R. Vago, H. Viefhaus, M. Stratmann, Fresenius J. Anal. Chem. 353 (1995) 329

[200] T.M. Willey, A.L. Vance, T. van Buuren, C. Bostedt, L.J. Terminello, C.S. Fadley, Surf. Sci. 576 (2005), 188

[201] C.J. Lee, S.Y. Leem, M.R. Karim, M.S. Lee, Spectrochim. Acta Part A 68 (2007) 1313

[202] H. Erlenmeyer, H. Ueberwasser, H.M. Weber, Helv. Chim. Acta 21 (1938)

[203] A. Ulman, Chem. Rev. 96 (1996) 1533

[204] M. Rohwerder, K, de Weldige, M. Stratmann, J. Solid State Electrochem. 2 (1998) 88

[205] E. Yeager, Electrochim. Acta 29 (1984) 1527

[206] G.Y. Decher, H. Möhwald, Langmuir 9(2) (1993) 481

[207] G.Y. Lvov, J. Schmitt, Thin Solid Films 244(1-2) (1994) 772

[208] A. Shipway, E. Kate, I. Willner, CHEMPHYSCHEM 1 (2000) 18

[209] X. Shi, M. Shen, H. Möhwald, Prog. Polym. Sci. 29 (2004) 987

[210] T.C. Wang, M.F. Rubner, R.E. Cohen, Langmuir 18(8) (2002) 3370

[211] G. Decher, B. Schlenoff, eds., Multilayer Thin Films; Wiley-VCH Verlag, Weinheim (2003)

[212] J.J. Harris, M.L. Bruening, Langmuir 16 (2000) 2006

[213] D. DeLongchamp, P. Hammond, Chem. Mater. 15 (2003) 1165

[214] J. Dai, D.M. Sullivan, M.L. Bruening, Ind. Eng. Chem. Res. 39 (2000) 3528

[215] O.M. Tanchak, C.J. Barrett, Chem. Mater. 16 (2004) 2734

[216] J.L. Stair, J.J. Harris, M.L. Bruening, Chem. Mater. 13 (2001) 2641

[217] X. Liu, B. Dai, L. Zhou, J. Sun, J. Mater. Chem. 19 (2009) 497

[218] S.S. Shiratori, M.F. Rubner, Macromolecules 33 (2000) 4213

[219] J.D. Mendelsohn, C.J. Barrett, V. Chan, A.J. Pal, A.M. Mayes, M.F. Rubner, Langmuir 16 (2000) 5017

[220] J.J. Harris, P.M. DeRose, M.L. Bruening, J. Am. Chem. Soc. 121 (1999) 1978

[221] H. Itani, PhD thesis, Bochum (2010)

[222] G. Xue, Y. Lu, Langmuir 10 (1994) 967

[223] Th. Doneux, F. Tielens, P. Geerlings, Cl. Boess-Herman, J. Phys. Chem. A 110 (2006) 11346

[224] K.T. Carron, M.L. Lewis, J. Mater. Sci. 28 (1993) 4099

[225] R.G. Pearson, Inorg. Chim. Acta 240 (1995) 93

[226] R.G. Pearson, J. Am. Chem. Soc. 85(22) (1963) 3533

[227] C.M. Whelan, M.R. Smyth, C.J. Barnes, N.M.D. Brown, C.A. Anderson, Appl. Surf. Sci. 134 (1998) 144

[228] S.D. Evans, E. Urankar, A. Ulman, N. Ferris, J. Am. Chem. Soc. 113 (1991) 4121

[229] F. Schreiber, Progr. Surf. Sci. 65 (2000) 151

[230] C.D. Bain, E.B. Troughton, Y.T. Tao, J. Evall, G.M. Whitesides, R.G. Nuzzo, J. Am. Chem. Soc. 111 (1989) 321

[231] R.K. Shervedani, A. Hatefi-Mehrjardi, M.K. Babadi, Electrochim. Acta 52 (2007) 7051

[232] B. Ren, J. Yao, C. She, Q. Huang, Z. Tian, Internet J. Vib. Spectrosc. 4 (2000) 2.4

[233] F.J. Boerio, Thin Solid Films 181 (1989) 423

[234] F.J. Boerio, W.H. Tsai, J. Polym. Sci. B 27 (1989) 1017

[235] O. Tanchak, K.G. Yager, H. Fritzsche, T. Harroun, J. Katsaras, J. Barett, Langmuir 22 (2006) 5137

[236] Q.C. Ruan, Y.C. Zhu, F. Li, J.W. Xiaso, Y. Zeng, F.F. Xu, J. Colloid Interf. Sci. 333 (2009) 725

[237] M.J. Rodríguez Presa, L.M. Gassa, O. Azzaroni, C.A. Gervasi, Anal. Chem. 81 (2009) 7936

[238] X. Wang, C. Somsen, G. Grundmeier, Acta Mater. 56 (2008) 762

[239] K. Kim, H.S. Lee, H.D. Yu, H.K. Park, N.H. Kim, Colloid. Surface. A 316 (2008) 1

[240] K. Kim, Y. M. Lee, H. B. Lee, K.S. Shin, Biosens. Bioelectron. 24 (2009) 3615

[241] K.K. Chia, R.E. Cohen, M.F. Rubner, Cem. Matr. 20 (2008) 6756

[242] J. Dong, Y. Ozaki, K. Nakashima, J. Polym. Sci. B 35 (1998) 5077

[243] S.J. Lee, S.W. Han, M. Yoon, K. Kim, Vibr. Spectrosc. 24 (2000) 265

[244] J.T. Young, W.H. Tsai, F.J. Boerio, Macromolecules 25 (1992) 887

[245] F. van Ackern, L. Krasemann, B. Tieke, Thin Solid Films 327-329 (1998) 762

[246] L. Krasemann, B. Tieke, Langmuir 16 (2000) 287